Polypyrrole-based Nanofibrous Membrane Separator for Lithium-ion Battery

by

Yifu Li

A thesis

presented to the University of Waterloo

in fulfillment of the

thesis requirement for the degree of

Doctor of Philosophy

in

Mechanical and Mechatronics Engineering

Waterloo, Ontario, Canada, 2021

Examining Committee Membership

The following serves on the Examining Committee for this thesis. The decision of the Examining Committee is by majority vote.

External Examiner:	Dr. Yong Lak Joo Professor
Supervisor:	Dr. Zhongchao Tan Professor
Internal Member:	Dr. Xianguo Li Professor
Internal Member:	Dr. Adrian Gerlich Associate Professor
Internal-external Member:	Dr. Aiping Yu Professor

Author's Declaration

This thesis consists of materials all of which I authored or co-authored: see Statement of Contributions included in the thesis. This is a true copy of the thesis, including any required final revisions, as accepted by my examiners.

I understand that my thesis may be made electronically available to the public.

Statement of Contribution

Yifu Li is the sole author for Chapters 1 and 7 which are written under the supervision of Prof. Zhongchao Tan and are not written for publication. This thesis consists of four manuscripts written for publication. Exceptions to sole authorship of material are as follows:

Research presented in Chapter 2:

This research is a literature review conducted at the University of Waterloo by Yifu Li under the supervision of Prof. Zhongchao Tan. Yifu Li designs the study and summarizes the literature relevant to electrospun separator with input from Prof. Qinghai Li from Tsinghua University. Yifu Li drafts the manuscript and each author provides intellectual input on manuscript drafts.

Y. Li, Q. Li, Z. Tan, A review of electrospun nanofiber-based separators for rechargeable lithium-ion batteries, *Journal of Power Sources*, 443 (2019) 227262.

Research presented in Chapter 3:

This research is conducted at the University of Waterloo by Yifu Li under the supervision of Prof. Zhongchao Tan. Yifu Li designs the study and completes the data collections and analysis. Yifu Li drafts the manuscript and each author provides intellectual input on manuscripts.

Y. Li, Z. Tan, Effects of a separator on the electrochemical and thermal performances of lithium-ion batteries: a numerical study, *Energy & Fuels*, 34 (2020) 14915-14923.

Research presented in Chapter 4:

This research is conducted at the University of Waterloo by Yifu Li under the supervision of Prof. Zhongchao Tan. Yifu Li designs the study and completes the data collections and analysis with consultations from Prof. Hesheng Yu, who is a visiting scholar at University of Waterloo. Yi Zhang contributes to modeling. Prof. Norman Zhou assists the sample characterization testing. Yifu Li drafts the manuscript and each author provides intellectual input on manuscripts.

Y. Li, H. Yu, Y. Zhang, N. Zhou, Z. Tan, Kinetics and Characterization of Preparing Conductive Nanofibrous Membrane by *In-situ* Polymerization of Polypyrrole on electrospun nanofibers, *Chemical Engineering Journal*. doi.org/10.1016/j.cej.2021.133531

Research presented in Chapter 5:

This research is conducted at the University of Waterloo by Yifu Li under the supervision of Prof. Zhongchao Tan. Yifu Li designs the study and completes the data collection and analysis with input from Prof. Hesheng Yu, who is a visiting scholar at University of Waterloo. Prof. Norman Zhou assists the sample characterization testing. Yifu Li drafts the manuscript and each author provides intellectual input on manuscripts.

Y. Li, H. Yu, N. Zhou, Z. Tan, Electrospun Nanofibrous Redox-active Separator for Enhancing the Capacity of Lithium-ion Batteries, *Journal of power souces* (Under review)

As first author of these four publications, I am responsible for experimental design, data collection and preliminary analysis, and drafting manuscripts. My coauthors provide guidance during each step of the research and provide feedbacks on draft manuscripts.

Abstract

A battery separator is one of the key components of a Lithium-ion battery (LIB). It serves as an insulator between the electrodes to prevent the internal short circuit. More importantly, the battery separator retains liquid electrolyte within its porous structure, allowing the migration of lithium ions during battery cycling. The fast-growing demand for high-performance LIBs in various applications requires the development of superior separators.

Electrospun nanofibrous separator receives considerable attention among all the progresses of battery separator research. Generally, electrospun nanofibrous separator offers appealing features including large pore size (typically above 500 nm), high porosity (typically above 70%) and interconnected porous structure. This improves ions transportation efficiency and battery cycling performance. However, most studies are focused on electrochemical inert material as battery separator, which is incapable of contributing any battery capacity to the LIB cells.

This thesis study develops a redox-active separator based on electrospun polypyrrole (PPy) composite nanofibers to enhance battery capacity. The proposed separator is fabricated by *in-situ* polymerization of PPy onto electrospun polyacrylonitrile (PAN) nanofibers followed by subsequent electrospinning to form a bilayer membrane.

This thesis starts with understanding the separator's effects on the battery performances to provide insights and guidance to the separator design. A two-dimensional electrochemical-thermal coupled model is developed for a 38120-type $LiFePO_4$ LIB. The model results show that separator thickness strongly impacts battery energy density. In addition, the mass transfer resistance of the separator increases with decreasing separator porosity, which results in increased electrolyte concentration gradient. However, the correlation between separator porosity and electrolyte concentration gradient indicates that a separator porosity of 80% or greater contributes little to the resistance to mass transfer.

After that, a detailed study of the kinetics on the *in-situ* polymerization of PPy with electrospun fibrous membrane as the template is carried out to better understand the mechanisms behind the fabrication of the proposed separator. The *in-situ* polymerizations of PPy are produced on electrospun fibrous PAN templates at temperatures ranging from 273 to 285 K. The experimental results show that the overall reaction rate of the *in-situ* polymerization process in the presence of electrospun fibrous template is faster than that without template. Further investigation confirms that the increase in the overall reaction rate results from the enhanced reactions between oxidized pyrrole oligomers and neutral pyrrole monomers

Then, the proposed separator with expected properties is fabricated and characterized. The produced separator exhibits a bi-layer structure, including a layer of PAN@PPy core-shell structured fibers and another layer of PAN fibers. The porosity and electrolyte uptake of the redox-active separator (79.3 ± 7.1% and 294.6 ± 31.5%) are much higher than that of a commercial PP separator (41% and 81.5 ± 17.4%). In addition, the redox-active separator is thermally stable up to 250 ℃ and capable of maintaining its dimensions at 160 ℃. Moreover, the redox-active separator exhibits superb mechanical properties than the electrospun PAN separator dose.

Finally, the separators are assembled into separate LIB cells for performance evaluation. The battery cell containing redox-active separator exhibits the highest discharge capacity of 158.7-227.0 mAh·g-1 at different current rates of 2-0.2 C. The enhanced battery capacity stems from the redox-activity of the PPy polymer contained in the redox-active separator. In addition, the battery cell with redox-active separator achieves the highest gravimetric energy density of 103.0 mAh·g-1, which is 56.1% higher than that with the commercial PP separator. These results suggest a promising strategy to enhance the capacity of LIBs by merely modifying the conventional separators into nanofibrous redox-active separators.

Acknowledgements

My PhD journey in University of Waterloo comes to an end upon completing this thesis. I would like to take this opportunity to thank the people who have made this journey not only possible but a fond memory I will always cherish.

First and foremost, I would like to express my deep gratitude to my supervisor, Prof. Zhongchao Tan, for all his encouragement and guidance throughout the past years. He fostered my curiosity, skills and professionalism for academic research. I have been fortunate to benefit from his dedication to help his students achieve success. Moving forward, he is the model I will always look up to as a researcher and educator.

I am grateful to my PhD examining committee members, Prof. Yong Lak Joo, Prof. Xianguo Li, Prof. Adrian Gerlich, and Prof. Aiping Yu for providing expert evaluations of this thesis.

My heartfelt thanks go to all the former and present members of Green Energy & Pollution Control Research lab; to name a few: Yi Zhang and Yunqiao Huang, thanks for the helping hands in lab and also all the alcohols we consumed for friendship; Dr. Maryam Razavi and Erqian Gao, thanks for the assistance to my research works. Especially, I would like to thank Dr. Hesheng Yu for the inspiration and intellectual input to my research articles.

In addition, I would like to acknowledge the Hai Zhou New Material Technology (Dong guan) Co., Ltd. for assisting the battery testing, and the Natural Sciences and Engineering Research Council of Canada and the GCI Ventures Capital for the financial supports.

I must thank my wife, Chao Qin, for her astonishing amount of support along my pursuit of academic studies. She has enriched my life and shaped me into the person I am today. Last but not least, I would like to thank my parents for always believing in me, which encourages me to explore the life without hesitation.

Table of Contents

List of Figures

List of Tables

List of Symbols

Notation	Term	Unit
A_i	Specific surface area	m^{-1}
$brug$	Bruggeman tortuosity exponent	
c_l	Electrolyte concentration	$mol \cdot m^{-3}$
c_s	Lithium concentration in solid electrode	$mol \cdot m^{-3}$
Cg_l	Electrolyte concentration gradient	$mol \cdot m^{-2}$
Cp	Heat capacity	$J \cdot kg^{-1} \cdot K^{-1}$
D_l	Diffusion coefficient in electrolyte	$m^2 \cdot s^{-1}$
D_s	Diffusion coefficient in electrode particles	$m^2 \cdot s^{-1}$
F	Faraday’s constant	$C \cdot mol^{-1}$
h	Heat transfer coefficient	$W \cdot m^{-2} \cdot K^{-1}$
i	Current density	$A \cdot m^{-2}$
$j_{0,i}$	Exchange current density	$A \cdot m^{-2}$
$j_{n,i}$	Local current density	$A \cdot m^{-2}$
k_i	Reaction rate constant	$m^{2.5} \cdot mol^{-0.5} \cdot s^{-1}$
k_T	Thermal conductivity	$W \cdot m^{-1} \cdot K^{-1}$
L_i	Thickness of battery component	m
Q_{act}	Active polarization heat generation rate	$W \cdot m^{-3}$
Q_{ohm}	Ohmic heat generation rate	$W \cdot m^{-3}$
Q_{rea}	Reaction heat generation rate	$W \cdot m^{-3}$
r	Radius distance of electrode particles	m
R	Gas constant	$J \cdot mol^{-1} \cdot K^{-1}$

t_+	Transference number of lithium ion	
T	Temperature	K
$U_{eq,i}$	Open circuit potential of the electrode	V
x	Distance variable through battery cell	m
y	State of charge of the cathode	

Greek letters

$\alpha_{\mathrm{a,i}}$	Transfer coefficient for anodic current	
$\alpha_{c,i}$	Transfer coefficient for cathodic current	
ε_l	Volume fraction of electrolyte	
ε_s	Volume fraction of solid material	
κ	Ionic conductivity of electrolyte	$\mathrm{S\cdot m^{-1}}$
ϕ	Electric potential	V
ρ	Density	$\mathrm{kg\ m^{-3}}$
δ	Electronic conductivity of solid electrode	$\mathrm{S\cdot m^{-1}}$
η	Local surface overpotential	V

Subscripts

a	Anode
c	Cathode
eff	Effective
ini	Initial
l	Liquid
p	Separator
s	Solid

List of Abbreviations and Acronyms

Notation	**Term**
Abbreviations	
AN	Aniline
DMP	Dimethylphenyl
OPSZ	Organopolysilazane
P3BT	Poly(3-butylthiophene)
PAN	polyacrylonitrile
PANI	Polyaniline
PBS	poly(butylene succinate)
PDA	Polydopamine
PE	Polyethylene
PEEK	Poly(ether ether ketone)
PEI	Polyetherimide
PFO	Poly(9,9-dioctylfluorene)
PI	Polyimide
PLA	poly(lactic acid)
PMIA	Poly(m-phenylene isophthalamide)
PP	polypropylene
PPESK	Poly(phthalazinone ether sulfone ketone)
PSA	Polysulfonamide
PU	Polyurethane
PVDF	poly(vinylideneu fluoride)
PVDF-HFP	Poly(vinylidene fluoride- hexafluoropropylene)

PVP	Polyvinylpyrrolidone

Acronyms

CA	Cellulose Acetate
DEC	Diethyl carbonate
EC	Ethylene carbonate
FEC	Fluoroethylene carbonate
HEMA	2-hydroxyethyl methacrylate
LATP	Lithium aluminum titanium phosphate
LiBOB	Lithium bis(oxalate) borate
LLTO	Lithium lanthanum titanate oxide
MCMB	Mesocarbon microbead
MEMO	3-(methacryloyloxy) propyltrimethoxysilane
OPS	Octaphenyl-Polyhedral oligomeric silsesquioxane
PAA	Polyamic acid
PEO	Polyethylene oxide
PET	Polyethylene terephthalate
PVA	polyvinyl alcohol
TEGDA	Tri(ethylene glycol) diacrylate
TPP	Triphenyl phosphate

Chapter 1

Introduction

1.1 Background

Nowadays, batteries are not only a ubiquitous power device for portable electronics, but also becoming the most promising candidate for powering electrical vehicles and large-scale energy storage systems [1]. Shifting electricity production from burning fossil fuels to sustainable energy sources is essential to the modern industrial society. Sustainable energy sources, including tidal energy, wind energy, solar energy, and biogas, generate electricity according to the time and climatic condition [2]. Thus, batteries as energy storage technologies are required for the utilization of electricity produced by sustainable energy sources.

In 1836, John F. Daniell proposed a practical and reliable battery cell that continuously produced a constant current for days [3]. Based on the Daniell cell, Gaston Planté invented the lead acid battery in 1859 as the first rechargeable battery. Nowadays, lead acid batteries are widely used in motor vehicles as power supply [4]. However, lead acid batteries are not suitable for portable devices like laptop computers and mobile phones because of the large volume and heavy weight. In 1980s, researchers [5, 6] found that lithium ions can be embedded into graphite and spinel, which inspires the invention of lithium-ion battery (LIB). Since then, with continual research and developments, LIB has become the most popular energy storage solution for a wide variety of portable electronic devices and electric vehicles because of their high energy density, long cycle life, and low self-discharging [7].

The charge-discharge function of LIBs is achieved by the lithium ions migrating between two electrodes through the electrolyte. As shown in Figure 1.1, an external electrical power source forces the electrons to pass through the external circuit and the lithium ions migrate towards the anode across the electrolyte during the charge process. When the battery is discharging, the electrons circulate in the reverse direction to produce electric power and the lithium ions migrate from anode to cathode.

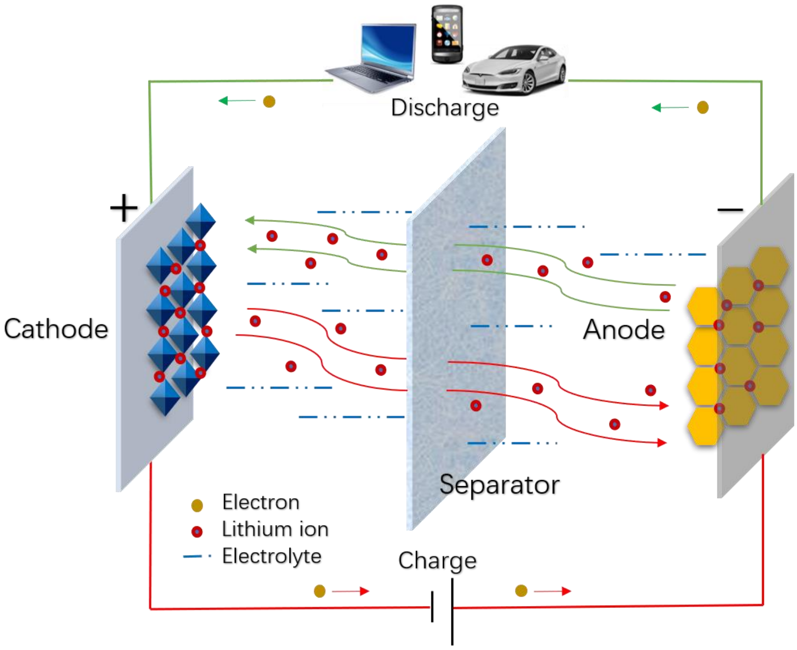

Figure 1.1. Schematic of a typical lithium-ion battery

The key elements in a LIB include cathode, anode, electrolyte, and separator. The cathode and anode receive and detach lithium ions during battery charging and discharging, respectively. The electrolyte acts as a reservoir of the lithium ions, enabling the lithium ions to transfer between the two electrodes. The battery separator placed between the two electrodes is a crucial component, which serves as an electrical insulator between the cathode and anode to prevent the internal short circuit. More importantly, the battery separator retains liquid electrolyte within its pores, allowing the migration of lithium ions during battery cycling. Thus, the structure and properties of separator strongly impact the battery cycling performance, lifetime, safety, and energy density [8]. The fast-growing demand for high-performance LIBs in various applications requires the development of superior separators.

1.2 Motivations and challenges

The battery separators currently dominating the commercial market are polyolefin-based thin membranes produced by wet or dry-laid process [9]. However, the commercial separators are criticized for its low porosity (less than 50% [10]), poor ionic conductivity (less than 1 mS cm^{-1} [11]), and poor thermal stability (shrink at around 130 °C [10]). As a result, considerable efforts have been made to the research and development of high-performance separators for advanced LIBs.

Recently, nanofiber-based separators have received considerable attention because of their interconnected porous structure and affinity to liquid electrolyte, which increases ions transportation efficiency, battery capacity and energy density [12, 13]. Therefore, they are reviewed extensively as follows.

Nanofibers-based separators can be produced by various methods, such as melt-blown [14], wet laid [15, 16], vacuum filtration [17, 18], and electrospinning [19, 20]. Table 1.1 compares different fabrication methods in terms of the ability of scale-up, variety of nanostructures, controllability of fiber formation, and operational difficulty. The melt-blown process has been adopted to produce commercial micro/nanofibers, where melted polymer is extruded through an orifice die with a jet of hot air to form fibrous web. However, the high temperature and airflow rate may cause fiber instability, leading to particles dispersed among the fiber web. As such, producing fine nanofibers is a challenge to melt-blown process [21]. Alternatively, wet-laid method requires the polymer precursor to form fibers in a liquid precursor suspension. Then, additional bonding additives are added to bond the base fibers by heat and pressure treatment. The structures and properties of the final fiber-based separators are mainly determined by the polymer type and compositions in the precursor suspension [22]. Similarly, nanofibrous separator produced by vacuum filtration process also requires the preparation of liquid precursor suspensions. The vacuum filtration help form the fiber web on a filter paper. However, achieving even vacuum force is difficult for a large surface, which limits the membrane dimensions produced by vacuum filtration method [23]. Compared to the three preceding methods, electrospinning can produce nanofibers with controllable nanostructures, such as the core-shell, hollow, and multichannel ones. It also gains interest for its application to battery separators in recent years as evidenced by the rising numbers of the annual publications (*see* Figure 1.2).

Table 1.1. Comparisons of different nanofiber fabrication methods

Methods	Scale-up	Nanostructure	Controllable fiber formation	Operational Ease	Ref.
Melt-blown	Yes	Fiber	Yes	Simple	[21]
Wet-laid	Yes	Fiber	No	Difficult	[22, 24]
Vacuum filtration	No	Fiber	No	Moderate	[17, 23]
Electrospinning	Yes	Fiber, Core-shell, Hollow, Multi-channel	Yes	Simple	[13, 25]

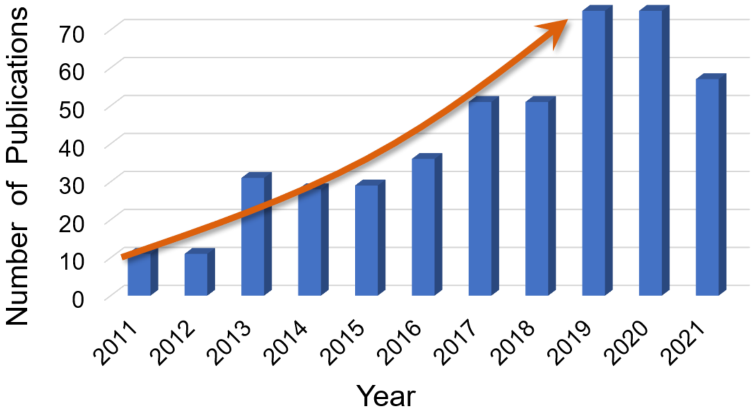

Figure 1.2. The number of publications on electrospun battery separators (data obtained by searching keywords "electrospinning separator" from Web of Science database, as of September 2021)

In general, electrospun nanofibrous separators have large pore sizes (typically above 500 nm), high porosity (typically above 70%) and interconnected pore structures [26-28]. This improves ions transportation efficiency and battery cycling performance. However, most research works are still focused on using electrochemical inert material as battery separator, although improved battery performances with nanofibrous separators are reported in the literature (*see* Section 2.1).

Admittedly, inert separators are incapable of contributing any battery capacity. The thicker the separator is, the lower the battery energy density is. Although, the use of a thinner separator seems to benefit the LIB energy density, it is impractical to do so [7] because a thinner separator retains less liquid electrolyte and has weaker mechanical strength, leading to poor battery performance and high safety risk.

An alternative strategy is to enhance the battery separator with redox activity. The redox-active separator can participate in the battery reactions and improve the battery capacity. Thus, the use of redox-active separators can eventually increase the energy density of LIBs.

For example, Wang *et al*. [17] first demonstrated the feasibility of fabricating redox-active separator by a bilayer structured cellulose/polypyrrole (PPy) composite separator for LIB. The PPy composite layer improved battery capacity stemmed from its redox activity, while the cellulose layer acted as insolation barrier between electrodes. The experiments showed that the redox-active separator contributes 0.116 mAh of discharge capacity to a $LiFePO_4$ half-cell at current rate of 0.2 C. This redox-active separator was fabricated via a conventional vacuum-filtration membrane-making process. However, this method is limited to the fabrication of small membranes for laboratory use only (as summarized in Table 1.1). Furthermore, the produced separators still suffered from low porosity of less than 60%, small pore size of below 60 nm, *etc*.

Thus, there is a need to develop PPy-based redox-active separators with improved structural properties. The electrospinning technology can produce battery separators with large pore size, high porosity and interconnected pores structure; such structures are expected to improve the LIB performance since these characteristics facilitate mass transportation in battery cells. Therefore, this thesis work aims to develop redox-active separators in the form of electrospun nanofibers.

1.3 Research objectives

This thesis aims to develop a technology for advanced LIB separators to enhance the battery capacity. This objective is achieved by several steps. First, understanding the separator's effects on the battery performances to provide insights and guidance to the separator design. Then, a bilayer structured redox-active separator is proposed based on *in-situ* polymerization of PPy onto electrospun polyacrylonitrile (PAN) nanofibers. A kinetics study of the *in-situ* polymerization is carried out to better understand the mechanisms behind the fabrication of the proposed separator. Finally, the proposed redox-active separator with expected properties is fabricated, followed by characterization and battery testing to study its properties and performances.

The following specific tasks are completed in this thesis work:

1) Develop a numerical model to quantify the effects of battery separator's thickness, porosity, and thermal properties on commercial-scale cylindrical LIB.
2) Compare controversial mechanisms· for pyrrole polymerization to identify the best suitable one.
3) Study the kinetics of *in-situ* polymerization of PPy onto electrospun nanofibers.
4) Fabrication of the redox-active separator and characterize its morphology, chemical composition, thermal stability and mechanical strength.
5) Evaluate the performance of redox-active separator in LIB.

1.4 Thesis structure

This study aims to develops a PPy based redox-active nanofibrous separator for LIB to improve the battery capacity. The redox activity of the separator is stemmed from the PPy polymer, which is integrated with the electrospun nanofibers by *in-situ* polymerization.

The structure of this thesis is organized as follows. Chapter 1 presents the background of LIB separator followed by introducing the current research trend of developing electrospun nanofibrous separator. Although the most research works are based on inert separators, a few research works have demonstrated the feasibility to use redox-active separator to further improve the battery capacity. Therefore, this thesis is motivated to develop nanofibrous redox-active separator in order to achieve well-developed porous structure and further improve the battery performance.

Chapter 2 provides a detailed literature review to cover the recent research progress of electrospun separators, which is a promising type of separator in LIB to enhance lithium ions transportation efficiency due to its ideal features like interconnected porous structures, high porosities and large surface-to-volume ratio. In addition, the commonly used methods of integrating PPy with electrospun nanofibers are briefly reviewed.

Chapter 3 presents a numerical modeling study to quantify the separator's effect on the LIB performances, in order to provide insights and guidelines for the separator design. A two-dimensional electrochemical-thermal coupled model is developed for 38120 cylindrical $LiFePO_4$ LIB. This type of commercial battery is used for many applications including electrical vehicles. The model is first validated with experimental data obtained from literature. Then the validated model is used to study the impact of separator design parameters, including thickness, porosity, thermal conductivity, and heat capacity, on the electrochemical and thermal performances of the battery.

Chapter 4 studies the kinetics of the in-situ polymerization of PPy onto electrospun nanofibers, aiming at the understanding of the mechanism of the fabrication process to produce redox-active nanofibers. Two different kinetics models are developed based on existing PPy polymerization mechanisms. The most suitable mechanism is first identified by comparing the model results with experimental data. Then, the kinetics of *in-situ* polymerizations of PPy on electrospun fibrous polyacrylonitrile (PAN) templates are studied, followed by the investigation of the activation enthalpy and entropy of the reaction.

Chapter 5 fabricates the PPy based nanofibrous redox-active separators based on electrospinning and *in-situ* polymerization processes. The obtained separator exhibits a bilayer structure, including a layer of PAN@PPy core-shell structured fibers and another layer of PAN fibers. Detailed characterization of the fabricated separator is presented, including the separator morphology, chemical composition, thermal stability, and mechanical property. Moreover, the redox-active separator is assembled into LIB coin cells to study the battery performance.

Chapter 6 summaries the conclusions of this thesis research and recommends the research directions for the future.

Chapter 2

Literature Review

2.1 Electrospun nanofibrous separators for LIB

Electrospinning technology is derived from the study of charged fluids. The ability of charged fluids to eject liquids was first reported by Rayleigh in 1882 [29]. Then, a detailed description of the deformation of charged liquid droplet was provided by Geoffrey Taylor in 1964 [30]. Figure 2.1 shows the deformation of a liquid droplet to eventually form fiber ejection in an electric field. When placing a liquid droplet in an electric field, the repulsive electrostatic force on the liquid surface increases with the increasing electric field strength. Once the repulsive force is greater than the hemispherical surface tension, an elongated droplet which also known as the Taylor cone is formed [31]. With the further increase of the electrical field strength, the repulsive electrostatic force will keep rising to eject fibers from the tip of the Taylor cone.

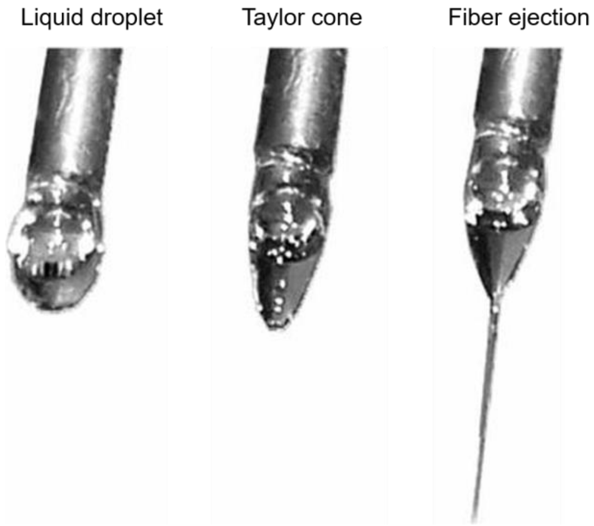

Figure 2.1. Images of liquid droplet deformation to form fiber ejection [31]

Figure 2.2 shows the schematic of a typical electrospinning system that can be used to produce electrospun separators in a laboratory setting. The setup is composed of a high voltage power supplier, a syringe with metallic needle, and a grounded collector. In a typical process, the selected electrospun precursors, such as PVDF, PAN, and PAA, are dissolved in solvent and loaded into the syringe. The high voltage power supply is connected to the metallic needle to form an electric field between the needle and the grounded collector. The ejected fiber undergoes an elongating whipping before reaching the collector while the solvent evaporates. Eventually, randomly oriented solid fibers are deposited onto the collector. The morphology and structure of the collected nanofibers can be controlled by the operational parameters such as applied voltage, tip to collector distance, temperature and humidity. As shown in Figure 2.2, different types of syringes and collectors can be applied to fabricate desired structures of nanofibers. Using a multi needle syringe can upscale the nanofiber production. It also allows different types of fiber solvents to eject at the same time to form composite membranes [32]. The co-axial needle contains a small inner capillary fitted inside the outer capillary can produce nanofibers with a core-shell structure by using two fiber materials [33, 34]. Using rotating drum or conveyor as a collector increases the depositing area and can control the spatial orientation of deposited fibers by adjusting the rotation or running speed [35].

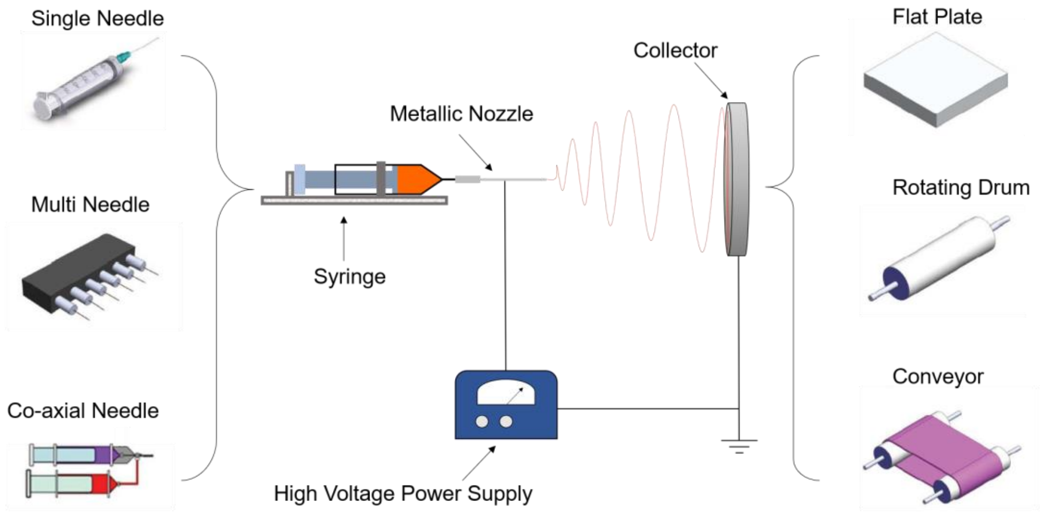

Figure 2.2. Schematic diagram of typical electrospinning setup

Electrospinning is ideal for fabricating nanofiber-based membrane separators for LIB with desired structures. However, it is criticized for its low production rate in the range of milliliters per hour. Adding additional nozzles may improve productivity, but, the repulsive electric-field from the additional nozzles causes distortion of the overall electric-field which leads to non-uniform nanofiber distributions [36, 37].

Alternatively, needle-less electrospinning is developed to overcome such drawbacks. For example, Yarin *et al*. [38] reported a magnetic-field-assisted needleless electrospinning system to improve the nanofiber production rate. It contains two layers of fluids with a polymer solution as the upper layer and ferromagnetic suspension as the lower layer. A magnetic field was applied to this system to form vertical spikes from magnetic suspension that perturbed the interlayer interface, as well as the free surface of the upper polymer layer. Meanwhile, an electric field was also applied to the system, the perturbations of free surface resulting in thousands of fibers ejected upward to the collector. Later, Jirsak *et al*. [39] proposed a simpler setup of needleless electrospinning by using a rotating cylinder as the nanofiber generator which is partially immersed in the polymer solution. When the cylinder rotates, the polymer solution is adhered onto the cylinder surface and generates enormous numbers of fiber jets under electric field. Similarly, some other rotary fiber generators such as, disc, ball and spiral coil were proposed by Niu *et al*. [40] and Wang *et al*. [41] as shown in Figure 2.3.

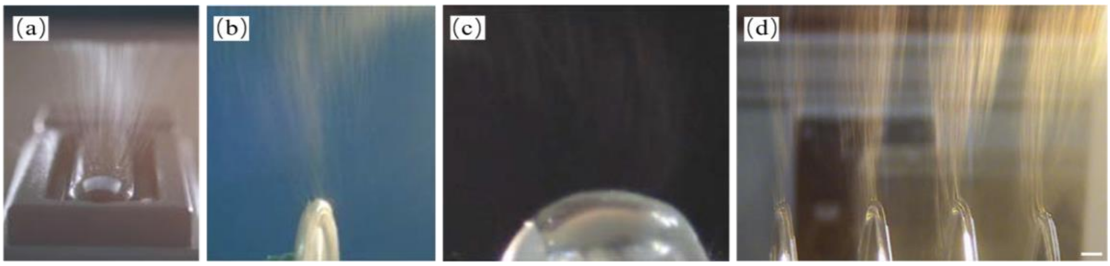

Figure 2.3. Different rotary fiber generators for needleless electrospinning process. (a) cylinder [42] (b) disc (c) ball [40] (d) spiral coil [41]

Admittedly, needle-less electrospinning generally requires higher applied voltage and closer collecting distance compared to needle electrospinning to generate fibers in similar diameter range [43]. However, it is feasible to generate large number of fibers from free surface of polymer solution. Thus, it has been quickly adopted in commercial applications. Companies such as Elmarco Ltd., Revolution Fibers Ltd. and SNC Ltd. have all launched their needleless electrospinning machines to achieve mass production of nanofibers. The rapid development of electrospinning technology also creates a promising future for the electrospun separators for LIBs.

Electrospun separators can be divided into four major types based on their composition and structure, namely monolayer separator, multilayer separator, modified separator, and composite separator. Monolayer and multilayer separators refer to the separators that contain one and multiple layers of electrospun nanofibers, respectively. Each layer of nanofibers is composed by one type of material. Modified separators are modified from electrospun separator via surface modification to further improve the surface electrochemical properties. Composite separators are fabricated by adding inorganic particles or co-electrospinning with multiple polymer nanofibers to electrospun separators.

2.1.1 Monolayer separators

Monolayer separator is the simplest membrane separator; it is prepared by one kind of precursor material. Unlike the traditional microporous separator which obtains its pore structures by membrane stretching [19], the pore structures of electrospun separator are formed by interstices between fibers. Thus, features like high porosities（typically above 70%）, large specific surface areas (typically above 10 $m^2 \cdot g^{-1}$ [43, 44]) and interconnected porous structures are readily achieved by the electrospun membrane separator. Electrospun monolayer separator can be made from different polymer materials. PVDF [45-48], PAN [49-51] and PI [52-55] are the most commonly reported polymers to prepare monolayer electrospun separators due to their good affinity to liquid electrolyte [7] and stable electrochemical properties [56].

Gao *et al*. [46] studied the effects of electrospinning process on the crystal structure and molecular chain conformation of PVDF separator. The charge density and elongation forces on the ejected fibers are enhanced by increasing applied voltage from 8 kV to 15 kV, resulting in the decrease of average fiber diameter from 884 nm to 514 nm. Results also indicate that the crystallinity of PVDF decreased while the amount of oriented molecular chains increased after electrospinning process. Low crystallinity of the membrane separator also contributes to lowering the internal resistance of LIB, because the migration of lithium ions could be hindered by the crystalline region of nanofibers [57]. As results, Li/$LiMn_2O_4$ battery cell with electrospun PVDF separator obtains better battery cycling performances as 95.2 % of capacity was retained after 50 cycles at 0.2 C rate, whereas the battery cell with a commercial microporous separator only remained 85.9 % of capacity in the same condition. This could also be attributed to the more uniform pore distribution of electrospun separators than commercial microporous separators. The uniform pore size distribution of a membrane separator can avoid the nonuniform current densities on the electrode-separator interface, which suppress the growth of lithium dendrites on the anode surface [58]. The interconnected pore structure and high porosity of an electrospun separator also facilitate the migration of lithium ions during battery cycling.

Yang *et al*. [48] proposed a spherical hat collector to obtain PVDF membrane separator with uniform thickness and fiber diameter. Experiment results show that the median diameters of fibers collected with a plane collector increased from about 125 nm to 188 nm during the collecting time of 70 min. The electrospun fibers obtained from the spherical hat collector were stable and thinner as the median diameters varied from about 116 nm to 133 nm during the same collecting time. In addition, the tensile strength of 6.9 MPa was achieved for the electrospun separator using the hat collector.

Electrospun PAN membrane with various fiber diameter and pore size were fabricated by Cho *et al*. [59] and were studied as a separator in LIB. The highest ionic conductivity of 2.6 $mS \cdot cm^{-1}$ is obtained by PAN membrane with the biggest pore size (380 nm) and porosity (76 %). Such structure features enable the retention of large amount of liquid electrolyte and meanwhile facilitate the migration of lithium ions passing through the membrane separator. Superior rate capability with electrospun PAN separator is also observed in graphite/$LiCoO_2$ battery cells as more than 90 % of the capacities retained at 4 C rate, which is more than 2 times of a commercial separator at the same condition. However, the battery cell contains electrolyte-soaked PAN separator cannot endure the operation at temperature of 150 °C, as the separator shrunk about 26% and caused a short circuit. This is because the carbonates in the electrolyte can act as plasticizers and weaken the interactions between the nitrile groups of PAN [60]. Thus, the electrolyte-soaked PAN separator shrinks when the temperature exceeds 150 °C. Sabetzadeh *et al*. [51] fabricated porous electrospun PAN separator by adding 7 wt% water into the electrospinning solution to induce phase separation during fiber solidification. The porous PAN shows higher porosity and electrolyte uptake than non-porous PAN membrane, resulting in a high ionic conductivity of 2.95 $mS \cdot cm^{-1}$. However, the porous structure sacrifices the mechanical properties which decreases the tensile strength from 30.6 to 14.4 MPa.

PI polymer has also been adopted to develop electrospun separator for LIB. Miao *et al.* [54] developed electrospun PI separators and studied its performances. The LIB with electrospun PI separator exhibits higher discharge capacity and rate capacity than a commercial separator. The polar electrolyte can be strongly coordinated within the polymer chains due to the electron donor and acceptor groups of PI. Moreover, the electrospun PI battery cell also shows an excellent cycling stability as the capacity remains almost the same after 100 cycles in a $Li/Li_4Ti_5O_{12}$ battery cell at 0.2 C rate. Cao *et al.* [52] reported the superior thermal stability (up to 500 °C) and electrolyte uptake (2522%) of electrospun PI separator. The battery cell with electrospun PI separator also shows advantages over the commercial PE separator with respect to rate capacity of LIB. The graphite/$LiCoO_2$ battery capacity retained 78.4% and 69.28 % of its initial values at a high current rate of 8 C and 16 C, respectively, whereas only 66 % and 8.48 % capacity retained for a LIB with commercial PE separator at the same condition. Since the PI polymer is insoluble, the above mentioned electrospun PI separators were prepared with polyamic acid (PAA) precursor solution followed by heat treatment to convert PAA into PI. However, the instability of PAA limited the fabrication of electrospun PI separator via this two-step method. Kong *et al.* [55] proposed fluorinated PI (F-PI) to increase the solubility of PI by incorporating of pendant trifluoromethyl ($-CF_3$) groups into the polymer backbone. The high polarity of F-PI membrane separator also provides affinity with polar liquid electrolyte. The ionic conductivity of F-PI separator was 37.6 % higher than PI separator.

In recent years, more novel materials were prepared as electrospun monolayer separators for LIBs. Electrospun poly(ether ether ketone) (PEEK) membrane separator was proposed by Li *et al.* [61, 62]. The least oxygen concentration to support combustion of PEEK is as high as 36.0–38.0% [63], implying excellent self-extinguishment ability in air. The PEEK separator exhibits high porosity of more than 90%, superior electrolyte uptake (520 %), ionic conductivity (2.71 $mS\cdot cm^{-1}$), as well as excellent mechanical strength (26.5 MPa). Similar to F-PI, the $-CF_3$ groups can also be attached to PEEK molecular chains to increase its affinity to polar electrolyte. As a result, Li/$LiFePO_4$ battery cell with F-PEEK separator shows 4.5 % higher initial discharge capacity compared to PEEK separator. Qi *et al.* [64] reported the physicochemical properties of electrospun poly(phthalazinone ether sulfone ketone) (PPESK) membrane as separator for LIB. Excellent liquid electrolyte uptake of 1210 % and ionic conductivity of 3.79 $mS\cdot cm^{-1}$ are achieved by PPESK separator due to its high porosity of 92 % and large pore size of 4.34 μm. More recently, Shi *et al.* [65] developed an inorganic electrospun SiO_2 monolayer separator for LIB with the advantage of "absolutely" thermal stability as it is flame-resistant. Li/$LiMn_2O_4$ battery cells with SiO_2 separators exhibit electrochemical stability up to 5 V; battery capacity retention of 87.5 % after 500 cycles at 1 C rate; and only slightly decrease of battery capacity at 10 C rate (about 70 % higher than a LIB cell with conventional PP separator).

As mentioned in the preceding, high porosity and large pore size of electrospun monolayer separator facilitate the liquid electrolyte retention and lithium ions transportation. However, such features may also lead to self-discharge, soft short circuit by dendrite growth and poor mechanical strength [66, 67]. Post-treatments such as mechanical press and/or heat treatment are applied as effective methods to increase the mechanical strength and long-term stability of electrospun separators under the premise of moderately decreasing the porosity and pore size. Jiang *et al.* [53] fabricated the electrospun PI separator and mechanical pressed the membrane separator under pressure of 1-5 MPa. Increasing the pressing pressure decreases the porosity of the PI separator from 87 % to 73 %, whereas the mechanical strength increases from 12 MPa to 31 MPa. When combined with lithium bis(oxalate) borate (LiBOB) based electrolyte, the Li/$LiFePO_4$ battery cell exhibits stable performance under high temperature. It retains 86 % of its discharge capacity after 50 cycles at 120 °C and 0.5 C rate, such feature is desired for some specific applications of LIBs, such as drilling tools for the oil drilling market. Kong *et al*. [55] heat treated the electrospun F-PI separator at 300 °C for 15 s to obtain the crosslinked fiber membrane as shown in Figure 2.4. After heat treatment, the pore size and porosity of F-PI separator decrease from 1.85 μm and 81.3 % to 1.14 μm and 73.4 %, respectively. But the tensile strength improved dramatically from 6.8 to 31.7 MPa. Similar effects of thermal treatment were also reported by Liang *et al*. [68] and Kong *et al*. [69] with electrospun PVDF and Polyetherimide (PEI) monolayer separator.

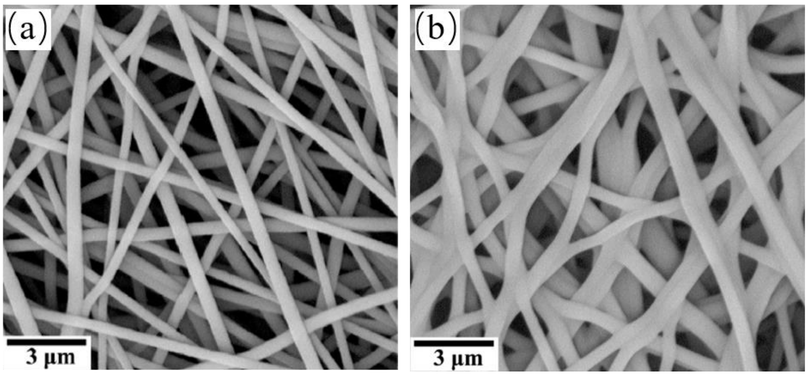

Figure 2.4. SEM images of electrospun F-PI membrane separator (a) before and (b) after thermal crosslinked at 300 °C [55]

2.1.2 Multilayer separators

Based on the unique operational features of electrospinning process, membrane with multilayer structure can be easily fabricated by sequentially spinning. Multilayer separators can attain optimal properties in mechanical strength [60, 70, 71], thermal stability[71-74] and battery performances[75, 76] by combining advantages of different fiber layers.

Polymer materials with superior mechanical strength, such as PMIA, PET and PAN, are reported as supporting layer in electrospun multilayer separators to provide sufficient mechanical strength. Zhai *et al*. [70] fabricated a PVDF/PMIA/PVDF tri-layer separator by sequentially electrospinning different nanofibers onto a same target collector. Due to the existence of the PMIA layer, the multilayer membrane separator exhibits superior properties than the monolayer PVDF separator. The tensile strength of the membrane separator increases from around 10 to 14 MPa, and meanwhile exhibits good dimensional stability under heat treatment of 180 °C. Li/$LiCoO_2$ battery cells contained the multilayer separator also show good capacity retention ratio of 93.1 % after 100 cycles. Peng *et al*. [77] electrospun PSA fibers on both sides of a PET mat to form multilayer separator for LIB. The supporting of the PET layer increased the tensile strength by 240 % to 17.7 MPa compared with monolayer PSA separator. Huang *et al*. [60] designed a multilayer separator with a SiO_2 ceramic layer been embedded in an electrospun PAN membrane. The risks of SiO_2 particles falling off during the separator handling and battery operation are diminished by the existence of electrospun PAN layers. The tensile strength of the as-prepared multilayer separators attains 7.1 MPa, and the graphite/$LiNi_{1/3}Co_{1/3}Mn_{1/3}O_2$ battery contained this separator showed stable cycling ability as 91 % of the capacity retained after 75 cycles. Notably, the poor thermal stability of electrolyte-soaked electrospun PAN separator [59] is also improved by the inserting of SiO_2 layer. After soaking with electrolyte, the multilayer separator exhibits only 2 % of shrinkage at 140 °C.

In a multilayer separator, PVDF [70, 72, 73] and PE [71, 78] layers are often designed as a thermal shutdown layer, due to their relatively low melting temperature, to improve the battery safety. Once a battery cell been overheated or when short circuit occurs, the function layer can thermally close its pore structure and cut down the migration of lithium ions thus prevent the battery from further heating. Wu *et al*. [73] studied the thermal shutdown behavior and morphologies changes of an electrospun multilayer PI/PVDF/PI separators under different heating temperatures. The embraced PVDF layer melts at 170 °C to form a pore free film layer. Due to the support of the PI layers, the multilayer separator only shows a 2.7 % shrinkage after the heat treatment. The shutdown function is validated by the battery tested with the multilayer separator. After heat treat the separator at 170 °C, the battery charging current sharply decreased to zero, and the discharge capacity is only 7 % of the cell with original separator. The results indicate that the thermal shutdown function of the as-prepared electrospun multilayer separator could serve as the safety mechanism to defend the thermal runaway issue of LIB. Liu *et al.* [71] fabricated multilayer membrane separator by electrospinning PI/SiO_2 fibers on both side of a microporous PE membrane using a needleless electrospinning set up. Due to the melting temperature differences between PI and PE layers, the multilayer separator is thermally shut down at temperatures above 131 °C. Li/$LiCoO_2$ battery cells with this multilayer separator exhibits wide electrochemical stability window as the electrochemical oxidation limit attains 5.3 V, and retained 83.5 % of its discharge capacity after 100 cycles at 0.2 C rate.

Besides the preceding introduced triple layer sandwich like separators, asymmetrical two-layer electrospun separator are also proposed to enable desired functions. Wang *et al.* [75] fabricated a bilayer separator to provide overcharge protection for LIB by first electrospinning PFO-DMP/PEO fibers onto the collector and then spinning P3BT/PEO polymer fibers directly onto the surface of the PFO-DMP/PEO mat. PEO component was then removed by sonication in deionized before battery assembling due to the PEO polymer being unstable above 4 V. The PFO-DMP layer, which has a high oxidation voltage, is placed in contact with the cathode to set a high protection voltage. The P3BT layer, has a lower oxidation voltage, is placed next to the anode to protect the PFO-DMP layer from degradation at the anode potentials. The Li/$Li_{1.05}Mn_{1.95}O_4$ battery cell contains such separator retained stable discharge capacity under 135 % overcharge conditions for well over 1000 cycles. Oh *et al.* [76] fabricated a bilayer dual (ion/electron)-conductive/chemically active separator by concurrent electrospraying and electrospinning process. The top layer which contains PEI fibers and multi-walled carbon nanotubes (MWNT) is both ionic and electron conductive. Thus, it acts as an “upper current collector” in LIB. This dual-conductive feature expedited the redox kinetics of the cathode and improved the discharge capacity, rate performance, and capacity retention of battery cells. The support layer contained PVP/PAN nanofiber skeletons and SH-silica particles can trap heavy metal ions dissolved from lithium metal oxide cathode materials. Once such metal ions migrate to anode will be electrochemically reduced to heavy metals and cause serious degradation of capacity during battery cycling. In the as-prepared separator, PVP can scavenge heavy metal ions due to its pyrrolidone groups having Lewis basicity [79], moreover, thiol groups of SH-silica can react with heavy metal ions to form metal-thiol complexes via their lone pair electron-mediated coordination bonds [80]. As a result, after 50 cycles of battery operation, the deposited heavy metal concentration on the anode was substantially mitigated in battery contained this bilayer separator (17 ppm) compared with a conventional PE separator (105 ppm).

2.1.3 Modified separators

The structure and surface morphology of the electrospun separator can be modified with post-treatment to further improve its physical and electrochemical properties. Dip-coating is the most widely applied method to modify electrospun separators. By immersing the separator into a coating solution for a period, the introduced coating materials adhere to the nanofibers thus affecting the separators properties [81]. Cao *et al*. [82] and Shi *et al*. [83] reported the use of PDA solution as a dip-coating solution to modify the PVDF and PVDF-HFP electrospun separators, respectively. PDA, commonly found in mussel adhesive proteins, is a small molecule compound containing catechol and amine groups which establishes covalent and non-covalent interactions with the surface of organic materials. Figure 2.5 (a) shows the surface morphology of the PVDF-HFP electrospun membrane after PDA coating. The network structure of the electrospun membrane maintain the same after the dip-coating process, meanwhile, a thin layer of PDA was deposited on the surface of the nanofibers. Due to the PDA bonding between PVDF-HFP fibers, the mechanical tensile strength of modified separator increases from 7.1 MPa to 11.2 MPa in dry state and

3.5 MPa to 7.1 MPa in wet state, respectively. The dip-coating modification also improves the thermal stability of the PVDF-HFP membrane separator as the modified membrane is capable of maintaining its pore structure at temperatures up to 170 °C. The Li/$LiMn_2O_4$ cell contained the PDA coated PVDF-HFP separator exhibits stable battery cycling performance as the discharge capacity remained 99.1 % after 100 cycles. However, the PDA coating is a detriment to electrolyte affinity, leading to 25.1 % decrease in ionic conductivity compared with PVDF-HFP separator. Liang *et al*. [84] reported the use of PEO as coating solution for electrospun PI separator modification. Due to the stable complex formed between PEO and lithium salt [85], the ionic conductivity of electrospun PI separator is improved from 1.87 to 3.83 $mS \cdot cm^{-1}$ after dip-coating process. The PEO coated PI separator decreases the electrode–electrolyte interfacial resistance of Li/$LiFePO_4$ battery cell by 55.6 % compared with uncoated PI separator, leading to the improved low temperature discharge capacity retention ratio of 75 % at 5 C at 0 °C (capacity retention ratios are 53.3% and 3.8% for LIB with PI and commercial separator, respectively).

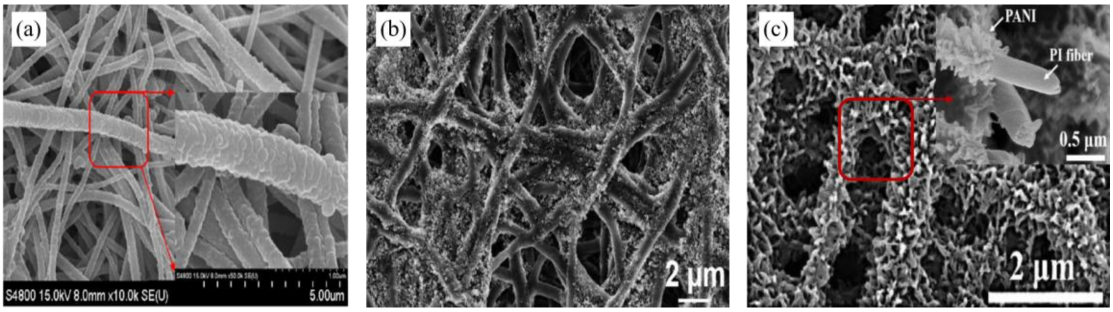

Figure 2.5. SEM images of electrospun separators after modification (a) PVDF-HFP membrane fibers dip-coating with PDA [83] (b) PEI-PU membrane fibers dip-coating with SiO_2 [86] (c) PI membrane fibers adhered with PANI nanowires [87]

Dip-coating solutions containing ceramic nanoparticles are also widely studied to modify electrospun separators. The addition of nanosized ceramic nanoparticles can reduce the crystallinity of electrospun polymer membrane and also react with polar electrolyte due to Lewis acid-base interactions, leading to promote the migration of lithium ions. Zhai *et al*. [86] fabricated the electrospun PEI-PU composite separator and followed by dip-coating with SiO_2/PVDF-HFP (mass ratio of 10:1) dispersion. As shown in Figure 2.5 (b), SiO_2 nanoparticles are filled into the interstices between the electrospun fibers with PVDF-HFP as binders, leading to improved tensile strength of 15.7 MPa but decreases the average pore size and porosity from 1.8 μm to 544 nm and 82.2 % to 59.1 %, respectively. Moreover, the ionic conductivity of the electrospun PEI-PU separator increases from 1.47 to 2.33 $mS{\cdot}cm^{-1}$ after modified with SiO_2 particles. Liang *et al*. [88] studied the performance of PI separator coated with SiO_2/Al_2O_3 particles. Similarly, the addition of nanoparticles sacrifices the porosity and electrolyte uptake amount of PI separator but improves the ionic conductivity from 1.81 to 2.92 $mS{\cdot}cm^{-1}$. The Li/$LiFePO_4$ battery cell with the modified separator maintains the greatest discharge capacity over various discharge rate from 0.2 to 20 C rate compared to uncoated PI and commercial separators.

Although most works focused on the dip-coating process, efforts have also been taken on the modification of electrospun separator through other methods. Ye *et al*. [87] applied an *in-situ* polymerization method to modify electrospun PI membrane with PANI nanowires. After immersing the PI membrane in AN solution for 30 min, the polymerization was carried out in an ice-water bath for 4 h to form the PI/PANI membrane. As shown in Figure 2.5 (c), the modified membrane exhibits a hierarchical 3D structure, where the PANI nanowires uniformly grew on PI nanofibers. Due to the good ion affinity of PANI nanowires, even though the modification of PI separator decreased the porosity and electrolyte uptake amount, it still improved the ionic conductivity from 1.03 to 2.33 $mS{\cdot}cm^{-1}$. Compared with PI and commercial separator, Li/$LiFePO_4$ battery cell with PANI modified separator maintains the highest discharge capacity with increased C-rate from 0.1 to 10 C. Stable Li/$LiFePO_4$ battery cycling performance is also achieved as 89.3 % of capacity retained after 500 charge/discharge cycles at 0.2 C rate. Similar modification strategy was also applied by Park *et al.* [89] to modify electrospun PAN separator with SiO_2 particles. The electrospun PAN separator was first immersed in a solution contained 5 wt% vinyl-functionalized SiO_2 particles and 10 wt% TEGDA, and then been heated at 80 °C for polymerization between reactive SiO_2 particles and TEGDA. The modification process enhances the tensile strength of PAN separator from 4.5 to 7.7 MPa and improves the ionic conductivity from 1.4 to 2.1 $mS\cdot cm^{-1}$. Shen *et al.* [90] applied atomic layer deposition (ALD) technique to modify electrospun PVDF-HFP separator with Al_2O_3 particles. The prepared electrospun membrane is first treated by the plasma enhancement to form oxygen-derived free radicals on the polymer surface. Then, in an ALD equipment, $Al(CH_3)_3$ and water are used as the alumina precursor and oxygen source, respectively. The obtained modified membrane separator presents a core-shell structure as about 30 nm of Al_2O_3 shell evenly deposited on the surface of each PVDF-HFP fiber. Due to the thermal stability of the introduced ceramic particles, the modified membrane separator is able to maintain its dimension and porous structure at temperatures up to 270 °C, which lead to obtain stable open circuit voltage of battery cell operated at 160 °C.

2.1.4 Composite separators

Another effective method to enhance the performance of electrospun separators is the addition of multiple organic polymers and inorganic fillers into an electrospinning solution to directly fabricate composite nanofibers. Due to the different physical and electrochemical properties of different polymers, the composite electrospun separators containing multiple polymer materials normally have desired properties compared to separators derived from only one polymer precursor [32, 91, 92]. Moreover, it is also known that introducing of inorganic particles to membrane separator can effectively enhance the thermal stability and the electrolyte affinity due to their stable thermal properties and great hydrophilicity [28, 93].

The directly blending of two polymer solutions for electrospinning is a simple way to produce composited electrospun separators. Xiao *et al*. [91] studied the properties of composite separator by electrospinning the mixture of PMIA and PU solutions. The PMIA is selected for its high thermostability while PU contributes to the high ionic conductivity of the composite separator [94]. By increasing the PMIA/PU weight ratio in the electrospinning solution, the average fiber diameter of the composite separator decreases gradually from 292 to 217 μm, and the tensile strength decreases from 25.2 to 15.8 MPa. Except for the PMIA/PU ratio of 2/8, the PMIA/PU composite electrospun separator also shows stable cycling performances in LIB. Zhao *et al*. [92] fabricated an electrospun composite separator with PAN and lignin. Lignin is the second most abundant component in nature with properties like biodegradability, biocompatibility and low cost. With increasing the lignin content ratio in the electrospinning solution from 0-50 %, the porosity of the obtained composite separator also increases, leading to the electrolyte uptake amount in the separator improves from 368 to 790 %. However, at the highest lignin ratio of 50 %, the LIB with such prepared separator exhibits relatively low capacity and decreased sharply with battery cycling, due to the fact that some of the lignin dissolves in the electrolyte and causes the battery system unstable.

Apart from the direct blending method, the co-electrospinning process has also been studied to produce composite membrane separator. With multiple needles separately eject different polymer solutions to the same collector, the obtained composite membrane is expected to combine advantages of different polymers and meanwhile keep their own raw properties [95]. Chen *et al*. [32] fabricated PVDF-HFP/PI composite nanofiber membrane for LIB separator via co-electrospinning process. After thermal calendaring the obtained composite membrane at 135 °C under 1MPa, the PVDF-HFP fibers partially melted due to its low melting temperature and served as bonding fibers, resulting in the improved tensile strength of the composite membrane from 2 MPa to 7.5 MPa. A similar approach was also reported by Zainab *et al*. [96] with co-electrospun PAN/PU composite separator. Improved ionic conductivity (2.07 $mS\cdot cm^{-1}$), tensile strength (10.4 MPa) and electrode stability up to

5.1 V are observed by the resultant membrane separator.

Core-shell structured composite membrane separator fabricated by coaxial electrospinning apparatus (with concentrically configured needle) have drawn research attention in recent years due to its unique structure. Generally, the core material is designed to provide thermal stability and mechanical strength, while the shell material contributes to the electrochemical stability and electrolyte affinity [97-99]. Huang *et al.* [33] extracted cellulose acetate from waste cigarette filter, and used it in a coaxial-electrospinning process to fabricate cellulose@PVDF-HFP composite membrane as LIB separator. As shown in Figure 2.6 (a), the cellulose nanofibers are fully wrapped by the PVDF-HFP to form core-shell structured composite membrane separator. The obtained membrane exhibits good tensile strength of 34.1 MPa, thermal dimensional stability to 200 °C as well as high ionic conductivity of 6.13 $mS \cdot cm^{-1}$. Jiang *et al.* [100] reported a core-shell composite separator with thermal shutdown function by using PLA and PBS as core and shell materials, respectively. Due to the melting of PBS shell, a complete occlusion of the composite membrane is observed after treating the membrane at 130 °C, whereas the PLA core polymer serves as a stable skeleton to maintain the dimensional integrity. This feature is expected to improve the battery safety by cutting off the lithium pathways and avoiding the battery short circuit under thermal abuse conditions. Liu *et al.* [101] reported another strategy to improve battery safety under harsh condition by using electrospun core-shell separator with flame-retardant property. TPP, a popularly used flame retardant, is used as fiber core with PVDF-HFP designed as the fiber shell. Once the temperature raises up to 160 °C, the PVDF-HFP shell melted to release the encapsulated TPP into the electrolyte, in order to prevent the flammable electrolyte from igniting.

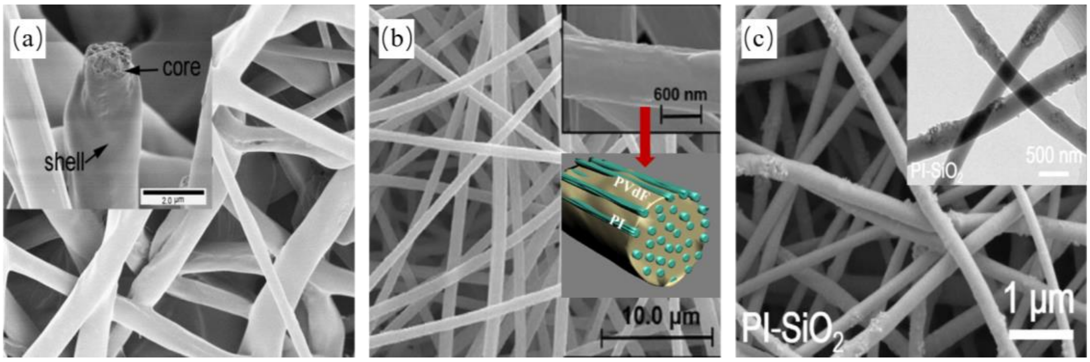

Figure 2.6. SEM images of electrospun composite separators (a) cellulose-core/PVDF-HFP-shell composite membrane [33] (b) multi-core/shell structured PI/PVDF composite membrane [102] (c) PI-SiO$_2$ composite membrane separator [103]

The fabrication of core-shell electrospun separator is not limited to using coaxial electrospinning. Park *et al*. [102] reported that the core-shell structure can also be naturally formed by using one electrospinning solution containing two immiscible polymers (*e.g.* PVDF/PI) through a single needle nozzle. After selectively removing PVDF component by solvent extraction with acetone, the morphology of the remained PI fibers is observed as ultrafine fibrils with diameters of 100-200 nm. This result indicates that the electrospun PI@ PVDF separator is multi-core/shell structured with PI core fibers being fully embedded by PVDF as shown in Figure 2.6 (b). The authors considered that the multi-core/shell structure is formed due to the complete isolation of PI and PVDF polymer phases. As the two phases mixed homogenously in the liquid solution, multiple small PI droplets are formed and coalesced into large droplets. Then, the PI droplets started to transform into core strings when the polymer solution is subjected to flow through the syringe capillary during electrospinning, which eventually lead to the formation of multiple PI ultrafine strings and PVDF outer shells. The as-prepared composite membrane separator exhibits stable thermal and electrochemical properties. The average MCMB/LiCoO$_2$ battery capacity decay rate for 500 cycles was reported as 0.03 mAh/g/cycle.

In addition to incorporate multiple organic polymer precursors, another important approach to prepare composite electrospun separator is to introduce inorganic nanoparticles. The most widely used inorganic particles, including SiO_2 [103-107], TiO_2 [108-110], Al_2O_3 [104] and $MgAl_2O_4$ [111], can be dispersed into the electrospinning solutions with different polymers. Figure 2.6 (c) shows the typical morphology of an electrospun composite membrane with inorganic nanoparticles. The fillers are mainly embedded inside the fibers with some amount dispersed on the fiber surfaces. The adding of these inorganic nanoparticles is effective to improve the ionic conductivity of the composite separator due to Lewis acid/base interactions between the filler surface, polar groups of the polymer and the ionic species in the liquid electrolyte [112, 113]. In several studies [27, 105, 108], the increase of nanoparticle concentration in the electrospinning solution is reported to cause the formation of thinner nanofibers and rough surface morphology, which improved the porosity and electrolyte uptake of the composite membrane separator. Liu *et al.* [71] explained this phenomenon from two aspects. On the one hand, the inserted nanoparticles between the polymer chains weaken the intermolecular Van der Waals' force, resulting in the decrease of solution viscosity and surface tension, thus leading to the formation of finer fibers during the electrospinning process [114]. On the other hand, ceramic nanoparticles, such as SiO_2, can be easily charged but hard to discharge. Therefore, the electrostatic charge on the composite solution droplet is increased during the electrospinning, which results in the enhanced radial Coulombic force and whipping motion of the spinning jets, thus also leads to thinner nanofibers.

Yanilmaz *et al.* [108] compared the performances of electrospun nylon 6,6 composite membranes containing SiO_2 and TiO_2 nanoparticles, respectively, as LIB separator. By adding 12 wt% SiO_2 and TiO_2 into Nylon 6,6 solution, the average fiber diameter of the obtained electrospun membranes decrease from 463 nm to 218 and 312 nm, respectively, which increases the membrane porosity and electrolyte uptake. The ionic conductivity of the SiO_2/Nylon composite membrane reaches 3.6 $mS \cdot cm^{-1}$ at room temperature, which is

28.6 % and 350 % higher than a single electrospun Nylon 6,6 and conventional microporous membrane separator, respectively. Due to the interaction between the nanoparticles and polymer matrix, the inserted SiO_2 and TiO_2 nanoparticles also enhance the tensile strength of electrospun Nylon membrane from 18 MPa to about 22 MPa. The electrospun SiO_2/TiO_2 composited Nylon 6,6 membrane separator exhibited stable battery cycling performances in both $Li/LiCoO_2$ and $Li/LiFePO_4$ cells. Generally, the integrating of the ceramic nanoparticles into polymer electrospinning solutions requires intensive sonication to ensure even dispersion of the particles [28]. Also, the concentration of the added nanoparticles is restricted to a relatively low level, due to the risk that the aggregation of nanoparticles at a high loading may cause poor battery cycling performances [115]. To this end, Smith *et al.* [116, 117] proposed the use of organopolysilazane (OPSZ) as ceramic precursor to fabricate PAN/polymer-derived ceramic composite membrane separator through electrospinning process. The OPSZ is fully miscible with PAN, the composite electrospinning solution is homogeneous without the need for an additional preparation process even at high ceramic loadings. During the electrospinning, OPSZ precursors are converted to polymer-derived ceramics via moisture crosslinking, and then well distributed within the PAN fibers. The experiment results confirm that the ceramic nanoparticles are mainly wrapped inside the fiber and forming an interconnected ceramic network with a thin layer of ceramic were appeared on the fiber surface. With 70:30 wt.% of PAN/precursor, the composite separator shows 93 % of capacity retention in a graphite/$LiCoO_2$ battery cell over 100 cycles. Recently, Jiang *et al.* [109] reported an electrospun PVP/TiO_2 composite membrane with an attractive thermal on/off function. The composite polymer solution was ejected with mineral oil through a coaxial electrospinning process. After removing the mineral oil from the fiber core, the obtained composite fiber presents hollow tubular structure. Due to the phase transition of PVP at temperature range from 60-90 °C, the reactions between PVP and liquid electrolyte close the pore structure of the separator at 60 °C. However, the structure of the porous membrane can be restored on the TiO_2 skeletons after temperature dropped to room temperature. As a result, the LIB cell containing PVP/TiO_2 composite separator exhibits a reusable temperature-dependent on/off function when the battery temperature reached 60 °C.

To further improve the mass transfer efficiency of lithium ions in LIB, Liang *et al.* [118, 119] fabricated electrospun PAN composite membrane separator with the addition of ionic-conducting ceramic particles. By adding 15 wt.% of LLTO and LATP, the ionic conductivity of the electrospun PAN separator improves from 0.87 to 1.95 $mS{\cdot}cm^{-1}$ and from 0.64 to 3.6 $mS \cdot cm^{-1}$, respectively. Huang *et al.* [34] fabricated electrospun cellulose@PVDF-HFP core-shell composite separator and introduced the LLTO particles into the fiber shell. The integrated 8% LLTO significantly improves the ionic conductively of the electrospun separator from 2.08 to 13.90 $mS{\cdot}cm^{-1}$, leading to the greater battery discharge capacity of 155.6 $mAh{\cdot}g^{-1}$ compared to LIB cells with cellulose@PVDF-HFP separator (139.9 $mAh{\cdot}g^{-1}$) and commercial separator (114.8 $mAh{\cdot}g^{-1}$) at 0.2 C rate.

Organic-inorganic hybrid nanoparticles have also been integrated with electrospun polymer separator for LIB. Chen *et al.* [120] introduced octaphenyl-polyhedral oligomeric silsesquioxane (OPS) particles into PVDF polymer matrix through electrospinning. OPS molecular has organic-inorganic intramolecular hybridization feature with a special cage-shaped core-shell structure [121]. The core of OPS is an inorganic kernel connected by silicon and oxygen element, leading to the features of inorganic nanoparticles such as electrolyte affinity, thermal and oxidative stability. Meanwhile, the vertices of OPS molecular can link with organic groups, which enhanced the compatibility between the nanoparticles and polymer matrix. Due to the smaller dimensions of OPS particles (1-3 nm) than traditional inorganic nanoparticles, small amount of OPS addition can effectively modify the physical and chemical properties of polymer membranes. With only 2 wt.% of OPS particles integrated with electrospun PVDF separator, the tensile strength of the obtained membrane increases from 1.6 to 12.7 MPa, and ionic conductivity increases from

1.4 to 4.2 mS·cm^{-1}. The Li/LiCoO$_2$ battery cell with this composite separator shows higher discharge capacity of 148.5 mAh·g^{-1} compared to original electrospun PVDF separator (102.3 mAh·g^{-1}) at 0.5 C rate. Similar results were also reported by Zhao *et al*. [122] with electrospun PMIA/OPS composite separator. With 2 wt.% OPS added, the average fiber diameter of the obtained membrane decreases by 46.6 %, whereas the tensile strength and ionic conductivity increases by 103.7 % and 221.7 %, respectively. The Li/LiCoO$_2$ cell with PMIA/OPS separator presents enhanced discharge capacity of 157.9 mAh·g^{-1} at 0.5 C, and stable battery performance as 89.04 % capacity retained after 100 battery cycles.

2.2 Methods to integrate PPy with electrospun nanofibers

As stated in Section 1.2, this thesis is motivated to develop redox-active separators by integrating PPy with electrospun nanofibers. PPy is a type of electrically conductive polymer with redox-activity, which can be produced by the polymerization of pyrrole (Py) using chemical oxidants or electropolymerization of pyrrole solution. However, pristine PPy is an insoluble and brittle solid in the forms of particles or dense film, which limits its direct use in electrospinning as sole polymer precursor (electrospinning requires the polymer precursor to be dissolved as viscous solution). Therefore, the following methods are proposed to integrate PPy with electrospun nanofibers.

2.2.1 Co-electrospinning PPy particles with driven polymer

Co-electrospinning PPy particles with a driven polymer is a simple and straight-forward method to produce PPy composite nanofibers. The principle of this method is the same as the electrospinning method to produce composite separator with nanoparticle fillers as introduced in the Section 2.1.4.

Chronakis *et al*. [123] reported the fabrication of PEO/PPy composited nanofibers. A solution with a PPy:PEO weight ratio of 1.0-4.0 was prepared for the electrospinning process. The diameters of the produced nanofibers are in the range of 70-300 nm. Increasing the PPy content in PPy/PEO nanofibers resulted in the increasing of electrical conductivity from 4.9×10^{-5} to 1.2×10^{-2} mS·cm^{-1}. Instead of directly adding pre-prepared PPy particles into spinning solution, Cetiner *et al.* [124] prepared the spinning solution by polymerizing Py on P(AN-co-VAc) matrix. In the presence of $Ce(NO_3)_6$ oxidant, Py and the driving polymer P(AN-co-VAc) with initial mass ratio of Py/P(AN-co-VAc) ranging from 5% to 20% were added into the spinning solution. The resultant PPy composite nanofibers exhibited a diameter of 290 nm and conductivity of 2.3×10^{-4} mS·cm^{-1}.

Zhao *et al.* [125] fabricated the PPy particles with dopants for co-electrospinning. Four different dopants, including toluene sulfonate (TSNa), dodecyl-benzene sulfonic acid sodium salt (DBSNa), dodecyl sulfonic acid sodium salt (DSNa), and di-(2-ethylhexyl) sulfosuccinate sodium salt (DEHS), were blended with pyrrole, respectively, to prepare doped PPy particles. Then, the spinning solution containing doped PPy particles and PVA (mass ratio of 1:1) were used for electrospinning. Due to the additional electrons provided by dopants, the mobility of electrons in the conductive band of PPy molecular is improved [126]. As results, the obtained PPy based composite nanofibers exhibit electrical conductivity of 1.6×10^{-3} to 2.2×10^{-3} mS·cm^{-1}.

Tavakkol *et al.* [127] reported a novel route for fabricating PPy-base nanofibers using co-electrospinning. Instead of polymerizing pyrrrole before electrospinning process, the pyrrole monomers were mixed with PVP (PVP/pyrrole: 9%-91%) for electrospinning, followed by post-polymerization of PPy by a one-step or two-step process. In the one-step process, the electrospun Py-PVP nanofibers are directly collected in an oxidizing ethanol bath containing $FeCl_3$ and dopant (anthraquinone-2-sulfonic acid sodium salt (AQSA) or p-Toluene sulfonic acid (PTSA)). For the two-step process, the electrospun Py-PVP-dopant nanofibrous webs are first pealed from the aluminum foil collector and then immersed into a $FeCl_3$ bath for polymerization. The experimental results show that the one-step process leads to the higher electrical conductivity (522 mS·cm^{-1}) of the final PPy composite membrane compared to the two-step process (198 mS·cm^{-1}).

2.2.2 Electrospinning of soluble PPy modified by surfactant

Adding surfactant of large molecules is effective in improving the PPy solubility. This is because the inserting of surfactant weakens the inter-chains interactions of PPy, which eventually improves the solubility of the PPy polymer [126]. Thus, it is feasible to prepare the spinning solution of soluble PPy and use it for electrospinning to produce PPy nanofibers.

Kang *et al*. [128] first reported the electrospinning of soluble PPy nanofibers prepared by using ammonium persulfate (APS) as oxidant and dodecylbenzene sulfonic acid (DBSA) as surfactant. The addition of surfactant effectively improves the solubility of PPy particles in chloroform solvent. However, the electrical conductivity of the produced PPy particles decreased after adding the surfactant. The produced electrospun nanofibers exhibit a conductivity of 5×10^{-2} mS·cm^{-1}, which is higher than that of a cast film (3×10^{-2} mS·m^{-1}) derived from the same precursor. This is possibly because of the more consistent molecular orientations of PPy chains induced during the electrospinning.

Ju *et al*. reported the application of PPy based nanofibers in LIB as the cathode [129]. Soluble PPy was prepared by adding DBSA as a surfactant and $FeCl_3$ as an oxidant to pyrrole monomer. The PPy particles were mixed with sulfonated-poly (styrene-ethylene-butylenes-styrene) (S-SEBS) (as binder) and Super P (as electrical conductor) in a solvent for electrospinning. The electrospun PPy based nanofiber cathode obtains electrical conductivity of 520 mS·cm^{-1}, and electrolyte–electrode interfacial resistance of 14 Ω. In the LIB half-cell testing, the electrospun PPy cathode achieves 80 mAh·g^{-1} discharge capacity, which is much higher than the cast film PPy cathode (48 mAh·g^{-1}). However, due to the relatively poor spinnability of the soluble PPy, it is difficult to continually produce nanofibers using this method. Other researchers also reported similar problems [123, 130].

2.2.3 PPy *in-situ* polymerizing on electrospun template

A feasible approach to fabricate PPy into various structures is *in-situ* polymerization of PPy onto different templates. For instance, Cu-TCPP nanosheets [131], textile fibers [132], and polyurethane foams [133] have been reported to implement as templates for *in-situ* polymerization process to fabricate PPy composites with different structures. Electrospun nanofibers have also been reported as a template for *in-situ* polymerization of PPy.

Lee *et al.* [134] reported the growth of PPy layer onto an electrospun polylactic-co-glycolic acid (PLGA) nanofiber template. The electrospun PLGA membrane was immersed in an aqueous solution containing monomer Py and oxidant $FeCl_3$ to form a PPy layer on nanofiber template. The resultant composited nanofibers exhibit core-shell structure with an average fiber diameter of 520 nm. The wall thickness of the PPy shell is about 85 nm thick. The electrical resistance of the PPy-based nanofiber membrane was 1.7×10^4 Ω/sq. Other researchers adopted similar fabrication method to produce PPy-based nanofiber membranes. These nanofiber membranes are used for various applications, including neural tissue[134-136], tissue regeneration [137], heavy metal adsorption [138], and photocatalyst [139], with electrical conductivities ranging from 57 to 10000 $mS\cdot cm^{-1}$.

Instead of *in-situ* polymerizing of PPy in liquid phase, some researchers used chemical vapor deposition (CVD) technique to coat PPy on electrospun nanofibers from the vapor phase. Nair *et al.* [140] investigated the effects of two chemical oxidants, $FeCl_3$ and $Fe(OTs)_3$, on the fabrication of PPy-based nanofibers. The oxidants were first blended in a polystyrene (PS) solution for electrospinning. Then, the obtained nanofiber membranes are exposed to saturated Py vapor to form PPy onto the fiber surface. Compared to $FeCl_3$ induced nanofibers (625 nm, 2 $mS\cdot cm^{-1}$), PPy based nanofibers derived from $Fe(OTs)_3$ presents greater average fiber diameter of 920 nm and electrical conductivity of 5 $mS\cdot cm^{-1}$.

2.3 Summary

In this chapter, Section 2.1 provides a detailed review of the electrospun battery separators to cover the state-of-art research progresses within the recent years. Electrospinning is a straight-forward and industry practicable technology to produce nanofibrous membranes. As a result, electrospun membranes gain increased attention for using as separators to improve LIB performances.

Monolayer separator prepared by only one precursor material is the simplest type of electrospun separator. Features like high porosities (typically above 70%), large specific surface areas (typically above 10 $m^2 \cdot g^{-1}$) and interconnected porous structures render electrospun monolayer separator with abilities to uptake large amounts of liquid electrolytes and offer effective lithium ions transport channels in LIB. Drawbacks such as weak membrane mechanical properties may pose a risk to the battery assembling and long-term stability, however, it can be improved by implementing post-treatment such as mechanical press and/or heat treatment.

Multilayer separator can be directly fabricated by sequentially electrospinning of different polymer precursor solutions. By combining advantages of different fiber layers, multilayer separators can readily achieve optimized membrane physicochemical properties as well as different separator functions such as thermal shutdown, flame-resistant, heavy metal ions capture, overcharge protection, *etc*.

Electrospun membrane separator can be modified by post-treatment processes, especially the dip-coating, to further improve its performances in LIB. The coated materials adhere to the nanofibers and alter the morphology of the fiber surface, leading to the improved physical and electrochemical properties of electrospun separator, including mechanical strength, thermal stability, electrolyte affinity, and ionic conductivity.

Electrospun composite separator derived from multiple polymer and inorganic filler precursors can generally provide optimal separator properties for LIB applications. Similar to the multilayer separator, the combination of different materials in a composite battery separator also renders novel design strategies for functional separator (with one material acting as an inert barrier and the rest to achieve functional properties).

Despite the solid progress achieved, most research works still focused on using inert materials to develop electrospun separators. However, for an advanced LIB design, separator can actually be rendered with additional practical functions (as introduced in preceding paragraphs) and even get involved in the battery reactions. Developing functional separator for advanced LIB is a promising future research direction. Thus, this thesis is aimed at developing redox-active separator based on electrospun nanofibers for further enhancing the battery capacity (as elaborated in Section 1.2). The electrospun material of PAN is selected in this thesis as a demonstration because of its superior spinnability. Since the redox-activity of the proposed separator is not stemmed from the electrospun fibers, the selection of the electrospun material is not restricted to PAN. Polymers such as PVDF, PI, PMMA, etc. (which exhibits superior performances as battery separator as introduced in Section 2.1) could also be adopted.

In addition, Section 2.2 briefly introduces three commonly adopted methods for integrating PPy with electrospun nanofibers. PPy is a type of electrically conductive polymer with redox-activity. The pristine PPy, produced by pyrrole chemical polymerization, is insoluble and brittle solid particles. Thus, a simple and straight-forward method to produce PPy composite nanofibers is co-electrospinning PPy particles with a driven polymer. However, the PPy particles are expected to be mostly embedded inside the electrospun fibers (similar to the co-electrospinning with other nanoparticles as discussed in Section 2.1.4) produced by this method. Only a few PPy particles can appear on the fiber surface. In addition, the use of PPy particles in the spinning solution is likely to cause clogging of the electrospinning needles, due to the aggregation of PPy particles at high concentration. Thus, this method is not suitable to produce electrospun nanofibers with considerable amount of PPy loading.

Electrospinning of soluble PPy can produce PPy electrospun nanofibers. The adding of certain surfactants can improve the solubility of PPy, thus enables the direct electrospinning from PPy solution. However, the poor spinnability of the PPy solution is still a challenge. It is difficult to maintain continually stable nanofiber production using this method.

In-situ polymerization is a feasible method to integrate PPy with electrospun nanofibers. First, nanofibrous membrane is produced by electrospinning. Then, it is adopted as a template for pyrrole *in-situ* polymerization. The resultant membrane obtains core-shell fibrous structure with the electrospun nanofiber as core and PPy as shell. The fabrication process can be stable and controllable; thus, this method is adopted in this thesis to develop redox-active separator which is based on PPy composite electrospun nanofibers.

Chapter 3

Numerical Modeling of the Effects of Separator on the Performances of LIB

3.1 Introduction

Numerous researchers have experimentally studied battery materials to improve LIB performances. Blomgren [141] summarized related works by a comprehensive review of LIB technologies developed over the past decades. This review article published in 2017 was devoted to the 25th anniversary of the first commercial LIB battery in the world. Research and development in many aspects of LIB materials, including electrodes, electrolyte, separator, and current collectors, continues improving the battery economics, energy capacity, and safety features. However, the experimental works are normally time-consuming and costly.

Alternatively, numerical models have been developed over the past decades for the optimization of battery design parameters [142-144]. These LIB models enable more comprehensive understandings of battery parameters that cannot be directly measured. For example, local current density, electrolyte concentration distribution, and heat generation can only be determined numerically. [145, 146].

On the other hand, earlier modeling works are mainly focused on battery cathodes and anodes. Suthar *et al*. [147], for example, investigated the effects of anode porosity, thickness, and tortuosity on the battery capacity fade mechanisms using isothermal electrochemical models. They reported that a thinner anode with less porous and more uniform tortuosity results in more stable battery discharge capacity. Later, Miranda *et al.* [148] simulated the influence of cathode materials, including active electrode material, binder, and conductive additive, on the LIB performances. They also optimized the content balance of cathode components using their models. In addition, Hosseinzadeh *et al*. [149] studied the effects of multi-layered porous cathode on the performance of LIB by a 3D electrochemical-thermal model. They suggested to improve the battery energy density and to reduce heat generation using cathodes with multi-layered porosity distribution. Despite these earlier studies, there is a lack of fundamental modeling work to study the impact of separator on LIB performances.

Admittedly, many researchers reported their experimental works for the development of superior separators for LIBs. Lee *et al*. [7] provided a comprehensive review for such experimental works focused on LIB separators; they summarized the influences of types of separators on LIBs. In addition, Section 2.1 reviews the electrospun nanofiber-based separators with a focus on the properties of fiber-based separators and the battery performances of using such separators. To the best of our knowledge, all lab-scale experimental studies on the battery separators were carried out using coin cell batteries. These coin cell batteries, however, are structurally different from the most widely-used commercial LIBs, which have cylindrical cells [150]. Therefore, a modeling study is needed to analyze the impact of separator designs on the performance of commercial cylindrical LIBs.

This chapter presents a two-dimensional electrochemical-thermal coupled model for the separator in a 38120 cylindrical $LiFePO_4$ LIB. This type of commercial battery is used for many applications including electrical vehicles [151]. This model is first validated with experimental data obtained from literature. Then, the validated model is used to study the impact of separator design parameters, including thickness, porosity, thermal conductivity, and heat capacity, on the battery electrochemical and thermal performances.

3.2 Model Development

3.2.1 Model domain and assumptions

Figure 3.1 illustrates the cylindrical domain of the electrochemical-thermal model developed for this study. The electrochemical simulation of a single $LiFePO_4 | Li_xC_6$ battery cell is on the basis of a widely accepted pseudo two-dimensional model [152]. The physical model includes a battery anode, a cathode, a separator, and two current collectors. The heat generation obtained from the electrochemical model is coupled with a 2D axisymmetric thermal model as heat source to simulate the thermal behavior of the cylindrical battery unit.

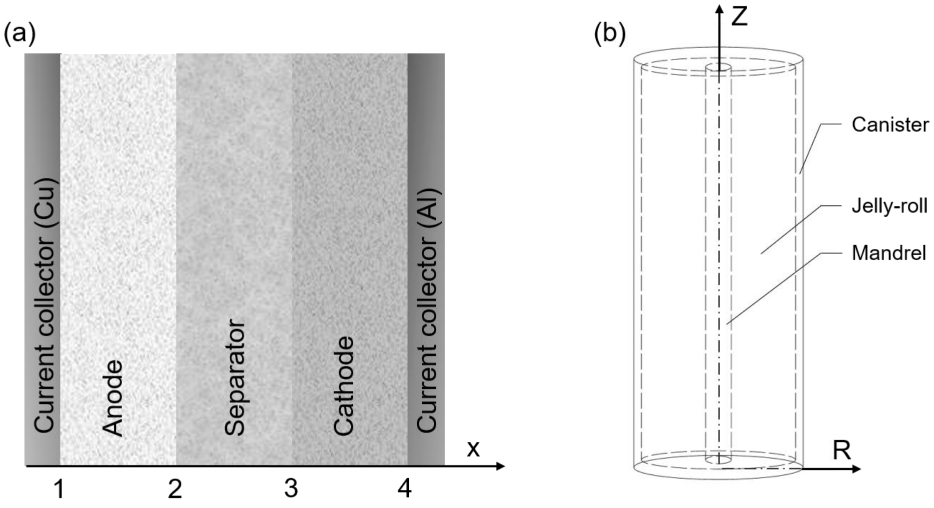

Figure 3.1. Schematic graph of lithium-ion battery for (a) electrochemical and (b) thermal model development

The model assumptions are as follows:

a. The active electrode material in cathode and anode are composed of spherical particles with uniform diameter.
b. The electrochemical reactions along the axial direction are homogenous.
c. The side reactions are negligible.
d. All battery components are well immersed into the liquid electrolyte.

These assumptions are valid and introduce little errors to the model results as discussed in Section 3.3.1.

3.2.2 Governing equations

3.2.2.1 Electrochemical kinetics

The local current density, $j_{n,i}$, on the electrode particle surface is calculated using the Butler-Volmer equation [144]:

$$j_{n,i} = j_{0,i}\left[\exp\left(\frac{\alpha_{\mathrm{a,i}}\mathrm{F}}{RT}\eta_i\right) - \exp\left(-\frac{\alpha_{c,i}\mathrm{F}}{RT}\eta_i\right)\right] \tag{3.1}$$

$$j_{0,i} = Fk_i c_l^{\alpha_{a,i}}\left(c_{s,\max,i} - c_{s,surf,i}\right)^{\alpha_{a,i}} c_{s,surf,i}^{\alpha_{c,i}} \tag{3.2}$$

$$\eta_i = \phi_{s,i} - \phi_{l,i} - U_{eq,i} \tag{3.3}$$

$$U_{eq,i} = U_{eq,ref,i} + \frac{\partial U_{eq,i}}{\partial_T}\left(T - T_{ref}\right) \tag{3.4}$$

Where *i=a, c*, denotes to anode and cathode, respectively; $U_{eq,ref,i}$ and $\frac{\partial U_{eq,i}}{\partial_T}$ are the open circuit potential of electrodes and its temperature derivative at the reference temperature (T_{ref}); k_i is the reaction rate constant. $U_{eq,i}$ and $\frac{\partial U_{eq,i}}{\partial_T}$ for $LiFePO_4$ and Li_xC_6 electrodes are obtained from literature [153]; they are dependent on the electrode state of charge. k_i is calculated using the following two equations [154]:

$$k_a = 3\times10^{-11}\exp\left[-\frac{20000}{R}\left(\frac{1}{T} - \frac{1}{298.15}\right)\right] \tag{3.5}$$

$$k_c = 1.4\times10^{-12}\exp(-y)\exp\left[-\frac{30000}{R}\left(\frac{1}{T} - \frac{1}{298.15}\right)\right] \tag{3.6}$$

3.2.2.2 Mass conservation

The mass conservation of lithium ions in electrode particles is calculated using Fick's law [155]:

$$\frac{\partial c_{s,i}}{\partial t}=\frac{D_{s,i}}{r^2}\frac{\partial}{\partial r}\left(r^2\frac{\partial c_{s,i}}{\partial r}\right) \tag{3.7}$$

where $D_{s,i}$ ($i=a,c$) is the solid diffusion coefficients for anode and cathodes, respectively, and they are calculated using these two equations [145, 156, 157]:

$$D_{s,\mathrm{a}}=1.45\times10^{-13}\exp\left[\frac{68025.7}{R}\left(\frac{1}{318}-\frac{1}{T}\right)\right] \tag{3.8}$$

$$D_{s,\mathrm{c}}=1\times10^{-13}\exp\left[-\frac{35000}{R}\left(\frac{1}{T}-\frac{1}{298.15}\right)\right] \tag{3.9}$$

The corresponding boundary conditions are:

$$-D_{s,i}\frac{\partial c_{s,i}}{\partial r}=0\text{, at } r=0 \tag{3.10}$$

$$-D_{s,i}\frac{\partial c_{s,i}}{\partial r}=j_{n,i}\text{, at } r=r_{s,i} \tag{3.11}$$

The mass conservation of lithium ions in the electrolyte is calculated according to the concentrated solution theory, which is described by [155]

$$\varepsilon_{l,i}\frac{\partial c_{l,i}}{\partial t}=D_{l,eff,i}\frac{\partial^2 c_{l,i}}{\partial x^2}+A_i\left(1-t_+\right)j_{n,i} \tag{3.12}$$

$$D_{l.eff,i}=D_l\varepsilon_{l,i}{}^{brug,i} \tag{3.13}$$

$$A_i=3\varepsilon_{s,i}/r_{s,i} \tag{3.14}$$

where $i=a,c,p$, p denotes to the separator. $D_{l,eff,i}$ is the effective diffusion coefficient in the electrolyte phase, which is related to the material porosity $\varepsilon_{l,i}$. The diffusion coefficient for electrolyte is calculated as [145]

$$D_l = 10^{-4} \times 10^{-4.43 - \left(\frac{54.0}{T - 229.0 - 0.005 C_l}\right) - 2.2 \times 10^{-4} C_l} \tag{3.15}$$

The corresponding boundary conditions are

$$D_{l,eff,i} \frac{\partial c_{l,i}}{\partial x} = 0 \text{ at boundaries 1 and 4} \tag{3.16}$$

As shown in Figure 3.1 (a), the boundary numbers 1, 2, 3 and 4 denote the current collector-anode boundary, the anode-separator boundary, the separator-cathode boundary, and the cathode-current collector boundary, respectively.

3.2.2.3 Charge conservation

The charge conservation in solid electrode particles is governed by Ohm's law [155]:

$$i_{s,i} = -\delta_{eff,i} \frac{\partial \phi_{s,i}}{\partial x} \tag{3.17}$$

$$\delta_{eff,i} = \delta_i \varepsilon_{s,i}^{brug,i} \tag{3.18}$$

the boundary conditions are

$$\phi_{s,a} = 0 \text{, at boundary 1} \tag{3.19}$$

$$-\delta_{eff,i} \frac{\partial \phi_{s,i}}{\partial x} = 0 \text{, at boundary 2 and 3} \tag{3.20}$$

$$-\delta_{eff,i} \frac{\partial \phi_{s,i}}{\partial x} = i_{app} \text{, at boundary 4} \tag{3.21}$$

The charge conservation in liquid electrolyte is [154, 155]

$$i_{l,i} = -\kappa_{eff,i} \frac{\partial \phi_{l,i}}{\partial x} + \frac{2\kappa_{eff,i} RT \left(1\text{-}t_+\right)}{F} \cdot \frac{\partial \ln c_l}{\partial x} \tag{3.22}$$

$$\kappa_{eff,i} = \kappa_i \varepsilon_{l,i}^{brug,i} \tag{3.23}$$

$$\begin{aligned}\kappa_i &= 1.12\times10^{-4}(-8.25+0.0532T-2.99\times10^{-5}T^2+0.262C_l-9.31\times10^{-3}C_lT \\ &\quad +8.07\times10^{-6}C_lT^2+0.22C_l^{\,2}-1.77\times10^{-4}C_l^{\,2}T)\end{aligned} \tag{3.24}$$

The corresponding boundary conditions are

$$\frac{\partial \phi_{l,i}}{\partial x}=0\text{, at boundary 1 and 4} \tag{3.25}$$

3.2.2.4 Energy conservation

Three different types of heat are generated during the LIB charge and discharge[155], and they are reaction heat, Q_{rea}, ohmic heat, Q_{ohm}, and active polarization heat, Q_{act}. Their calculations are listed as follows, respectively [158].

$$Q_{rea}=A_iFj_{n,i}T\frac{\partial U_{eq,i}}{\partial T} \tag{3.26}$$

$$Q_{ohm}=\delta_{eff,i}\left(\frac{\partial \phi_{s,i}}{\partial x}\right)^2+\kappa_{eff,i}\left(\frac{\partial \phi_{l,i}}{\partial x}\right)^2+\frac{2\kappa_{eff,i}RT}{F}\left(1-t_+\right)\frac{\partial \ln c_i}{\partial x}\frac{\partial \phi_{l,i}}{\partial x} \tag{3.27}$$

$$Q_{act}=A_iFj_{n,i}\eta_i \tag{3.28}$$

Then, the calculated heat generations were applied as heat source to simulate the thermal behavior of the cylindrical LIB unit (see Figure 1(b)). The energy conservation equation is [155]

$$\rho C_p\frac{\partial T}{\partial t}=\nabla(k_T\nabla T)+Q_{rea}+Q_{ohm}+Q_{act} \tag{3.29}$$

where ρ, C_p and k_T are the material density, the heat capacity, and the thermal conductivity of the battery unit. The thermal conductivity in the cylindrical battery along the radial direction is different from that along the axial direction [142]. They are calculated using the following two equations, respectively.

$$k_{\mathrm{T},R}=\frac{\sum L_i}{\sum \frac{L_i}{k_{T,i}}} \tag{3.30}$$

$$k_{\mathrm{T,Z}}=\frac{\sum L_i k_{T,i}}{\sum L_i} \tag{3.31}$$

The corresponding boundary condition is

$$Q_0=h\cdot(\mathrm{T_{amb}}-\mathrm{T}) \tag{3.32}$$

where Q_0 is the heat flux on the battery surface and h is the lumped heat transfer coefficient. h is set as 15 W m^{-2} K^{-1} [159] in this study, which simulates the free air convective condition.

3.2.2.5 Numerical solution of the equations

The electrochemical-thermal coupled model is solved using the COMSOL Multiphysics 5.2 software, which is widely accepted by researchers for studies on LIB modeling [149, 154, 155]. Table 3.1 and Table 3.2 shows the model parameters and the material properties, respectively, used in this study. Typical battery separators are made of polymers such as polyethylene, polypropylene, and polyacrylonitrile [43]. This study sets the thermal conductivity, heat capacity and density of separator as 0.3 W m^{-1} K^{-1}, 1,700 J kg^{-1} K^{-1} and 900 kg m^{-3}, respectively, to represent typical values of polymer based separator [160, 161].

Table 3.1. Modeling parameters

Parameter	Unit	Cathode	Separator	Anode	Ref.
L_i	µm	55	20	39	[162]
r_i	µm	1.4	-	6.5	[162]

$\varepsilon_{s,i}$	-	0.513	-	0.585	[162]
$\varepsilon_{l,i}$	-	0.364	0.54	0.417	[162]
C_{s,i_max}	mol·m^{-3}	22,806	-	31,370	[162]
C_{s,i_ini}	mol·m^{-3}	1,140	-	26,665	[162]
C_{l,i_ini}	mol·m^{-3}	1,500	1,500	1,500	[153]
$\alpha_{a,i}$	-	0.5	-	0.5	[153]
$\alpha_{c,i}$	-	0.5	-	0.5	[153]
δ_i	S·m^{-1}	0.5	-	100	[162]
$brug,i$	-	1.8	1.5	2.4	[162]
t_+	-	0.363	0.363	0.363	[153]

Table 3.2. Thermal properties of LIB materials

Material	k_T (W m^{-1} K^{-1})	C_p (J kg^{-1} K^{-1})	ρ (kg m^{-3})	Ref.
Cathode	1.48	800	1,500	[153]
Separator	0.3	1,700	900	
Anode	1.04	641	2,223	[153]
Cathode CC*	237	897	2,700	[153]
Anode CC	398	396	8,700	[153]
Electrolyte	0.099	1,518	1,210	[153]
Battery canister	14	460	7,500	[153]
Mandrel	0.26	1,700	1,150	[155]

* Current collector

3.3 Results and discussion

3.3.1 Model validation

The model for the 38120 type $LiFePO_4$ LIB is first validated by comparing the model with the experimental data reported in literature [153]. The result in Figure 3.2 shows that the discharge voltage plateau and capacity decrease as the battery discharge rate increases from 0.3 to 2 C. This is because of the great internal battery resistance at a fast discharge rate [163]. On the other hand, there is a rapid temperature rise at high discharge rate because the battery cell operated at a higher discharge rate is exhausted quickly [151].

Overall, the model agrees with the experimental results [153] for LIB discharged at various rates, except for the working voltage at the beginning of discharge and the temperature rise for the discharge rate of 0.3C. As a result, the developed model is deemed valid for the electrochemical and thermal performances of the 38120 LIB discharged at 1C and 2C rates. The mean relative error for simulating working voltage and temperature rise of the LIB with discharged rates of 1C and 2C are 0.76% and 7.6%, respectively.

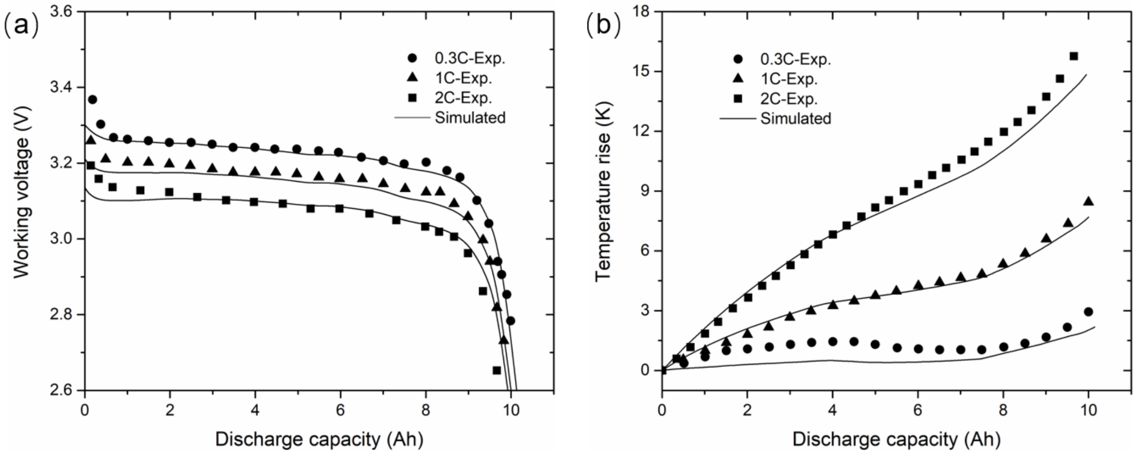

Figure 3.2. Comparison of model with experimental data at different discharge rates: (a) working voltage and (b) temperature rise

The validated model is then used to study the performances of the 38120 type $LiFePO_4$ LIB by changing the separator design parameters. The studied discharge rate is set at a high rate of 2C, due to the rising trend of developing high-rate LIB [164, 165]. The rest of this chapter presents the calculated battery energy density and electrolyte concentration distribution with different separator thickness (ranging 5-100 μm) and separator porosity (35%-95%), respectively. In addition, the temperature rises and temperature distribution within the battery packed material are also studied for separators with different thermal conductivities (0.3-3 $W\ m^{-1}\ K^{-1}$) and heat capacities (1700-3500 $J\ kg^{-1}\ K^{-1}$), respectively. The ranges of these parameters were chosen to cover typical values of battery separators [7, 43, 166].

3.3.2 Effects of separator on energy density

Figure 3.3 (a) presents the effects of separator thickness and porosity on the energy density of the LIB discharged at a rate of 2 C, where the effects of separator thickness is shown in the dashed line and the separator porosity is shown in the solid line. The battery energy density dropped from 148.8 to 110.6 Wh/kg when the separator thickness increased from 5 to 100 μm. However, the separator porosity has negligible impact on the battery energy density. Figures 3(b) and 3(c), on the right of Figure 3(a), show the discharge profiles of the batteries with different separator thickness and porosity. The working voltage of the discharge plateau decreased by about 0.02 V when the separator thickness increased from 5 to 100 μm, meanwhile, the discharge capacity decreased from 11.1 to 6.3 Ah. Unlike the separator thickness, separator porosity does not have a strong impact on the battery discharge profile: there was only slight decrease of the working voltage when the separator porosity changed from 35% to 95%.

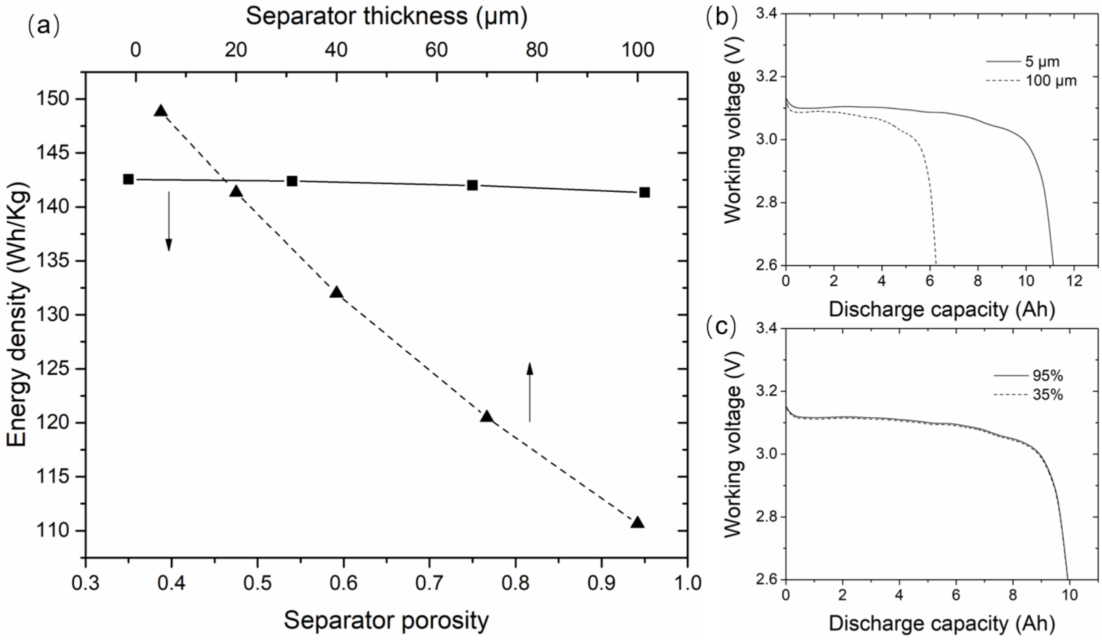

Figure 3.3. Effects of separator thickness and porosity on the energy density of the LIB (a) discharged at 2C rate, (b) with detailed discharge profiles for different separator thickness and (c) separator porosity

The rapid drop of energy density indicates the negative effects of the separator thickness on the battery energy density than that of the separator porosity. For a given battery canister, increasing the separator thickness reduces the packed volume of the electrode materials, which consequently reduced the battery discharge capacity (see Figure 3b). In addition, increasing separator thickness from 5 to 100 μm results in increased internal resistance of the battery.[43] As a result, the initial discharge voltage of using a 100 μm separator is about 0.02 V lower than that using a 5 μm separator.

Enhanced discharge rate capability is reported for coin cell LIBs with high-porosity separators [82, 90]. It means that increasing separator porosity would improve the battery energy density that discharged at a fast rate. However, this is not the case for the 38120 cylindrical batteries with high separator porosities, even at a discharge rate of 10 C.

This diminished advantage of 38120 LIB with a high-porosity separator is attributed to the heat generation in the 38120 cylindrical battery, which is much greater than that in a coin cell battery. The resultant temperature rise enhances the mass transfer and electrochemical reactions for 38120 LIBs with both high and low porosity separators (*see* Eqs. 3.5, 3.6 and 3.15). On the contrary, the low temperature rise of coin cells was reported by Wang *et al.* [167]: the temperature rise on the surface of a CR2032 coin cell was always below 0.05 °C during battery operation at various C rates. In addition, our results show that the energy density of 38120 LIB could be increased from 81.8 to 84.1 Wh/kg when the separator porosity increased from 35% to 95% for a discharge rate of 10 C if the temperature rise of battery is omitted. This finding further confirms that separator porosity has little impact on the energy density of 38120 type LIBs.

3.3.3 Effects of separator on electrolyte concentration distribution

Figure 3.4 shows the electrolyte concentration distribution across the calculated battery domain with different separator thicknesses and porosities. The contents in the brackets in the legends are the electrolyte concentration gradients. Both graphs show that the electrolyte concentrations decrease from anode to cathode at the end of discharge, creating concentration gradients across battery cell. Figure 3.4 (a) shows that the differences between electrolyte concentration gradients within the separator domain are negligible when the separator thickness increases from 5 to 100 μm. On the contrary, Figure 4(b) shows that the concentration gradient in the separator domain decreases from 15.7×10^5 to 3.5×10^5 $\mathrm{mol{\cdot}m^{-4}}$ as the separator porosity increases from 35% to 95%.

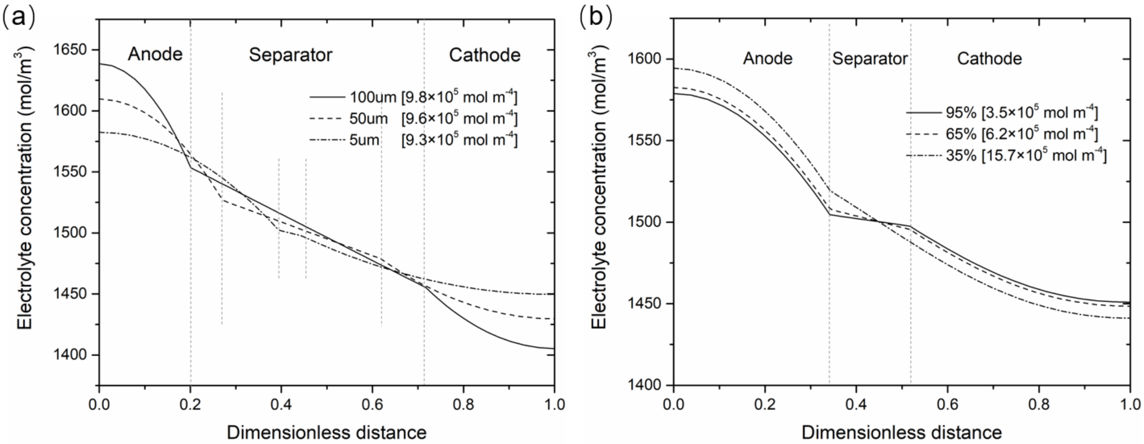

Figure 3.4. Electrolyte concentration distribution of LIB with different (a) separator thicknesses and (b) porosities at the end of 2C rate discharge

During the battery discharge, the lithium ions are first extracted from the anode electrode particles followed by intercalation into the cathode electrode. As shown in Figure 3.4, the electrolyte concentration gradient across the battery cell is caused by the mass transfer resistance within the battery component. The increasing electrolyte concentration gradient within the separator phase indicates a higher resistance to mass transfer per unit distance. Thus, the results from Figure 3.4 (b) indicate that increasing separator porosity can effectively reduce the mass transfer resistance per unit separator thickness. This result can also be explained by Eq. (3.13): increasing the separator porosity can directly increase the effective diffusion coefficient, enhancing the mass transfer. Increasing separator thickness increases overall battery resistance although the separator thickness shows a negligible effect on the electrolyte concentration gradient; this is also supported by the overall concentration drop from anode to cathode (*see* Figure 3.4 a).

Realizing the importance of separator porosity, this study further quantifies the correlation between the separator porosity and the electrolyte concentration gradient. The correlation shows that their relationship can be described using the exponential function in Eq. 3.33 with R^2=0.9996 (*see* Figure 3.5). This result suggests that the mass transfer resistance remains relatively stable for the separator porosity of 80% or greater. Therefore, the porosity of 80% can be considered as a design value for separators.

$$Cg_l = 2.7\times10^5 + 1.3\times10^6 \exp\left(-\left(\varepsilon_{l,s} - 0.346\right)/0.23\right),\ (0.35 \le \varepsilon_{l,s} \le 0.95) \qquad (3.33)$$

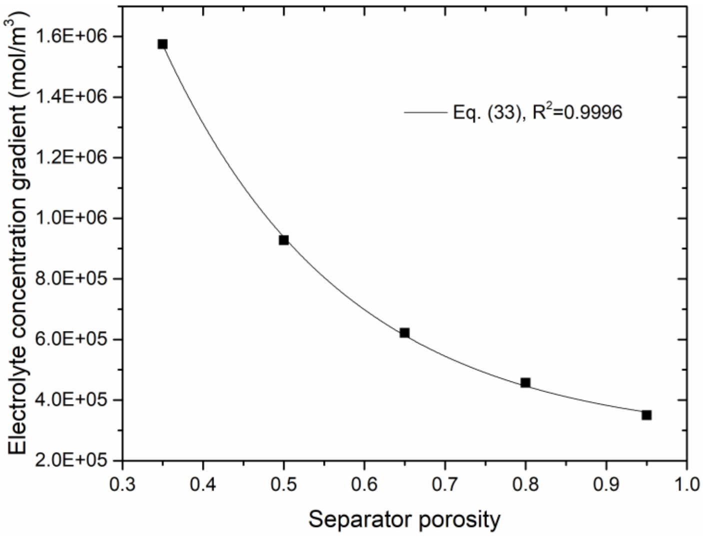

Figure 3.5. Curve fitting of correlation between separator porosity and electrolyte concentration gradient

In addition, Figure 3.6 presents the temporal changes of electrolyte concentrations at the separator boundaries for separator porosities of 35% and 95%. For both porosities, the electrolyte concentrations at boundary 2 increase while those at boundary 3 decrease at the beginning of battery discharge. For both separator porosities, the electrolyte concentration reached their changing point in about 80 s. As we have explained in the above paragraphs, the mass transfer rate positively correlates to the separator porosity. Therefore, the changes in electrolyte concentrations on the separator boundaries are higher for the separator with 35% porosity than that with 95% porosity. After reaching their peak or bottom values, the electrolyte concentrations remained relatively steady for the separator with 95% porosity during the discharge period. On the contrary, the electrolyte concentrations for the separator with 35 % porosity slowly decreased at boundary 2, but increased at boundary 3. When the current is cutoff at the end of discharge, the electrolyte concentrations quickly returned back to its original value within milliseconds.

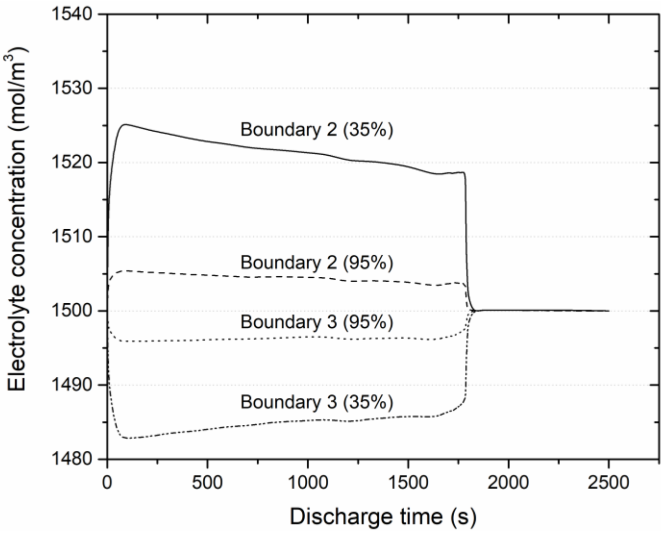

Figure 3.6. Temporal changes of electrolyte concentrations in the LIBs having different separator porosities with the 2C discharge rate

The preceding results in Figure 3.6 can be explained as follows. During discharge, as shown in Figure 3.2, the battery temperature quickly rises over time, which in turn enhances the electrolyte mass transfer (see Eq. 3.15). Therefore, the concentration at Boundaries 2 and 3 decreased and increased, respectively, weakening the concentration gradient during the discharge time. This enhancement in mass transfer due to temperature rise, however, is negligible for the separator with a 95% porosity. This is because of the low mass transfer resistance already achieved by high porosity as stated above.

3.3.4 Effects of separator on battery thermal performances

The heat generated in a LIB cell can be reversible heat or irreversible heat. As presented in

Section 3.2.2.4, the reaction heat (Q_{rea}) is reversible and the active polarization heat (Q_{act}) and ohmic heat (Q_{ohm}) are irreversible. Only ohmic heat is generated in the separator because of the transport of lithium ions [145]. Thus, the heat generation rate inside separator phase is calculated by Eq. (3.27) in this study.

Figure 3.7 (a) shows the calculated effects of the porosity and thickness of a separator on the heat generation rate within the separator. Increasing separator porosity from 35% to 95% reduces the heat generation rate from 7,475 to 1,670 W/m^3. On the other hand, the separator thickness has negligible effect on the heat generation rate. As discussed in Section 3.3.3, the electrolyte concentration gradient decreases as the separator porosity increases. Then, the reduced concentration gradient, as indicated by the term $\partial \ln c_i / \partial x$ in Eq. (3.27), results in lowering heat generation rate within the separator. However, the impact of separator thickness on the heat generation rate is not obvious because the separator thickness has little effect on the electrolyte concentration gradient (*see* Figure 3.4).

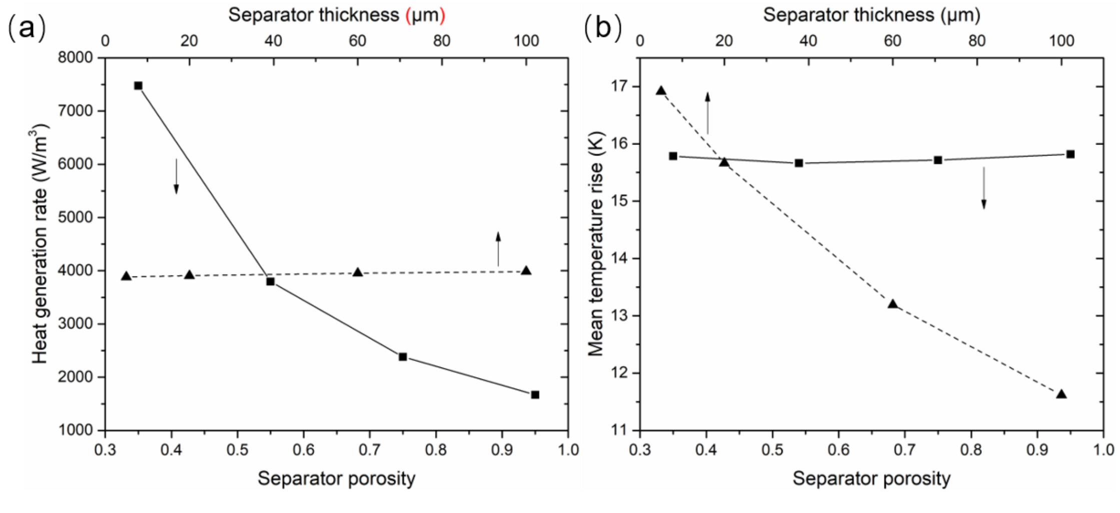

Figure 3.7. Effects of separator porosity and thickness on (a) the heat generation rate in the separator phase and (b) the temperature rise of packed material in the battery cell

Figure 3.7 (b) compares the effects of separator porosity and thickness on the mean temperature rise in the materials packed inside the LIB. The temperature rise drops from 16.9 to 11.6 K when the separator thickness increases from 5 to 100 μm, but the separator porosity has a little impact on the battery temperature. The battery temperature rise decreases with separator thickness because less active electrode materials were packed in the battery canister when the separator becomes thicker. The heat in a battery is primarily generated by battery cathode and anode [145], which dominates the temperature rise of LIB operation. This also explains the negligible effects of the separator porosity on the temperature rise of the battery.

The excessive heat accumulation and uneven temperature distribution in a LIB may degrade the LIB [162]. As shown in Table 3.2, the heat conductivities of the separator and the electrolyte are much less than those of other LIB components. As a result, the thermal resistance of a 20 μm separator contributes to about 70% of the total resistance in the battery along the radial direction.

Figure 3.8 shows the effects of separator thermal conductivity and heat capacity on the temperature rises and differences of the packed materials in LIBs. The temperature rise quickly drops by 0.4 K when the separator conductivity increases from 0.3 to 1.0 W m^{-1} K^{-1}. Further increase in the conductivity did not significantly reduce the temperature rise. The temperature difference shows a similar trend: the temperature difference decreased by 0.63 K when the thermal conductivity increased from 0.3 to 1.0 W m^{-1} K^{-1}. However, the separator heat capacity, does not have an obvious impact on the temperature differences. The temperature rise linearly decreased from 16.4 to 15.5 K while the separator heat capacity increasing from 1,700 to 3,500 J kg^{-1} K^{-1}. Yang *et al.* [166] reported similar effects of separator thermal conductivity using a different model (which is carried out by inputting assumed joule heating power values as heat source, whereas the heat source in this study is calculated by electrochemical modeling). A separator thermal conductivity of 1.0 W m^{-1} K^{-}

^{1} was reported to be effective in reducing the temperature rise for both cylindrical and prismatic batteries. As a result, a thermal conductivity of 1 W m^{-1} K^{-1} can be considered as a design value for LIB separators.

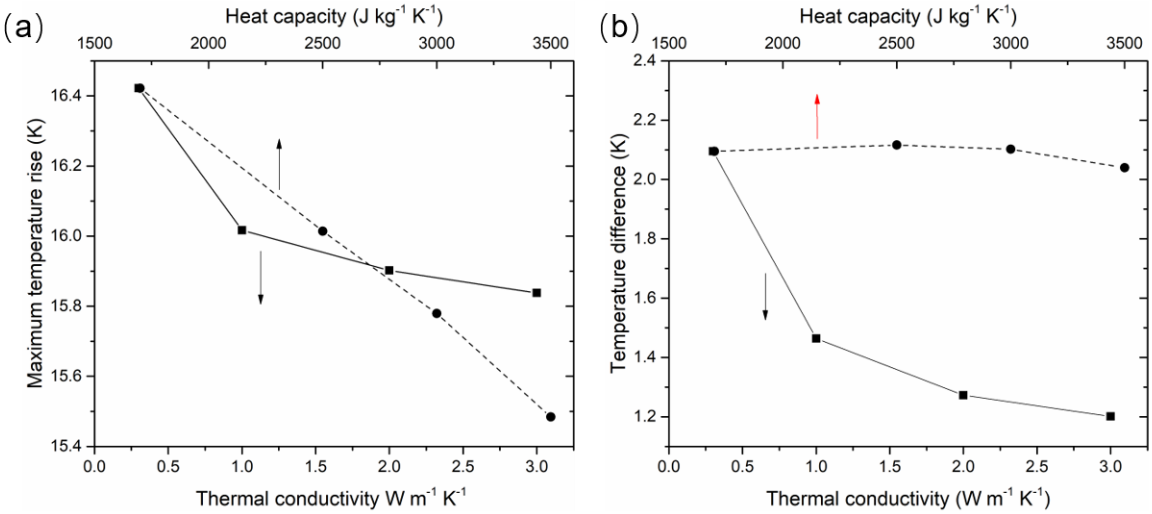

Figure 3.8. Effects of separator thermal conductivity and heat capacity on (a) the temperature rise and (b) temperature difference of the materials packed in the battery discharged at 2C rate

In summary, the analyses in this section show that thermal performance of a LIB battery can be improved by increasing both separator thermal conductivity and its heat capacity. Though, the elevated temperature facilitates the mass transfer of a single battery cell (as discussed in Sections 3.3.2 and 3.3.3), the accumulated heat still causes safety issues when using it for big battery packs. Thus, improving the thermal performances of a single battery cell can help with the longevity. It also helps maintain stable electrochemical performances by minimizing undesired side reactions and thermal stress of LIB at low temperature rise and uniform temperature distribution condition [166, 168]. For the ease of presentation, Figure 8 illustrates the temperature profile of a LIB unit discharged at a 2C rate. It shows that simultaneous increase in the separator thermal conductivity to 1 W m^{-1} K^{-1} and its heat capacity to 3500 J kg^{-1} K^{-1} reduces not only the maximum temperature rise of the battery material by 1.3 K, but also the temperature difference by 0.8K.

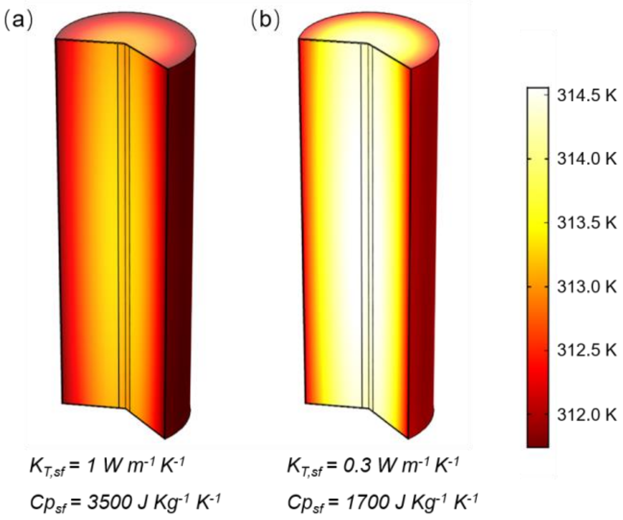

Figure 8. The LIB temperature profile at the end of discharge with a rate of 2 C

3.4 Summary

This Chapter studies the impact of the thickness, porosity, thermal conductivity, and heat capacity of a battery separator on the electrochemical and thermal performances of a commercial 38120 $LiFePO_4$ LIB by numerical modeling. The 2D axisymmetric electrochemical-thermal coupled model for LIB is developed and validated with experimental data in the literature before it is used to simulate the battery operation at different conditions. The following conclusions can be drawn from the works presented herein.

First, the separator thickness shows strong effects on the battery energy density. The battery energy density drops from 148.8 to 110.6 Wh/kg when the separator thickness increases from 5 to 100 μm. The reason is that a thicker separator takes more space in the battery canister allowing for less packed electrodes materials.

Second, the mass transfer resistance increases with decreasing separator porosity, resulting in increased electrolyte concentration gradient inside the battery separator. The correlation between the separator porosity and the electrolyte concentration gradient can be described by an exponential function. This function indicates that LIB separators should have an optimum porosity of 80% and that further increase in the separator porosity contributes little to the mass transfer.

Finally, it is necessary to improve the thermal properties of the separator because of its great heat transfer resistance. Simultaneous increase in thermal conductivity to 1 W m^{-1} K^{-1} and heat capacity to 3500 J kg^{-1} K^{-1}, respectively, helps reduce the battery temperature rise by 1.3 K and temperature differences by 0.8 K.

Chapter 4

Kinetics of Preparing Polypyrrole-based Membrane by *In-situ* Polymerization on Electrospun Nanofibers

From Chapter 3, an important conclusion is that the use of a thin separator with high porosity of 80% in a LIB cell can achieve enhanced battery energy density with low internal mass transfer resistance. The high porosity of a separator can be achieved by developing electrospun nanofibrous separator, due to the electrospun membrane can attain porosity as high as above 70% [43]. However, the thickness of a separator in actual battery applications cannot be reduced to extremely thin. Because, there is a trade-off between a separator's thickness and its mechanical strength. A separator has to be sufficiently strong to fulfill the mechanical requirements of the battery assembling process, and maintain its integrity during battery operations.

An alternative strategy is to use redox-active separator to provide additional capacity to the battery cell. Therefore, the redox-active separators with sufficient thickness can be used in LIB cells without compromising the energy density. A bilayer structured redox-active separator is proposed in this thesis based on integrating PPy with electrospun nanofibers. On the other hand, *in-situ* polymerization is considered as a feasible method to fabricate the PPy composite nanofibers as discussed in Chapter 2.2. Thus, this Chapter presents a detailed kinetics study of the PPy in-situ polymerization on electrospun nanofibers, aiming to better understand the mechanisms behind the fabrication process.

4.1 Introduction

Polypyrrole (PPy) is a typical type of conductive polymer with redox-activity, chemical stability, and ease of synthesis [126]. PPy can be produced by the polymerization of pyrrole (Py) with chemical oxidants or electropolymerization of pyrrole solution. Either method is suitable for sample preparation in a laboratory setting. However, pristine PPy is an insoluble and brittle solid in the forms of particles or dense film, which limits its direct applications in many fields where a porous flexible material is required (*e.g.* battery separator) [133].

A feasible approach to fabricating PPy into various structures is *in-situ* polymerization of PPy onto different templates. For instance, Cu-TCPP nanosheets [131], textile fibers [132], and polyurethane foams [133] have been reported to implement as templates for *in-situ* polymerization process to fabricate PPy composites with different structures.

Electrospun nanofibers have also been reported as a template for *in-situ* polymerization of PPy. The resultant composite maintains the structural features, including inter-connected porous structure, superior porosity, and submicron pore size, of electrospun fibers for applications to filtration, energy storage, and tissue engineering. For example, Luo *et al.* [169] used electrospun polyacrylonitrile (PAN) membrane as a template for pyrrole *in-situ* polymerization. The fabricated composite membranes exhibited more than 8 times of Pb(II) adsorption compared to pristine PAN membrane for water treatment. Lu *et al.* [170] also implemented the pyrrole *in-situ* polymerization on electrospun poly(acrylic acid) (PAA)/MnO_2 membranes. The PPy based fibrous membrane was used as an efficient electrode for supercapacitors with a gravimetric specific capacity of 564 F g^{-1}. Thunberg *et al.* [136] also fabricated PPy/cellulose composite membrane by *in-situ* polymerization of pyrrole on electrospun cellulose template. SHSY5Y human neuroblastoma cells were incubated onto the membrane to test the feasibility of the fabricated membrane as scaffold for neural tissue. After 15 days of cell differentiation, the PPy-based membrane was altered to a neuron like phenotype. However, these earlier research works are focused on the electrochemical properties of the PPy added nanofibrous membrane and they are tested for specific applications. The kinetics of *in-situ* polymerization of pyrrole in the presence of nanostructural template is rarely studied.

Only a few studies reported the observations of an increase in the reaction rate of polymerization with template. Percec *et al.* [171] reported the *in-situ* polymerization of PPy on nano graphene oxide platelets. The pyrrole consumption rate increased when graphene oxide platelets were added as *in-situ* polymerization templates. In addition, Chatterjee *et al.* [132] compared the *in-situ* polymerization of PPy onto various textile fibers and showed that the PPy generation rate and final yield increased by 2.4-65.8% and 0.4-14.5%, respectively, with textile fibers added into the polymerization solution. Despite these earlier studies, the mechanisms behind the increase in reaction rate remain unclear [172, 173].

Therefore, the objective of this work is to study the kinetics of the *in-situ* polymerization of PPy with electrospun fibrous membrane as template, aiming to better understand the mechanism of pyrrole *in-situ* polymerization. Accordingly, the rest of this chapter is organized as follows. Section 4.2 introduces two different kinetics models developed based on existing PPy polymerization mechanisms to calculate the concentrations of pyrrole monomer at different reaction times. Then, Section 4.3 introduces the procedure and methods of pyrrole *in-situ* polymerization. Polyacrylonitrile (PAN) nanofibers are produced by a laboratory-made electrospinning device, followed by *in-situ* polymerization of pyrrole onto the fiber surface to form membranes. The *in-situ* polymerization treatment is carried out in aqueous solutions at different temperatures using ammonium persulfate (APS) as oxidant. The most suitable mechanism for pyrrole polymerization is identified in Section 4.4.1 and adopted for the rest of study by fitting the model against experimental data. Based on the knowledge obtained in Section 4.4.1, Section 4.4.2 presents an in-depth kinetics study on the *in-situ* polymerization of pyrrole, followed by the investigation of the activation enthalpy and entropy in Section 4.4.3. Then, Section 4.4.4 describes the effects of doping on *in-situ* polymerization. Dopant is commonly used for PPy synthesis in practical applications to improve its conductivity. Thus, the effect of dopant on the *in-situ* polymerization process is of interest.

4.2 Kinetics models of pyrrole polymerization

There are two pyrrole polymerization mechanisms reported in the literature. The more widely suggested mechanism (denoted as Mechanism I in this study) is based on the coupling between radical cations [174]. As shown in Figure 4.1, the pyrrole monomer is first oxidized to produce radial cation. Then, two radical cations are coupled and deprotonated to produce a bipyrrole, which is oxidized to react with another radical cation. Repeating the preceding steps results in the chain propagation and large molecular PPy. The polymerization reaction based on this mechanism is first order with respect to pyrrole and oxidant [175]. Thus, the rate equation for pyrrole can be written as:

$$-\frac{d\left[\mathrm{Py}\right]}{dt}=k\left[\mathrm{S_2O_8}^{2-}\right]\left[\mathrm{Py}\right] \tag{4.1}$$

where k is the reaction rate constant ($\mathrm{L \cdot mol^{-1} \cdot min^{-1}}$); [$S_2O_8^{2-}$] and [Py] are the concentrations ($\mathrm{mol \cdot L^{-1}}$) of the APS (the oxidant used in this study) and pyrrole, respectively.

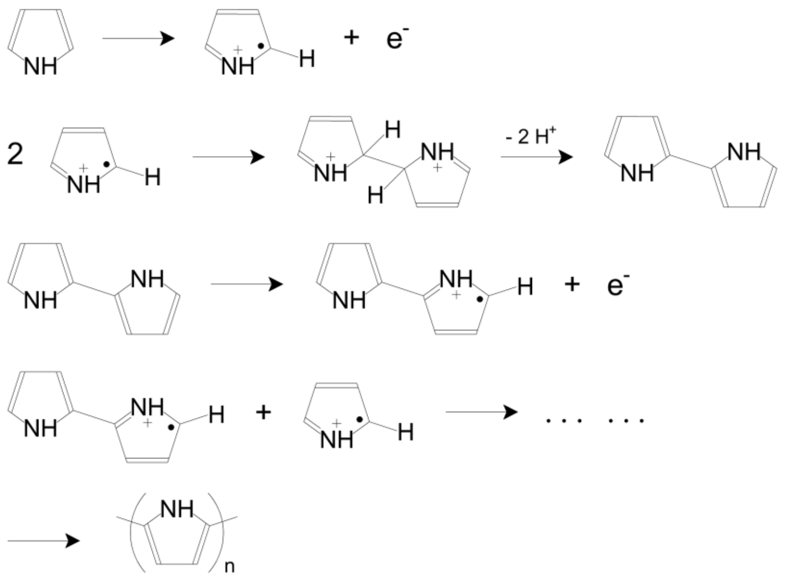

Figure 4.1. Mechanism I of pyrrole polymerization

According to the reaction stoichiometry of pyrrole reaction with APS [176], 1.25 mol of APS ($S_2O_8^{2-}$) is consumed for unit mole of pyrrole polymerized. Thus, the concentration of APS can be calculated as:

$$\left[\mathrm{S_2O_8}^{2-}\right] = \left[\mathrm{S_2O_8}^{2-}\right]_0 - 1.25\left([\mathrm{Py}]_0 - [\mathrm{Py}]\right) \tag{4.2}$$

where $[S_2O_8^{2-}]_0$ and $[Py]_0$ are the initial concentrations (mol·L^{-1}) of APS and pyrrole, respectively.

Then, Eq. 4.3 is obtained by substituting Eq. 4.2 into Eq. 4.1:

$$-\frac{d[\mathrm{Py}]}{dt} = k\alpha[\mathrm{Py}] + 1.25k[\mathrm{Py}]^2 \tag{4.3}$$

where,

$$\alpha = \left[\mathrm{S_2O_8}^{2-}\right]_0 - 1.25[\mathrm{Py}]_0 \tag{4.4}$$

The solution to Eq. 4.3 is described using Eq. 4.5:

$$[\mathrm{Py}] = -\frac{k\alpha \exp\left(k\alpha C_1\right)}{-\exp(k\alpha t) + 1.25k \exp\left(k\alpha C_1\right)} \tag{4.5}$$

where C_1 is a constant derived and it must satisfy Eq. (4.6) to ensure [Py] = $[\mathrm{Py}]_0$ at $t = 0$:

$$C_1 = \frac{\ln\left[[\mathrm{Py}]_0 \big/ \left(1.25 \cdot k \cdot [Py]_0 + \alpha k\right)\right]}{\alpha k} \tag{4.6}$$

Another mechanism of pyrrole polymerization (denoted as Mechanism II) is as follows [172]. As shown in Figure 4.2, the pyrrole monomer is first oxidized into radial cation. Then, the radical cation reacts with a neutral pyrrole monomer to produce bipyrrole. The bipyrrole is immediately oxidized to form another type of radical cation, which reacts with another neutral monomer to generate tripyrrole. Repeating this process results in the formation of large molecular PPy. The pyrrole reaction rate is described using Eq. 4.7.

$$-\frac{d[\mathrm{Py}]}{dt} = k_1\left[\mathrm{S_2O_8}^{2-}\right][\mathrm{Py}] + k_2[\mathrm{P}][\mathrm{Py}] \tag{4.7}$$

where k_1 and k_2 are the reaction rate constants ($\mathrm{L \cdot mol^{-1} \cdot min^{-1}}$); $[\mathrm{S_2O_8}^{2-}]$, [Py], and [P] denote the concentrations ($\mathrm{mol \cdot L^{-1}}$) of APS, pyrrole, and oxidized oligomer (molecules consists a few repeating units derived from pyrrole polymerization, *e.g.*, bipyrrole, tripyrrole, *etc.*), respectively.

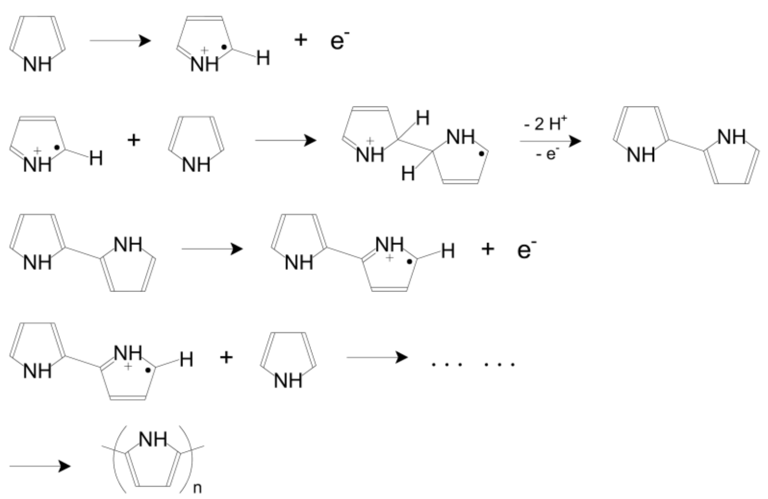

Figure 4.2. Mechanism II of pyrrole polymerization

The oxidation of a pyrrole oligomer or PPy polymer is so fast [172] that the concentration of the oxidized oligomer is considered the same as that of the oligomer generated:

$$[\mathrm{P}]=[\mathrm{Py}]_0-[\mathrm{Py}] \tag{4.8}$$

Substituting Eqs. 4.2 and 4.8 into Eq. 4.7 results in Eq. 9:

$$-\frac{d[\mathrm{Py}]}{dt}=\beta_2[\mathrm{Py}]+\beta_1[\mathrm{Py}]^2 \tag{4.9}$$

where β_1 and β_2 are coefficients:

$$\beta_1=1.25k_1-k_2 \tag{4.10}$$

$$\beta_2=k_1\left[\mathrm{S_2O_8}^{2-}\right]_0-\beta_1[\mathrm{Py}]_0 \tag{4.11}$$

Solving Eq. 4.9 gives the concentration of pyrrole:

$$[Py]=-\frac{\beta_2\exp(\beta_2C_2)}{-\exp(\beta_2t)+\beta_1\exp(\beta_2C_2)} \tag{4.12}$$

where C_2 is a constant and it must satisfy Eq. 4.13 to ensure the initial condition of [Py] = $[\mathrm{Py}]_0$ at $t = 0$.

$$C_2 = \frac{\ln\left[[\mathrm{Py}]_0 \big/ \left(\beta_1 \cdot [\mathrm{Py}]_0 + \beta_2\right)\right]}{\beta_2} \tag{4.13}$$

Equations 4.5 and 4.12 are used in this study to fit the experimental data of pyrrole polymerization. Accordingly, the reaction rate constants k, k_1, and k_2 are obtained from the fitting results.

In addition, parameter λ is defined (*see* Eq. 4.14) to quantify the excessive amount of oxidants used in pyrrole polymerization.

$$\lambda = \frac{[\mathrm{oxidant}]_0}{s \cdot [\mathrm{Py}]_0} \tag{4.14}$$

where s is the stoichiometric coefficient of the oxidant per unit number of pyrrole. In this study, s is 1.25 for the APS oxidant [176]. Eq. 4.14 shows that λ greater than 1 indicates excessive oxidant used for pyrrole polymerization and that λ less than 1 indicates inadequate oxidant.

Moreover, the Eyring equation [177] is used to describe the change of reaction rate constant with temperature:

$$\ln\frac{k_i}{T} = \frac{-\Delta H^{\ddagger}}{R} \cdot \frac{1}{T} + \ln\frac{k_B}{h} + \frac{\Delta S^{\ddagger}}{R} \tag{4.15}$$

where T is the reaction temperature (K), R is the gas constant 8.314 $\mathrm{J \cdot K^{-1} \cdot mol^{-1}}$; k_B denotes to the Boltzmann constant, 1.38×10^{-23} $\mathrm{J \cdot K^{-1}}$; h is the Planck's constant, 1.05×10^{-34} J·s; $\Delta H^{\ddagger}$ and $\Delta S^{\ddagger}$ are the activation enthalpy (J) and activation entropy ($\mathrm{J \cdot K^{-1}}$), respectively.

Eq. 4.15 shows a linear relationship between $\ln(k_\mathrm{i}/T)$ and $1/T$. Thus, the activation enthalpy and entropy can be calculated from the slope and intercept of the $\ln(k_\mathrm{i}/T)$ *vs.* $1/T$ plot, respectively.

4.3 Experiment

4.3.1 Materials

Polyacrylonitrile (PAN, M_W=150000), pyrrole (Py, purity>98%), ammonium persulfate (APS, purity>98%), sodium ferrocyanide ($Na_4Fe(CN)_6$, purity>98%) N,N-dimethylformamide (DMF, purity>99.8%) are purchased form Sigma Aldrich (Canada). Pyrrole is sealed and stored in a refrigerator after each use.

4.3.2 Electrospinning device

As shown in Figure 4.3, the electrospinning device used in this study is custom designed and assembled. The main components of this device include a syringe pump (Fusion 200, chemyx, USA), a laboratory-made high voltage power supply, a metallic needle loaded on a needle holder, and a grounded drum collector with controller (TongLi Tech, China). The aluminum frames and structure of the device is obtained from 80/20 LLC, USA, to custom build the enclosure.

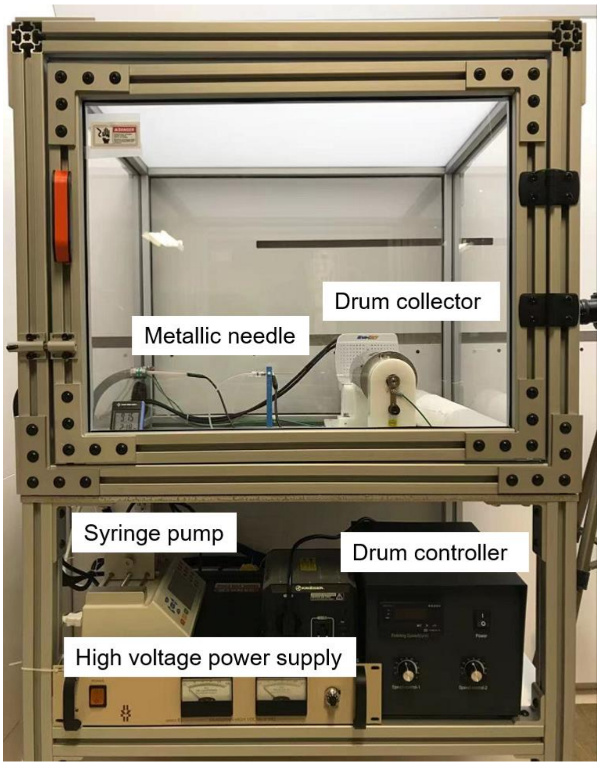

Figure 4.3. Laboratory-made electrospinning device

4.3.3 Fabrication of PAN nanofibers

The laboratory-made electrospinning device is used to produce PAN nanofibers following this procedure. First, PAN is dissolved in N,N-Dimethylformamide (DMF) to prepare a PAN solution with a concentration of 10 wt.%. The PAN solution is then loaded into a 5 mL syringe connected to a metallic needle with an inner diameter of 0.514 mm. The syringe pump is used to pump the solution at a steady flow rate of 0.4 ml/hr. The laboratory-made positive high voltage supply is connected to the metallic needle. The grounded drum collector (at a rotating speed of 30 rpm) covered with non-stick aluminum foil (Reynolds wrap, USA) is placed 11 cm away from the needle tip and used as a fiber collector. Continuous fiber jets are generated from the needle tip when the voltage is 7.5 kV. The nanofibers are deposited on the collector to form a fibrous membrane. Finally, the membranes are peeled off from the aluminum foil and cut into 4 cm×4 cm squares for further use.

4.3.3 Pyrrole *In-situ* polymerization

The procedure of pyrrole in-situ polymerization onto electrospun PAN template is carried out as follows. First, pyrrole is added into 15 ml of deionized water (0.008 mol/L) and cooled to a low temperature ranging from 273K to 288K in a cooler. Then, PAN electrospun membrane is immersed into the pyrrole solution as a template. Different weights of APS are dissolved into 2 ml of deionized water and cooled down to the same temperature of the pyrrole solution. Finally, the APS solution is added to the pyrrole solution dropwise to start the *in-situ* polymerization. The concentration of APS in the reaction bath is 0.04 mol/L or 0.012 mol/L. After a predetermined reaction time (*e.g.*, 15 or 30 min), the immersed membrane is immediately taken out from the solution using a tweezer and rinsed thoroughly using deionized water. Meanwhile, the reaction solution is vacuum filtered by a Büchner funnel connected to a vacuum pump. The precipitate and the treated membrane are then dried under vacuum at 80 °C in a vacuum oven for at least 12 hours (Vacuumoven-001, LeDAB, Canada).

Figure 4.4 shows the overall reaction equation for the pyrrole polymerization in an aqueous environment using APS as an oxidant [176]. The generated sulfate doped PPy is insoluble, thus it precipitates in the reaction bath and deposited onto the fiber surface. The amount of pyrrole consumed for each test is calculated using a gravimetric method [178, 179] (*see* Eq. 4.16).

$$[\mathrm{Py}]_c = 4\times\frac{W_p + \left(W_{m,a} - W_{m,b}\right)}{M_{PPy}\times V} \tag{4.16}$$

where $[\mathrm{Py}]_c$ (mol/L) is the amount of pyrrole consumed; W_p (g) is the weight of the precipitates; $W_{m,a}$ and $W_{m,b}$ (g) are the weights of the electrospun membrane after and before the *in-situ* polymerization reaction, respectively; M_{PPy} (g/mol) is the molecular weight of the repeating unit of sulfate doped PPy; V (L) is the volume of the reaction bath.

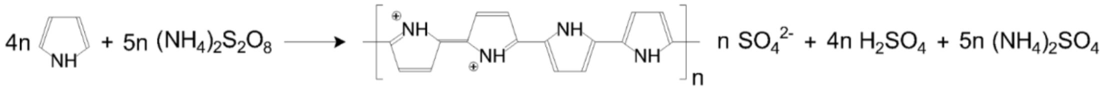

Figure 4.4. The polymerization of pyrrole with APS

The pyrrole concentration in liquid at the end of each test is calculated using Eq. 4.17:

$$[\mathrm{Py}] = [\mathrm{Py}]_0 - [\mathrm{Py}]_c \tag{4.17}$$

In addition, sodium ferrocyanide ($Na_4Fe(CN)_6$) is used as a dopant to study its effect on the *in-situ* polymerization of pyrrole. PPy polymers are commonly synthesized with the addition of dopant to improve its conductivity because the doping increases the amount of delocalized electrons in the PPy molecular chains. In this study, $Na_4Fe(CN)_6$ is adopted as a dopant for PPy synthesis because the final product exhibits great electrochemical properties, which has been reported as a potential material for energy storage [180]. Thus, in Section 4.4.4, 0.032 mol of $Na_4Fe(CN)_6$ is added to the pyrrole solution prior to the addition of oxidant.

4.4 Results and discussion

4.4.1 Comparison of pyrrole polymerization mechanisms

Figure 4 shows the depletion of pyrrole over reaction time at 277K without adding the electrospun membrane as fibrous template and the theoretical fittings using Mechanisms I and II. Both mechanisms well fit, with R^2>0.98, with the experimental data obtained with excessive APS for pyrrole polymerization (*i.e.*, λ=1.2). However, only Mechanism II (R^2=0.989) fits with the experiment when APS concentration is inadequate (*i.e.*, λ=0.4), whereas the fitting result of Mechanism I deviates from the experimental data with a R^2 =

0.653.

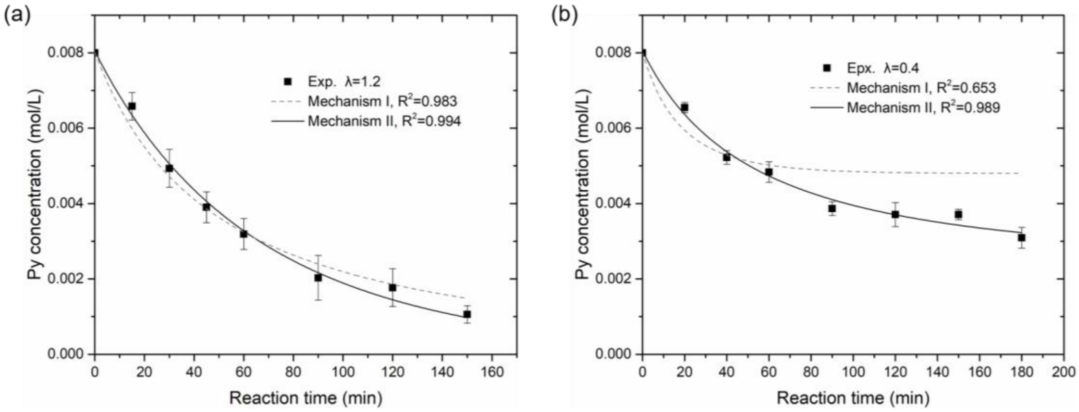

Figure 4.5. Theoretical fittings of pyrrole polymerization using different concentrations of APS at 277K.

In addition, both mechanisms are fitted with the experimental data in the literature [171, 172, 181] (*see* Figure 4.6). The results are the same as our findings, which confirms that Mechanism II fits well to experiments, regardless of excess or inadequate oxidant used for pyrrole polymerization. On the contrary, Mechanism I fits poorly with the experimental data when the oxidant concentration is inadequate. When $\lambda \leq 0.12$, the calculated results using Mechanism I implies that the polymerization rate should quickly drop to zero soon after the experiment started, which is inconsistent with the experimental results.

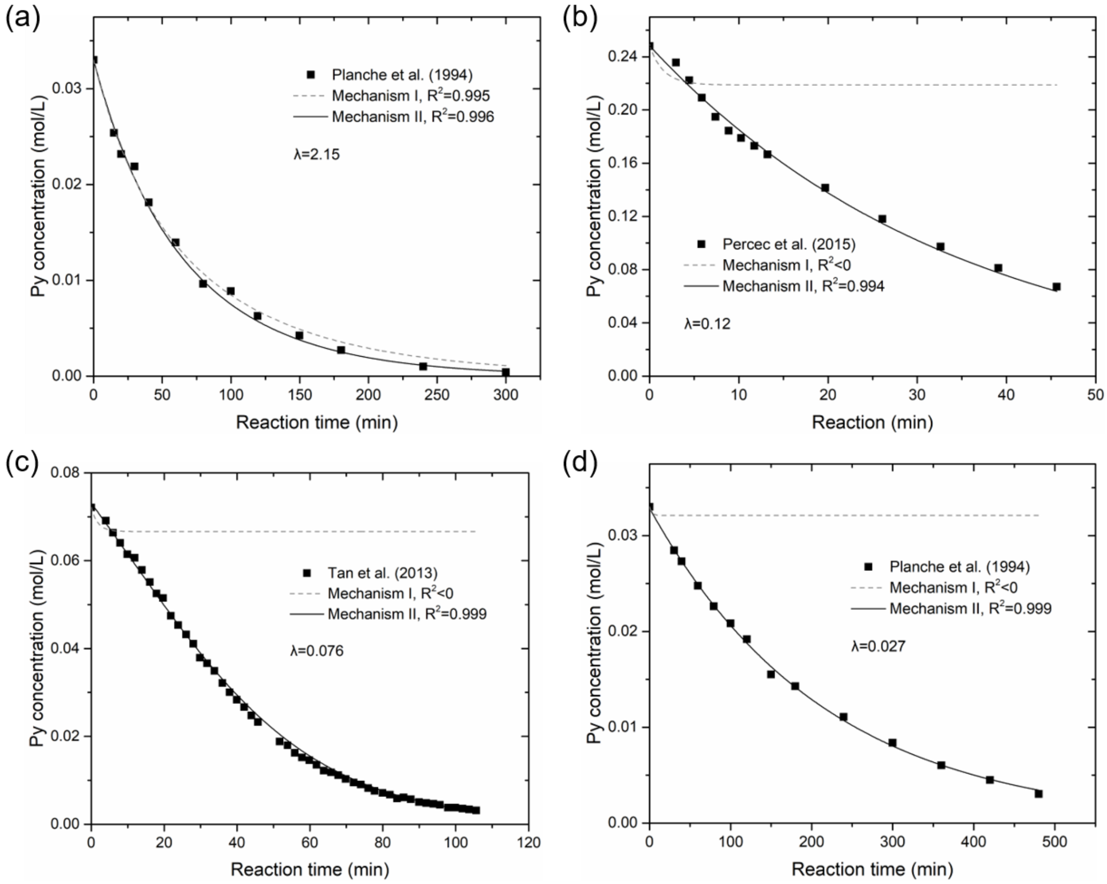

Figure 4.6. Theoretical fittings of Mechanisms I and II with the experimental data obtained from the literature (a) [181], (b) [171], (c) [172] and (d) [181]

The preceding results indicate that Mechanism II has a wider applicability than Mechanism I. In Mechanism I, the unreacted pyrrole monomers and oligomers must be oxidized by the oxidant prior to the chain propagation step. Thus, an adequate amount of oxidant is considered essential in this mechanism; otherwise, the polymerization reaction rate should be extremely slow when the oxidant concentration is low. However, in actual pyrrole polymerization experiments, the pyrrole concentrations at the late stage are obviously lower than the calculated results using Mechanism I (*see* Figure 4.5 b, Figure 4.6 b, c, and d). This indicates that the polymerization reaction rates are still relatively fast for low oxidant concentrations. On the other hand, Mechanism II proposes that the oxidized oligomer can directly react with a neutral pyrrole monomer for chain growth. The amount of oxidant involved in the polymerization process is less required in Mechanism II than in the Mechanism I. Thus, Mechanism II can be well fitted with the experimental data when oxidant is inadequate for pyrrole polymerization (See Figure 4.5 and Figure 4.6). Therefore, Mechanism II is deemed the most suitable mechanism for pyrrole polymerization. Thus, it is adopted in this chapter to study the *in-situ* polymerization of pyrrole.

It is worth noting that different experimental methods (*i.e.*, gravimetric method, high-performance liquid chromatography method, and nuclear magnetic resonance spectroscopy method) are used in different studies. The experimental data in Figure 4.5 seems to fluctuate more than those reported in the literature [171, 172, 181] (*see* Figure 4.6). However, the results in the literature did not provide error bars. If we assume that the reported data has acceptable repeatability, then we can conclude that all the experimental data fit with Mechanism II regardless of experimental methods. The gravimetric method used in this study is featured by low cost and simple operation. Thus, it is a suitable method for conducting the study in this chapter or other similar research.

4.4.2 Kinetics of pyrrole *in-situ* polymerization

Figure 4.7 shows the pyrrole depletion over time with and without the electrospun fibrous membrane as *in-situ* polymerization template. The pyrrole concentration in the liquid phase decreases with increasing reaction time, and it decreases more rapidly as the reaction temperature increases from 273 K to 285 K. The decreasing rates of pyrrole concentration are notably faster once the electrospun fibrous membranes are added into the reaction bath as a template for *in-situ* polymerization. In addition, the theoretical fittings of Mechanism II agree with the experimental data with R^2 greater than 0.99.

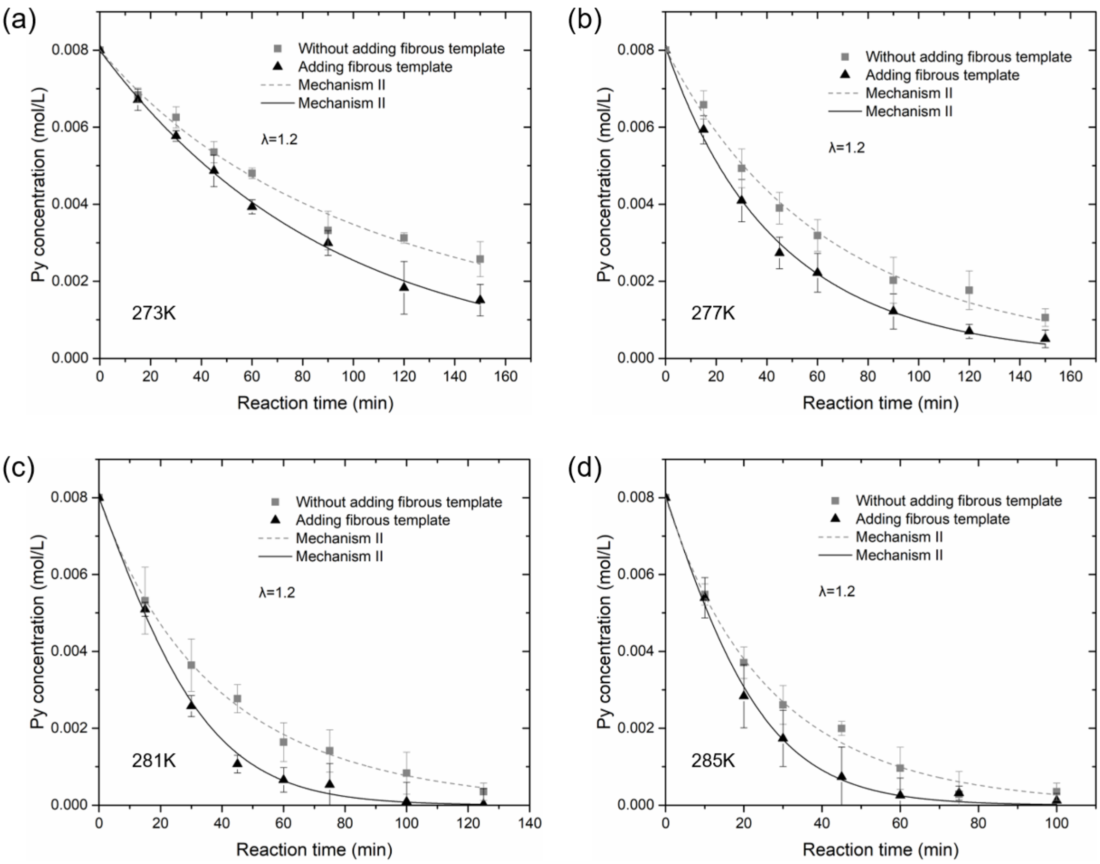

Figure 4.7. Comparisons of the experimental pyrrole polymerization data with theoretical fittings at different temperatures

Table 4.1 presents the reaction rate constants k_1 and k_2 calculated from the fitting results using Eqs. 4.10 and 4.11 at different reaction temperatures. The electrospun membrane as *in-situ* polymerization template has a negligible effect on the rate constant k_1. However, adding the fibrous template increases k_2 by 158.2-209.6%. This result indicates that the presence of an electrospun fibrous template enhances the reaction between oxidized oligomer and neutral monomer. The reason is attributed to the large surface area, typically above 10 $m^2 \cdot g^{-1}$ [43, 44], of the electrospun fibrous template.

Table 4.1. Reaction rate constants obtained from the theoretical fittings

Temperature (K)	k_1 (L·mol^{-1}·min^{-1})	k_2 (L·mol^{-1}·min^{-1})	k_1 (L·mol^{-1}·min^{-1})	k_2 (L·mol^{-1}·min^{-1})
	Without fibrous template		Adding fibrous template	
273	0.82	0.47	1.02	1.36 (189.4%)*
277	1.47	0.98	1.75	2.52 (158.2%)*
281	2.28	1.95	2.23	6.05 (209.6%)*
285	3.55	2.62	3.19	7.98 (204.0%)*

* Increasing of the k_2 compared to the one obtained without fibrous template

Figure 4.8 shows the schematic of the pyrrole *in-situ* polymerization with a fibrous template (Figure 4.8 a) compared to the polymerization without template (Figure 4.8 b). During *in-situ* polymerization, the generated pyrrole oligomers are first deposited onto the surfaces of the fibers. Then the pyrrole monomers in the liquid phase continuously reacting with the oxidized oligomers, growing the molecular chain to yield PPy polymer on the fiber surface. Eventually, the PPy polymers formed to fully cover the surface of the fibers. Therefore, considerable amount of reaction sites is available for the *in-situ* polymerization because of the large surface area of electrospun fibers presented in the reaction bath (*see* Figure 4.8 a). As a result, the reactions between oligomers and monomers are enhanced.

On the contrary, the generated pyrrole oligomers can only accumulate to form clusters when the fibrous template is absent in the polymerization process. The reaction sites with the pyrrole monomer are only available on the outer surface of these clusters (*see* Figure 4.8 b). Thus, the reactions between the pyrrole oligomers and monomers slow down because less surface area are provided by the oligomer clusters than the electrospun fibers.

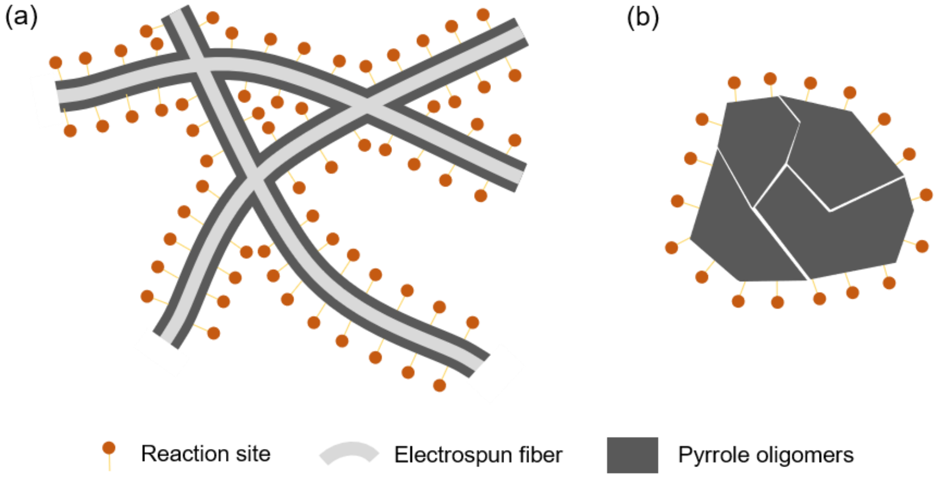

Figure 4.8. Schematic of the pyrrole polymerization process with (a) oligomer formed on the fiber surface and (b) oligomers formed on cluster

The preceding analysis shows that adding templates with large surface areas can enhance the rates of pyrrole polymerization. This finding concurs with several earlier studies [132, 171, 182] (as stated in Section 1) using various pyrrole *in-situ* polymerization templates including fabric fibers and nano-sized platelets. All these used templates are commonly regarded as materials with large surface areas [183, 184]. Thus, the preceding analysis in this paper can also explain the observations in the relevant literature.

4.4.3 Activation enthalpy and entropy

The Eyring equation (Eq. 4.15) is used to fit the changes of the reaction rate constant k_2 with the temperatures to further investigate the effects of the electrospun fibrous template on pyrrole *in-situ* polymerization process. Figure 4.9 shows $\ln(k_2/T)$ *versus* $1/T$ for two different reaction conditions. There is a linear relationship between $\ln(k_2/T)$ and $1/T$ regardless of the fibrous template. All the experiment results are well fitted with the Eyring equation with $R^2>0.96$.

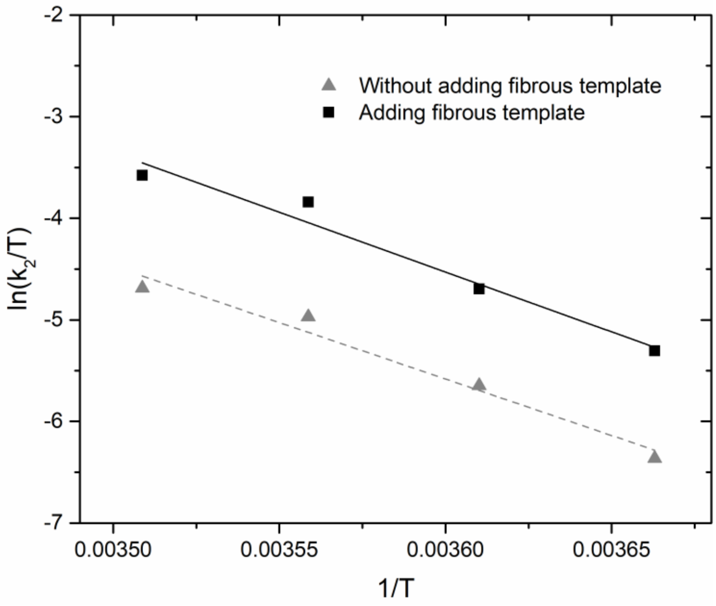

Figure 4.9. Fittings of Eyring equation to the pyrrole polymerization experiments (a) with and without the fibrous template

As seen in Eq. 4.15, the slope and intercept of the above fittings indicate the activation enthalpy and entropy of the reaction, respectively. Adding fibrous template has little effect on the reaction activation enthalpy. The values of the activation enthalpy are 97,902.4 J and 92,493.6 J for the experiment with and without fibrous template, respectively. The activation enthalpy should be identical because the pyrrole polymerization route remains the same for both cases. Thus, the slight difference between the two activation enthalpy values, which is less than 6%, may result from the experimental errors.

However, there is a strong impact of fibrous template on the activation entropy. The values of activation entropy are 101.9 $J \cdot K^{-1}$ and 74.0 $J \cdot K^{-1}$ when fibrous template is present and absent for *in-situ* polymerization, respectively. The results indicate that the overall transition state is more disordered in the reaction environment with the fibrous template because activation entropy is an indication of the disorder of the transition state in a chemical reaction [185].

The increase of activation entropy is resulted from the large surface area provided by the fibrous template. As explained in Section 4.4.2, considerable amount of reaction sites is created by the fibrous template in the *in-situ* polymerization process. As a result, the reactions between oligomers and monomers are enhanced, leading to the increase of the overall disorder during the reaction process.

4.4.4 Effects of dopant

Figure 4.10 shows the effects of dopant on the PPy yield during *in-situ* polymerization. The yield of PPy increases with the reaction time. However, the PPy formation rate is lowered by the addition of $Na_4Fe(CN)_6$, as indicated by that the reaction continuously lasted for at least 300 min. On the contrary, the PPy yield quickly raised up to maximum within only 75 min when the dopant is absent.

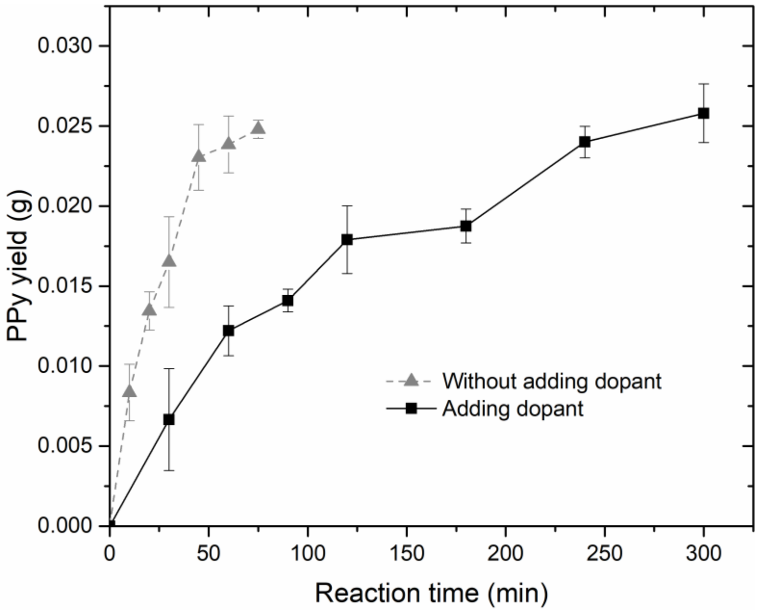

Figure 4.10. Effect of adding dopant on the PPy yield, initial Py: 0.016 mol/L, APS: 0.024 mol/L, $Na_4Fe(CN)_6$: 0.032 mol/L, temperature: 277K

The interaction between the dopant $Na_4Fe(CN)_6$ and the monomer pyrrole can help explain the negative effect of dopant on the pyrrole *in-situ* polymerization. The Fe^{2+} in the dopant has a strong chemical affinity to N atom in the pyrrole ring. Thus, the $Fe(CN)_6^{4-}$ can be anchored to the Pyrrole molecule [180]. As a result, the steric hindrance effect within the polymerization process is enhanced, leading to the slower reaction than that of the polymerization without dopant. A systematic kinetics study could further investigate the quantitative changes of the reaction rate constants with the adding of dopant. However, it's inaccurate to calculate the pyrrole concentration using data obtained by the gravimetric method in Section 3.3, because the doping of the final product PPy varies with reaction time. That is why a systematic kinetics study of the pyrrole polymerization with dopant added is not included in this study.

Despite the negative effect of the dopant, adding $Na_4Fe(CN)_6$ as a dopant strongly increases the conductivity of the fabricated PPy-based membrane. The electrospun pristine PAN membrane is electrically insulated before any treatment. The *in-situ* polymerization treatment results in the formation of PPy on the PAN fiber surface, which enables the membrane to conduct electrons. The conductivity of the membrane (*in-situ* polymerization under 277K for 60 min) is $4.2 \times 10^{-3} \pm 1.4 \times 10^{-3}$ mS·cm^{-1} without adding dopant, whereas the conductivity reaches 2.7 ± 0.3 mS·cm^{-1} for the membrane (*in-situ* polymerization under 277K for 240 min) treated with $Na_4Fe(CN)_6$ dopant.

4.5 Summary

A kinetics study of the *in-situ* polymerization process of PPy is carried out with electrospun PAN fibrous membranes as templates. First, two different kinetics models are developed based on existing PPy polymerization mechanisms. Mechanism II is found suitable for the rest of this study by comparing the fittings of the model to the experimental data. Then, *in-situ* polymerizations of PPy on electrospun PAN templates are conducted at different temperatures ranging from 273 to 285 K. The overall reaction rates of the *in-situ* polymerization process are higher than those without the electrospun fibrous template. The reaction rate constant k_2 (between oxidized oligomers and neutral monomers) increases by 158.2-209.6% when the fibrous template is added. The reactions between oligomers and monomers are enhanced, because considerable amount of reaction sites is created in the *in-situ* polymerization process due to the large surface area of electrospun fibers presented in the reaction bath. This explanation is further confirmed by the 37.7% higher activation entropy of the *in-situ* polymerization process compared to the polymerization without template. Adding electrospun fibrous template into the *in-situ* polymerization bath increases the available reaction sites between reactants, leading to the increase of overall disorder of the reaction process. In addition, the effect of adding $Na_4Fe(CN)_6$ as dopant is also studied. The results show that the PPy formation rate is slower with the adding of dopant. It is explained by the steric hindrance effect within the polymerization process caused by the interactions between $Fe(CN)_6^{4-}$ and Py monomer.

Chapter 5

Redox-active Separator for Enhancing the Capacity of Lithium-ion Battery

The preceding chapters confirm the importance of developing redox-active separator for LIB. In addition, Chapter 4 prepares the PPy composite nanofibers by *in-situ* polymerization, and provides a kinetics study to understand the mechanism of the fabrication process. Based on these progresses, the proposed PPy based redox-active separator is fabricated and characterized in this chapter, followed by evaluating the performance of the separator in LIB coin cells.

5.1 Introduction

Lithium-ion batteries (LIBs), as one of the most widely applied energy storage devices, have played a crucial role in modern day-to-day life. The battery separator is one of the crucial components in LIB. The fast-growing demand for high-performance LIBs in various applications requires the development of superior separators.

Electrospun nanofibrous separator receives considerable attention among all the up-to-date progresses of battery separator research works. Section 2.1 has reviewed the recent achievements of electrospun nanofibrous separators with a focus on the separator properties and the battery performances of using such separator. Although, superior battery performances with nanofibrous separators are reported in literatures, most research works are still focused on using electrochemical inert material as battery separator.

As discussed in Section 1.2, a novel strategy is to enhance the battery separator with redox activity. The redox-active separator can participate in the battery reactions and then provide additional battery capacity. The use of such redox-active separator can eventually increase the energy density of LIBs.

In this chapter, the nanofibrous redox-active separators is fabricated based on electrospinning and *in-situ* polymerization process. The obtained separator exhibits a bi-layer structure, including a lay of Polyacrylonitrile (PAN)@PPy core-shell structured fibers and another layer of PAN fibers. The PAN@PPy composite layer serves to enhance the battery capacity stemmed from its redox activity within the voltage potential range of battery operation. Meanwhile, the PAN layer acts as the insulating barrier to prevent the battery from short-circuit. The bilayer separator, in its entirety, retains a considerable amount of liquid electrolyte in its well-developed porous structure allowing the migration of ions during the battery cycling. This study presents detailed characterizing properties of the electrospun nanofibrous redox-active separator, including the separator morphology, chemical composition, thermal stability, and mechanical property. Moreover, the redox-active separators are assembled into LIB coin cells to study the battery performance of using such separators.

5.2 Experiment

5.2.1 Materials

Polyacrylonitrile (PAN, M_W=150000), Pyrrole (Py, purity>98%), Ammonium persulfate (APS, purity>98%), Sodium ferrocyanide ($Na_4Fe(CN)_6$, purity>98%), N,N-dimethylformamide (DMF, purity>99.8%), and liquid electrolyte of 1 M $LiPF_6$ in ethylene carbonate (EC)/dimethyl carbonate (DMC) (1:1 in volume) are purchased form Sigma Aldrich (Canada). Commercial microporous polypropylene (PP) separators used for comparison are obtained from the manufacture. All chemicals are used as received without any further purification.

5.2.2 Fabrication of nanofibrous redox-active separator

Figure 5.1 illustrates the fabrication process of the redox-active separator prepared in this study. A laboratory-made electrospinning device is used to produce PAN nanofibrous membranes as follows. First, PAN polymer is dissolved into DMF to prepare the solution of 10 wt.% concentration as electrospinning precursor. Then, the PAN solution is loaded into a syringe with a metallic needle (with inner diameter of 0.514 mm) connected to a laboratory-made positive high voltage supply. A grounded drum collector (at a rotating speed of 30 rpm) covered with non-stick aluminum foil (Reynolds wrap, USA) is placed 11 cm away from the needle tip and used as a fiber collector. Finally, continuous fiber jets are generated from the needle tip to form a membrane on the fiber collector when the voltage is adjusted to 7.5 kV and the PAN solution is pumped at a steady flow rate of 0.4 ml/hr.

The collected electrospun PAN membrane is peeled off from the aluminum foil and immersed into 15 mL pyrrole aqueous solution (0.016 mol/L) blended with $Na_4Fe(CN)_6$ (0.032 mol/L) for *in-situ* polymerization. $Na_4Fe(CN)_6$ is adopted as a dopant for PPy synthesis because the final product exhibits great electrochemical properties, which has been reported as a potential material for energy storage [180]. Then, APS is dissolved into 2 ml of deionized water and added into the pyrrole solution dropwise. (The concentration of APS in the reaction bath is 0.024 mol/L.) The *in-situ* polymerization reaction is kept at 275 K in a cooler for 3.5 hours to produce PAN@PPy composite membrane. Finally, the immersed membrane is taken out from the solution and rinsed thoroughly using deionized water, followed by drying under vacuum at 80 ℃ in a vacuum oven for at least 12 hours (Vacuumoven-001, LeDAB, Canada).

Then, the obtained PAN@PPy membrane is affixed to a grounded collector for second electrospinning to produce a bilayer membrane. The operational parameters are kept the same as the first electrospinning to generate PAN nanofibers on top of the PAN@PPy membrane. Finally, the bilayer membrane, consists of one layer of PAN@PPy nanofibers and another layer of PAN nanofibers, is used as redox-active separator for lithium-ion battery.

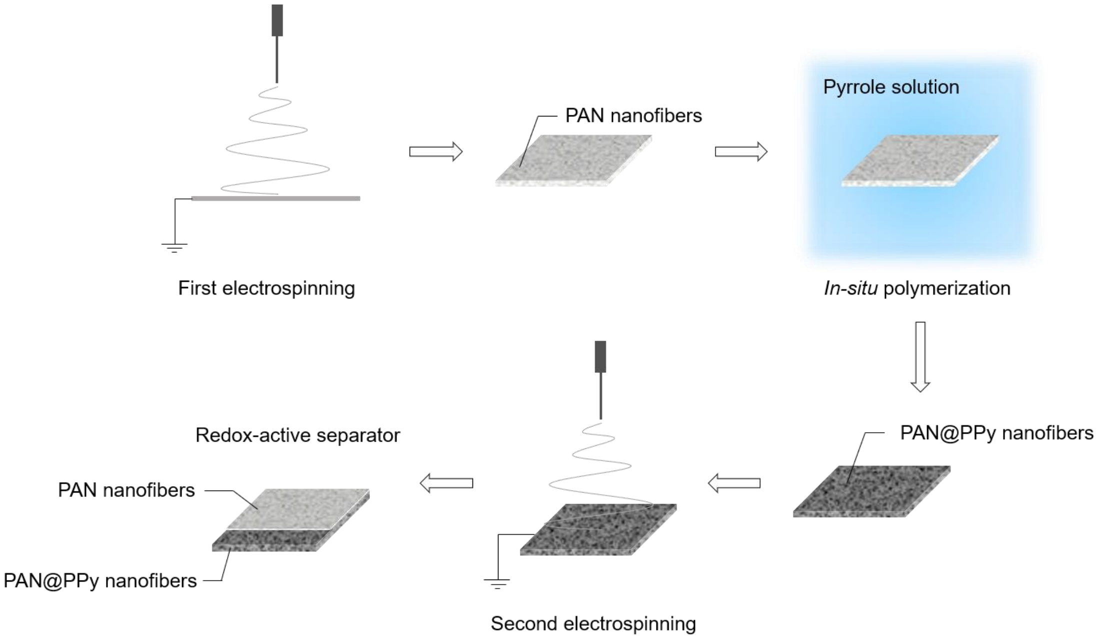

Figure 5.1. Schematic of the fabrication method of the redox-active separator in this study

5.2.3 Separator characterization

The morphology of the fabricated separator is characterized using a scanning electron microscope (SEM, UltraPlus FESEM, Zeiss, Germany), which is available at WATLab in University of Waterloo, after sputtering with a thin layer of gold for 120 s. Then, the fiber size distribution and pore size distribution of the separator are obtained from the imaging processing of the corresponding SEM images. In order to improve the accuracy of the results obtained, two SEM images with different magnifications of a same separator are imported into MATLAB software. Then, the size distributions are calculated from the combination results of these two SEM images following a method published in a previous work [186].

The functional chemical groups of the fabricated separator are characterized by Fourier transform infrared (FTIR) transmittance spectra (8400S, Shimadzu, Japan), which is available at G2N lab in University of Waterloo, performed at the wavenumbers ranging from 500-3500 cm^{-1}. In addition, the chemical composition of the separator is determined by X-ray photoelectron spectroscopy (XPS, Thermo VG Scientific Escalab 250, USA) located at WATLab in University of Waterloo.

The porosity of the separator is measured by the n-butanol uptake tests and calculated using the equation:

$$\text{Porosity (\%)} = \left(W_{nw} - W_d\right) / \left(\rho_b \times V\right) \tag{5.1}$$

where W_d and W_{nw} are the weights of dry separator and n-butanol wetted separator, respectively, ρ_b is the density of n-butanol, and V is the geometric volume of the separator.

The electrolyte uptake of the tested separator is measured by weighing the separator before and after soaking in the liquid electrolyte for 2 hours. Then, the electrolyte uptake is calculated as:

$$\text{Electrolyte Uptake (\%)} = \frac{W_{ew} - W_d}{W_d} \times 100 \tag{5.2}$$

The ionic conductivity of the fabricated separator is measured by electrochemical impedance spectroscopy (EIS) using an electrochemical work station (PMC2000, Princeton, USA), which is carried out by a contractor located in China. The EIS is performed on electrolyte-soaked separators sandwiched between two stainless steel electrodes over a frequency range of 100 kHz to 0.1 Hz at 10 mV AC amplitude. Then, the ionic conductivity of the tested separator is calculated as:

$$\sigma = \frac{d}{R_b \times S} \tag{5.3}$$

where d is the separator thickness (cm), S is the effective area (cm^2) of the separators, and R_b is the bulk resistance obtained from the intercept of Nyquist plot.

The dimensional thermal stability of separator is characterized by its heat shrinkage rate. A circular separator is placed in an oven to expose at 160° C for 1 hour, and the heat shrinkage rate is then calculated from the area change of the separator using image processing in ImageJ software.

Differential scanning calorimetry (DSC) spectra of separators are collected using a differential scanning calorimeter (Q2000, TA Instruments, USA), which is available at the analytical lab in University of Waterloo, at a heating rate of 10 °C/min in N_2 atmosphere.

Mechanical properties of separators are tested on an universal testing machine（5548, Instron, USA）, which is available at CAMJ lab in University of Waterloo, at the pulling rate of 10 mm/min. Each type of separator sample has been tested at least 3 times to calculate the average value.

5.2.4 Battery performance evaluation

The fabricated redox-active separator, electrospun pristine PAN separator and commercial PP separator are punched into discs of 19 mm diameter (using a precision disc cutter, MSK-T-07, MTI, USA) and assembled into CR2032 coin cells in a N_2 filled glove box for battery performance evaluation. All the battery testing is contracted out to a service company located in China. The redox-active layer (*i.e.* PAN@PPy layer) of the redox-active separator contacts the cathode side, while the inert layer (*i.e.* PAN layer) contacts the anode side in the assembled battery cells. The assembled LIB half-cell consists $LiFePO_4$ (LFP) as cathode, lithium metal as anode, and 1M $LiPF_6$ solution as liquid electrolyte. The LFP cathode is prepared by blending LFP, carbon black, and polyvinylidene fluoride (PVDF) binder at a weight ratio of 8:1:1 into N-Methyl-2-pyrrolidone slurry, followed by casting it onto aluminum foil. The final mass loading of the LFP on the cathode is about 3.5 g/cm^2.

The charge-discharge test of the assembled LIB coin cells is carried out in a battery cycler (CT200, Land, China) in a potential range of 2.5-4.2 V (versus Li$^+$/Li) at 0.2-2 C rate. The charge/discharge rate is calculated based on the mass of LFP in cathode for comparisons between battery cells with different separator (*i.e.*, 1 C = 170 mA·g^{-1}). The specific capacity of the tested battery cell is also calculated based on the mass of LFP in cathode.

The cyclic voltammetry measurements of the assembled LIB coin cells are carried out using an electrochemical work station (PMC2000, Princeton, USA) between 2.5 and 4.2 V (versus Li+/Li) at the scanning rate of 0.2 mV/s.

5.3 Results and discussion

5.3.1 Morphology and composition characterization

Figure 5.2 shows the digital photos and SEM images of the fabricated redox-active separator. The separator is a Janus-faced membrane with a black redox-active side and a white inert side. Both layers of the separator are consisted of randomly oriented nanofibers, and exhibit well-developed interconnected porous structures. The surface of the fibers in the inert layer is smooth, whereas the fibers in the redox-active layer is much rougher (*see* Figure 5.2 c, e). Moreover, the detailed SEM image with large magnification (*see* Figure 5.2 f) confirms the core@shell structure of the fibers in the redox-active layer.

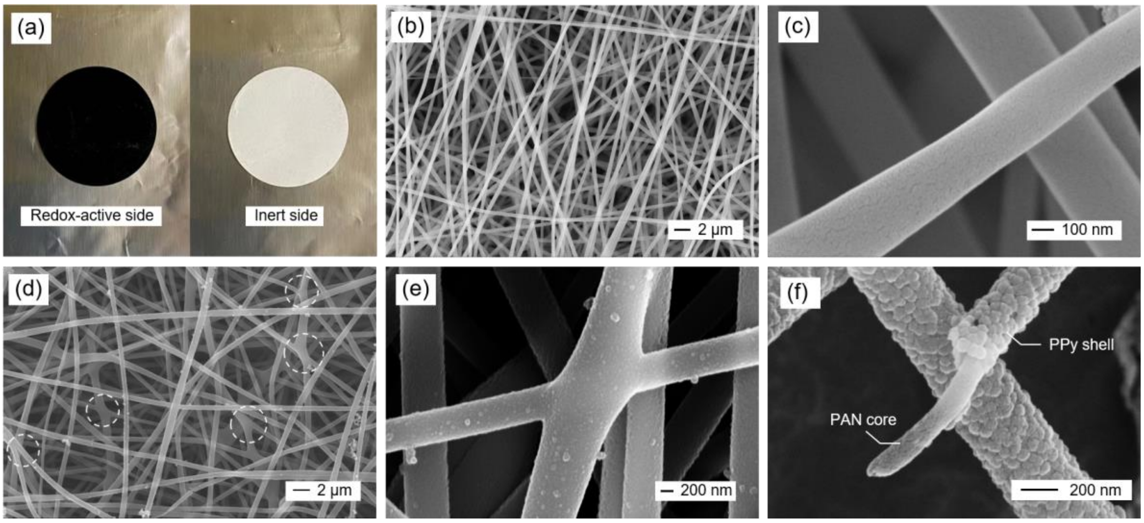

Figure 5.2. (a) Digital photo of the fabricated redox-active separator. (b) (c) SEM images of inert side of the separator. (d) (e) (f) SEM images of redox-active side of the separator

The fabricated separator exhibits a bilayer structure with different nanofibers constituting each layer. The inert layer is composed of pristine electrospun PAN nanofibers, whereas the nanofibers in the redox-active layer is fabricated by the *in-situ* polymerization of PPy onto PAN nanofibers. The black color of the redox-active layer indicates that the PPy formed from the *in-situ* polymerization stay on and fully cover the surfaces of the PAN nanofibers, as black is the characteristic color of the PPy polymer. This speculation is confirmed in the Figure 5.2 (f) which shows that the electrospun PAN nanofiber is fully wrapped by the produced PPy polymer. Thus, the PAN@PPy core-shell fiber structure in the redox-active layer is confirmed.

In addition, the forming of the PPy is further verified by the FTIR results as shown in Figure 5.3. The infrared absorption peaks of the pristine PAN nanofibers represent the characteristic functional groups of PAN polymer. The absorption peaks at 2920 and 1452 cm^{-1} represent the $-CH_2-$ absorption and its scissor vibration, respectively; The peak at 2240 cm^{-1} refers to the $-C\equiv N$ stretching vibration. (The other peaks appeared in the spectrum indicate the existing of the DMF solvent residue, as the peaks at 1664 and 1385 cm^{-1}

represent the C=O and =C-N groups, respectively.) The infrared spectrum of the PAN@PPy nanofibers verifies the forming of PPy polymer. The peaks at 896 and 1032 cm^{-1} represent the C-H out-plane and in-plane vibration, respectively; Peaks at 1448 and 1553 cm^{-1} represent the C=C and C=N stretching in the pyrrole ring. (all the above information is obtained from the FTIR handbook [187]) Moreover, the PPy loading in the redox-active layer is determined as 99.9±19.4 mg·cm^{-3} by comparing the weight differences of the electrospun samples before and after pyrrole *in-situ* polymerization treatment.

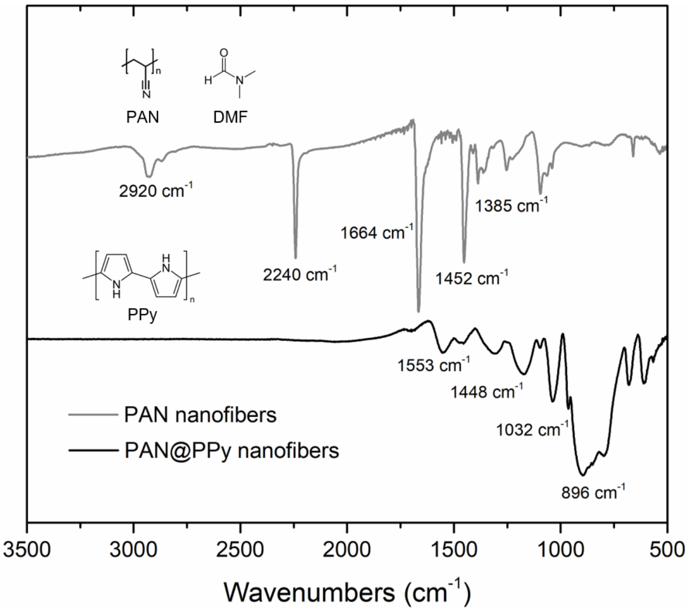

Figure 5.3. FTIR spectra of electrospun PAN nanofibers and PAN@PPy nanofibers

Figure 5.4 shows the chemical composition of the PPy fiber shell characterized by XPS spectra. The PAN fiber core has negligible interference on the element detection of PPy, because the XPS only allows the analysis of elements in the outermost 10 nm of the surface [188] (the wall thickness of the PPy shell is much greater than 10 nm, which is discussed in the context corresponding to Figure 5.5). The result shows that the PPy fiber shell is doped by SO_4^{2-} and $Fe(CN)_6^{4-}$, as evidenced by the element detection of S, O and Fe. The

SO_4^{2-} is derived from the APS oxidant used in the *in-situ* polymerization, whereas the $Fe(CN)_6^{4-}$ is intentionally added as dopant. Finally, the chemical composition of the PPy fiber shell fabricated in this study is determined as $PPy_{18.5}^{7+}\cdot(SO_4)_{1.5}^{3-}\cdot Fe(CN)_6^{4-}$ by calculating the proportion of S 2p and Fe 2p to the N 1s content in PPy. The doping level of the $Fe(CN)_6^{4-}$ is comparable to the result reported in literature [180] ($PPy_{17.1}^{7+}\cdot Fe(CN)_6^{4-}$), which fabricates the $Fe(CN)_6^{4-}$ doped PPy into nanoparticles. The result concludes that the *in-situ* polymerization of PPy onto electrospun nanofibers has negligible interference on the $Fe(CN)_6^{4-}$ doping.

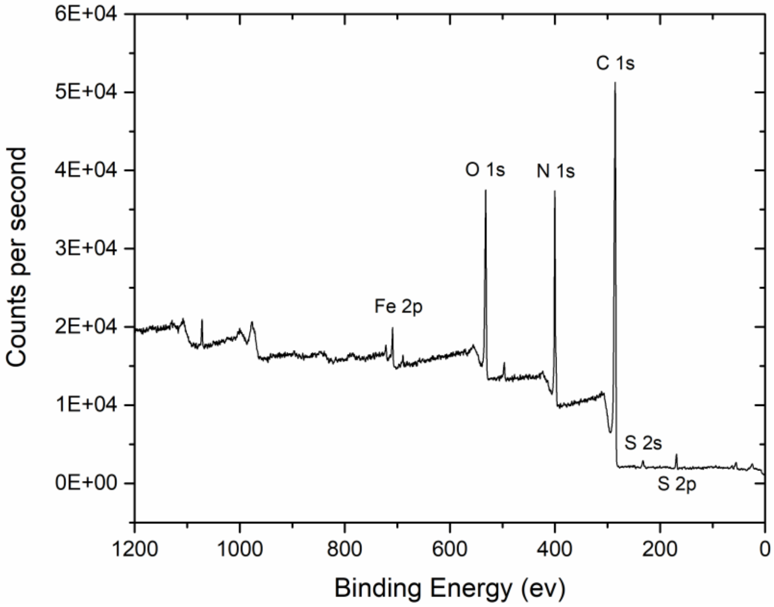

Figure 5.4. XPS spectra of PAN@PPy nanofibers

It is worth noting that some adjacent PAN@PPy fibers in the redox-active layer are joined together at where they contact (*see* white circles in Figure 5.2 d, and Figure 5.2 e). This is resulted from the *in-situ* polymerization of PPy onto the electrospun PAN nanofibers. The PPy is formed to wrap both adjacent fibers inside of it to form bindings during the *in-situ* polymerization process. These joint fibers can improve the mechanical strength of the fabricated separator, which is discussed in Section 5.3.3.

Figure 5.5 compares the fiber and pore size distribution of the inert and redox-active layer of the fabricated separator. The inert layer, consists of pristine PAN nanofibers, exhibits an average fiber size of 478.7±4.8 nm; and an average pore size of 750.4±44.0 nm. The PAN@PPy nanofibers in the redox-active layer exhibits greater average fiber size of 619.5±10.2 nm; and smaller average pore size of 650.3±34.8 nm. The size differences of the two fabricated layers are attributed to the existing of the PPy fiber shell in the redox-active layer. The forming of the PPy shell increases the fiber diameter and decreases the pore size. In addition, the increase of the fiber size in the redox-active layer indicates that the wall thickness of the PPy sheath is about 70 nm or so.

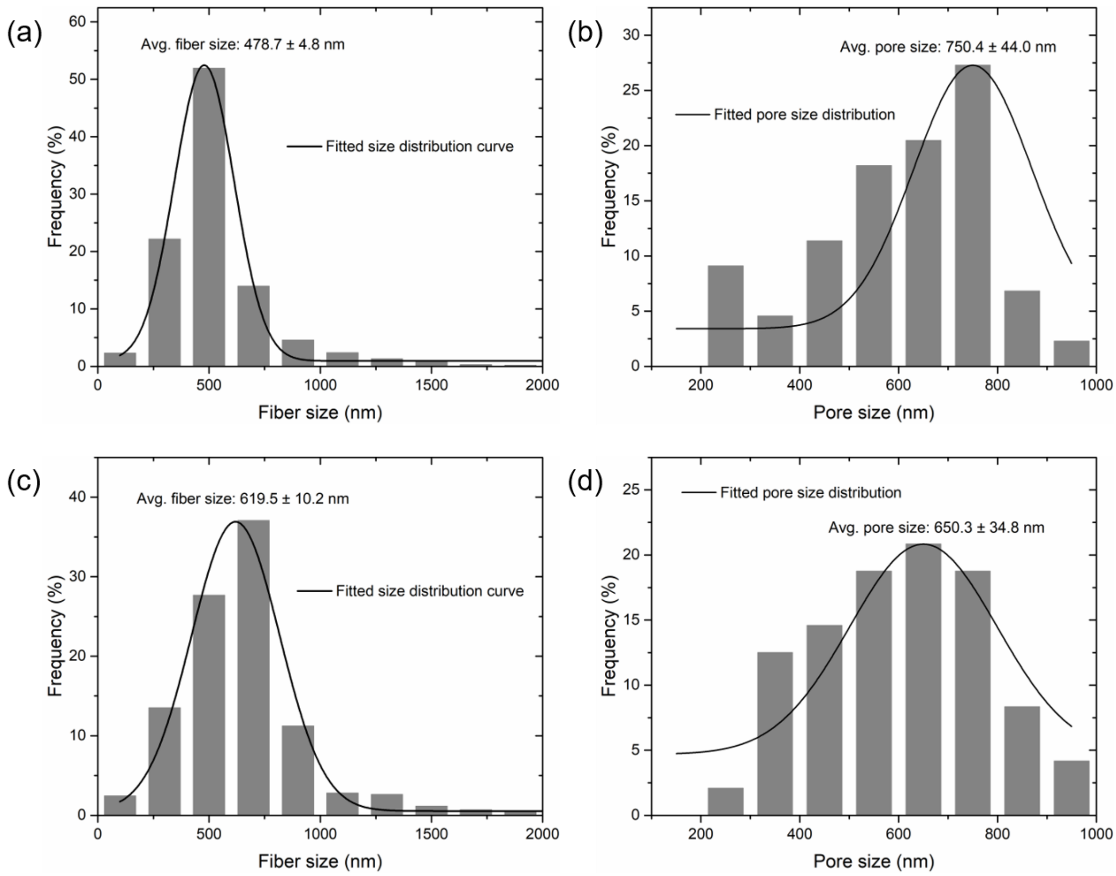

Figure 5.5. Fiber size distribution and pore size distribution of (a) (b) electrospun PAN inert layer and (c) (d) PAN@PPy redox-active layer

Table 5.1 presents the porosity and electrolyte uptake of the separators used in this study. The highest porosity of 85.7±7.0% is obtained by electrospun PAN separator. The redox-active separator exhibits a lower porosity of 79.3±7.1%. The commercial PP separator shows only 41% of porosity (The data is obtained from the manufacture. However, future works should measure the porosity of the commercial separator using the method listed in Section 5.2.3 for consistent comparison) as the lowest. The electrolyte uptakes of the separators are positively correlated to its porosity, as the redox-active separator, PAN separator and PP separator exhibit 310.7±32.2%, 294.6±31.5%, and 81.5±17.4% of electrolyte uptake, respectively.

Table 5.1. Porosity and electrolyte uptake of different separators used in this study

	Thickness	Porosity	Electrolyte uptake
Redox-active separator	50 μm	79.3 ± 7.1%	294.6 ± 31.5%
Electrospun PAN separator	50 μm	85.7 ± 7.0%	310.7 ± 32.2%
Commercial PP separator	25 μm	41% [a]	81.5 ± 17.4%

[a] obtained from the manufacture

The porosities of the redox-active separator and the electrospun PAN separator are considerably greater than that of a commercial separator. It is owing to the interconnected nanofibrous structures of these fabricated separators (*see* Figure 5.2). The porosity of the redox-active separator is about 6% smaller compared to the electrospun PAN separator. This result indicates that higher separator porosity can be achieved by smaller fiber diameter with greater pore size (*see* Figure 5.5), since more void space is available between thinner fibers.

Similarly, the redox-active separator and the electrospun PAN separator achieves more than 3 times higher of the electrolyte uptake than commercial PP separator. This high amount of electrolyte uptake is achieved not only because of the higher porosity of the fabricated separator in this study (considering that the porosity is only about 2 times higher than the commercial PP separator as shown in Table 5.1), but also its great affinity to the electrolyte. The commercial PP separator is criticized for its poor electrolyte wettability and affinity [43], whereas the redox-active separator and PAN separator fabricated in this study exhibit great electrolyte affinity. This is because that both PAN and PPy polymers contain a large amount of N containing groups, which has a strong affinity to Li^+ in the electrolyte [189]. In this study, the high porosity and larger electrolyte uptake of the fabricated separators are deemed important for reducing the mass transfer resistance between electrodes [8, 117].

In addition, Figure 5.6 shows the Nyquist plots of symmetric cells with different separators obtained from EIS measurements. The intercept of the obtained data on the real axial corresponds to the bulk resistance of the tested separators. The commercial PP separator presents the highest bulk resistance of $1.2 \pm 0.02\ \Omega$, even though its thickness is only half of the redox-active separator and electrospun PAN separator (*see* Table 5.1) used in the testing cells. The reason is attributed to the low porosity and electrolyte uptake of the commercial separator as preceding discussed, which hampers the mass transfer of Li ions through channels of separators. Thus, the calculated ionic conductivity of the separators follows the order of electrospun PAN separator ($2.26 \pm 0.09\ mS \cdot cm^{-1}$) > redox-active separator ($1.57 \pm 0.06\ mS \cdot cm^{-1}$) > commercial PP separator ($0.75 \pm 0.02\ mS \cdot cm^{-1}$).

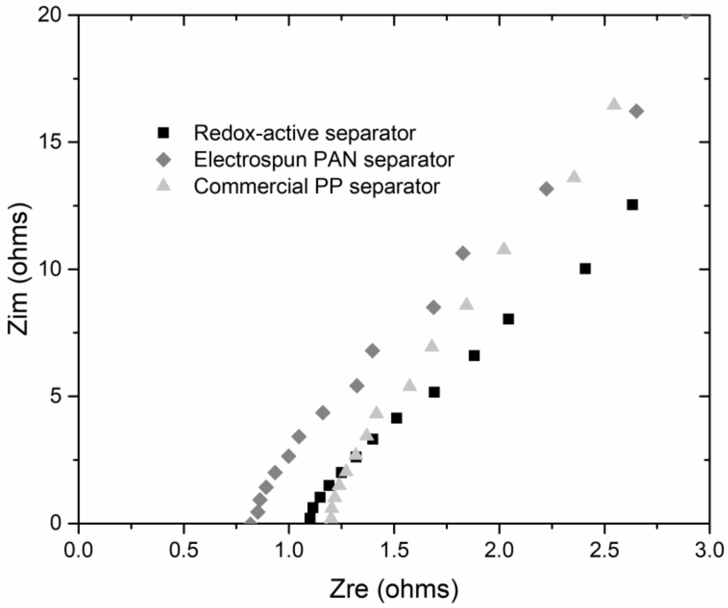

Figure 5.6. Typical Nyquist plots of symmetric cells with different separators

Table 5.2 compares the ionic conductivity of the separators fabricated in this study with the data reported in literature. All the data summarized in this table is for electrospun PAN separators, which is the same material used in this study for separator fabrication. The reported ionic conductivities of the electrospun PAN separators range from 1.11 to 2.6 mS·cm^{-1}, due to different fabrication parameters and conditions adopted in different research works. As a result, the porosity and electrolyte uptake also vary from study to study. However, Table 5.2 concludes that the separators fabricated in this study achieved the same level of physical properties as typical electrospun separators which is superior than the commercial PP separator.

Table 5.2. Comparison of the porosity, electrolyte uptake and ionic conductivity between the separators used in this study and from literature

	Porosity	Electrolyte uptake	Ionic conductivity ($mS\cdot cm^{-1}$)	Ref.
Electrospun PAN	69%	257%	2.0	[28]
Electrospun PAN	87.4%	306%	1.11	[190]
Electrospun PAN	76%	-	2.6	[59]
Electrospun PAN	60%	430%	1.21	[191]
Electrospun PAN	85.7 ± 7.0%	310.7 ± 32.2%	2.26 ± 0.09	This study
Redox-active separator	79.3 ± 7.1%	294.6 ± 31.5%	1.57 ± 0.06	This study
Commercial PP separator	41%	81.5 ± 17.4%	0.75 ± 0.02	This study

5.3.2 Thermal stability

The thermal stability of the separators is characterized by the DSC thermograms as shown in Figure 5.7. The redox-active separator and the electrospun PAN separator exhibit a relatively stable heat flow before 250 °C. However, a strong endothermic peak is observed for the PP separator around 163 °C. The redox-active separator is further heated up to 350 °C to locate the temperatures of its thermal reactions. The results reveal two exothermic peaks at 289 and 312 °C, respectively.

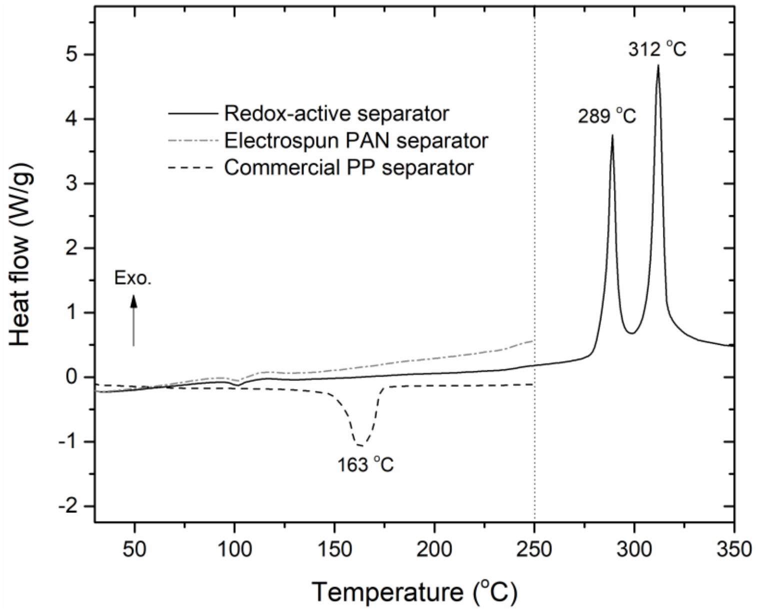

Figure 5.7. DSC thermograms of the redox-active separator and the commercial PP separator

The DSC results indicate that the redox-active separator and electrospun PAN separator have better thermal stability than the commercial PP separator. The melting of the PP polymer is corresponding to its endothermic peak at 163 °C. However, the thermal properties of the redox-active separator and PAN separator are relatively stable up to 250 °C. Further heating up the redox-active separator causes two strong exothermic peaks. The first peak at 289 °C is attributed to the cyclization of the PAN polymer within the redox-active separator. Heating up the PAN polymer to around 290 °C causes the radical reactions in the -C≡N groups, leading to formation of hexagonal carbon nitrogen rings within the PAN molecules [117]. The second exothermic peak at 312 °C is caused by the thermal reactions of the $Fe(CN)_6$ groups which are doped into the PPy polymer. At temperatures higher than 300 °C, the internal redox reactions between iron ions and the coordinated CN^- occur, leading to the formations of cyanates and carbonates [192].

In addition, Figure 5.8 shows the digital photos of the separators before and after thermal exposed at 160 °C for 1 hour. The dimensional stability of a separator is deemed important to protect the battery cells from internal short circuit at high temperatures. Both the redox-active separator and electrospun PAN separator can maintain its dimensions at the temperature of 160 °C. However, the commercial PP separator suffers 36% shrinkage at the same temperature. Thus, it is safer to use the redox-active separator or the electrospun PAN separator in a LIB cell compared to the use of a commercial PP separator.

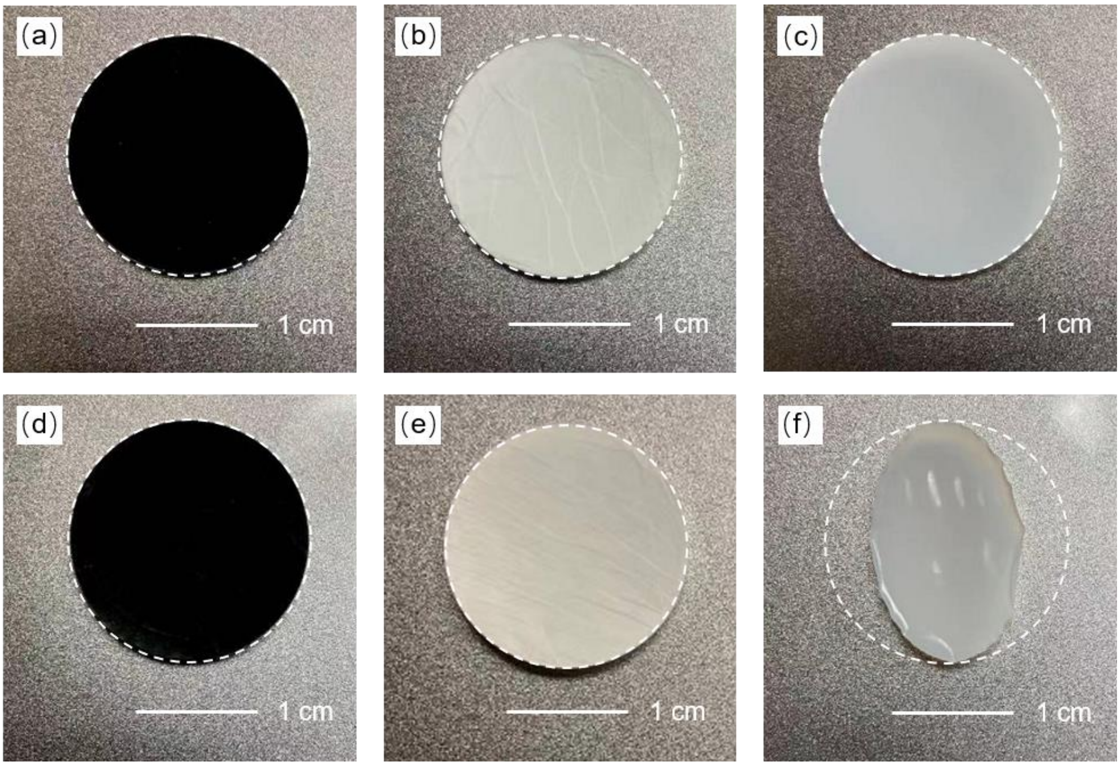

Figure 5.8. Digital photos of redox-active separator, electrospun PAN separator, and commercial PP separator (a) (b) (c) before and (d) (e) (f) after thermal exposure at 160 °C for 1 hour.

5.3.3 Mechanical properties

Figure 5.9 shows the stress-strain curves of the redox-active separator and the electrospun PAN separator. The stress that the membrane undergoes increase with the increase of strain until it reaches the ultimate tensile strength (UTS). After the UTS of 6.9±0.4 MPa, the stress of the PAN separator drops fast with further increase of strain, which indicates its fracture. The redox-active separator exhibits higher UTS of 7.8±0.6 MPa, followed by a fast drop of the stress to about 3 MPa at the strain of 25%. Then, the separator undergoes this stress until the strain reaches about 150% before fracture. `1

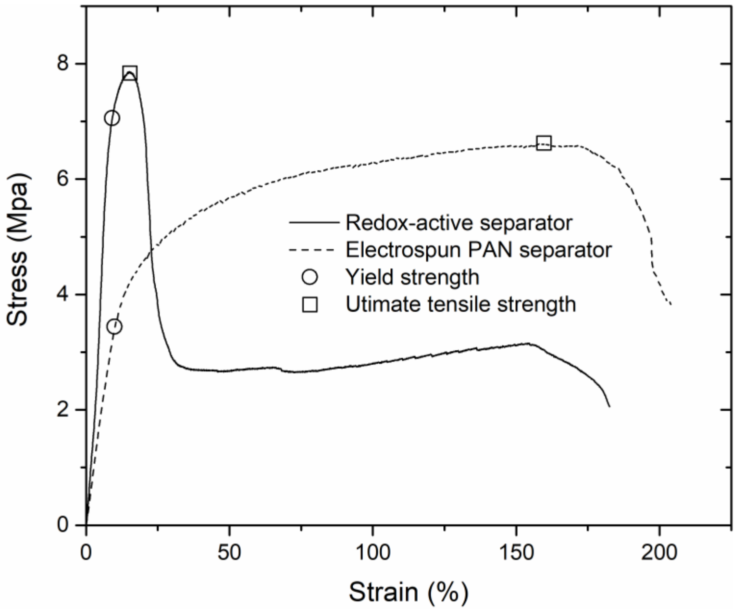

Figure 5.9. Typical stress-strain curves of the redox-active separator and PAN separator

The stress-strain curve of the PAN separator shows two different regions before fracture. The first region is the elastic deformation region, where the stress is proportional to the strain until it reaches the yield strength of 3.5±0.1 MPa. In this region the shape change of the PAN separator under the applied force is temporary. The second region is the strain hardening region, where the stress continually increases while the separator is further stretched. The membrane undergoes plastic deformation in this region, meaning the shape change is irreversible. The wide hardening region of the PAN separator is evidenced by the strain region from about 10% to 160%.

The stress-strain curve of the redox-active separator shows a different pattern compares to the PAN separator. The elastic deformation region and the strain hardening region are observed for the redox-active separator before the UTS (similar to the electrospun PAN separator). However, the separator withstands further strain up to 150% at a stress of 3 MPa before final fracture. This is because the redox-active separator has a bilayer structure. The UTS is mainly attributed to the PAN@PPy fibrous layer, whereas the large strain capability is attributed to the pristine PAN layer. The mechanical strength of the PAN@PPy layer is greater than the PAN layer, due to the PPy sheath fiber formed from the in-situ polymerization process which results in bindings between some adjacent fibers (*see* Figure 5.2 e). The change of the nanostructures improves integrity, thus enhances the mechanical strength of the separator without sacrificing flexibility. As results, the redox-active separator exhibits greater mechanical properties than the electrospun PAN separator, including 82.9% higher of yield strength (6.4 ± 0.6 MPa); 187.3% higher of Young's modulus (70.1±14.1 MPa); and 13.0% higher of UTS (7.8±0.6 MPa).

It is worth noting that the mechanical strength of electrospun nanofiber-based separators is still weaker than that of a commercial separator. Figure 5.10 compares the UTS of the separators used in this study with different electrospun separators obtained from literatures. Most electrospun fiber-based separators exhibit the UTS below 20 MPa including the redox-active separator and electrospun PAN separator fabricated in this study. However, the highest UTS is achieved by the commercial separator. The UTS of the commercial PP separator used in this study is 139.3 MPa in the machine direction, and 13.7 MPa in the transverse direction (The data is obtained from the manufacture. However, future works should test the strength of the commercial separator using the testing machine listed in Section 5.2.3 for consistent comparison). Thus, in order to achieve endurable battery performance, the thickness of the redox-active separator and electrospun PAN separator used in this study for battery testing is about 50 μm (whereas the thickness of the commercial PP separator is 25 μm).

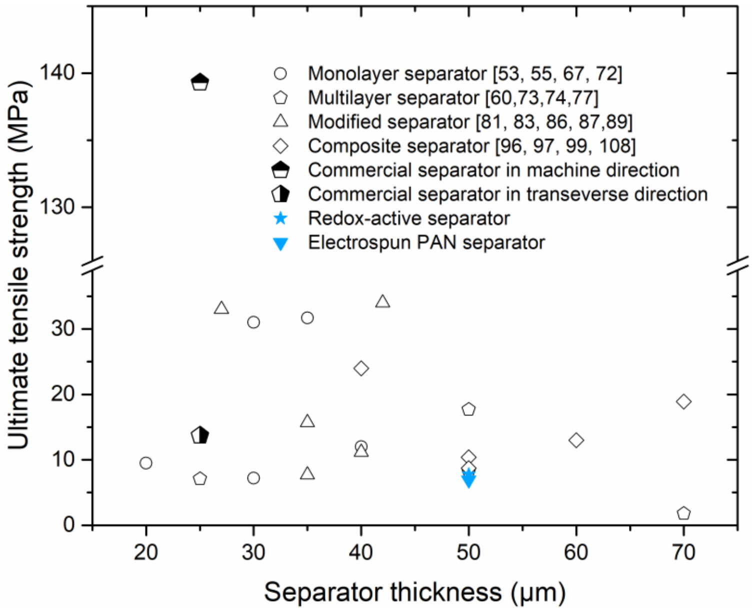

Figure 5.10. Comparison of the ultimate tensile strength of different electrospun separators and the separators used in this study

5.3.4 Battery performance

Figure 5.11 (a) presents the first cycle charge-discharge curves of Li/$LiFePO_4$ half cells containing different separators at 0.2 C. In the charging step, the electrode voltage quickly climbed to a voltage plateau. Then, the electrode maintains at this voltage till the end of charging, where the voltage raised quickly to the cut-off voltage of 4.2 V. On the contrary, the electrode voltage drops to the voltage plateau of 3.4 V at the beginning of the discharging step. Then, the discharge voltage is maintained before a quick drop to the cut-off voltage of 2.5 V. The discharge capacity of the battery cell containing the redox-active separator is 227.0 mAh·g^{-1}, which is higher than the ones containing electrospun PAN separator (161.6 mAh·g^{-1}) and commercial PP separator (155.9 mAh·g^{-1}).

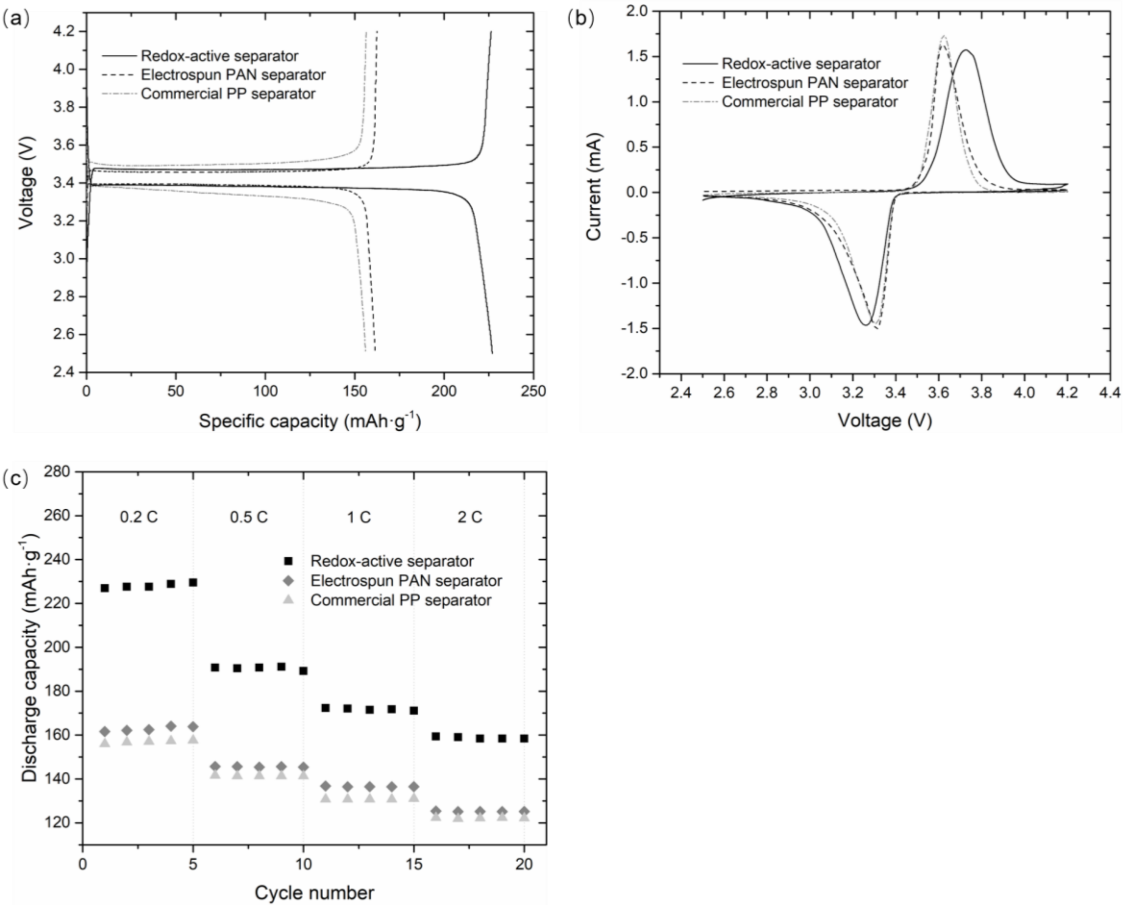

Figure 5.11. Battery performance of Li/LiFePO4 cells containing different separators. (a) first cycle charge/discharge profiles. (b) Cyclic voltammograms. (c) Rate capability

The first-cycle coulombic efficiency of the battery with redox-active separator is 98.3%, which is slightly lower than that of the ones with conventional separators (above 99%). This result indicates that more lithium ions become irreversible during the battery cycling when using the redox-active separator. Admittedly, the coulombic efficiency of 98.3% is acceptable for battery operation, the slightly poor coulombic efficiency is attributed to the PPy polymer, which is participating in the battery reactions with a slightly poor coulombic efficiency than the LFP cathode. Similar efficiencies are also reported in literature [180, 193] which directly uses PPy polymer as a battery cathode.

The cyclic voltammograms (CV) in the Figure 5.11 (b) further confirms the enhanced battery capacity for cells with redox-active separator. All the battery cells exhibit well reversibility as indicated by the symmetric peaks obtained. The redox-active separator exhibits wider cathodic peak and anodic peak compared to the other two separators, which explains the enhanced battery capacity presented in the charge/discharge tests. In addition, the CV peaks of the battery containing redox-active separator is broader than the other two, because it is a combination of two redox reactions including the reactions of LFP cathode and also the PPy redox-active separator layer.

Figure 5.11 (c) shows the rate capability of the battery cells containing different separators. All the battery cells exhibit good rate capability of retaining more than 70% of its original capacity at a high rate of 2 C. The battery cell with redox-active separator obtains the highest capacity at all current rates. It delivers 158.7 $mAh \cdot g^{-1}$ of capacity at the highest rate of 2 C, which is even higher than the battery cell with a commercial PP separator at the lowest rate of 0.2 C (156.9 $mAh \cdot g^{-1}$).

The cycling of the battery cell with redox-active separator remains stable at different current rates without signs of separator breakage (*see* Figure 5.11 c). It should be mentioned that even though the PAN@PPy nanofiber layer in the separator is electrically conductive, it will not short-circuit the battery when the separator is partially penetrated by the lithium dendrite formed on the anode. (The growing of the lithium dendrite is an undesirable phenomenon in a LIB, which is caused by the accumulation of extra lithium ions on the anode surface and cannot be absorbed into the anode in time. The growing of the lithium dendrite may eventually pierce the separator and cause short-circuit of battery.) The reason is because PPy is reduced to its electronically insulating state upon contacting with lithium metal [17]. However, future works of long-term battery cycling (more than 100 cycles) are still needed to further justify the stability of the redox-active separator.

The enhanced battery capacity is attributed to the redox-activity of the PAN@PPy nanofibers contained in the separator. Both electrospun PAN separator and commercial PP separator are conventional separators consisting of inert polymers. Thus, the battery capacity is only provided by the LFP cathode, as evidenced by the similar cathodic and anodic curves obtained in the cyclic voltammetry measurement for electrospun PAN separator and commercial PP separator (*see* Figure 5.11 b). However, the battery capacity can be provided by both the LFP cathode and the PPy polymer for a battery cell with redox-active separator, leading to the enhanced overall battery capacity (as shown in Figure 5.12). In the charging process, the PPy polymer is inserted by the PF_6^- anion via an oxidation reaction, resulting in the releasing of a Li^+ cation and an electron. In the discharging process, the PF_6^- is extracted reversibly from the PPy polymer chain, while the PPy is reduced to receive an electron [129, 193]. Therefore, the redox-active separator containing PAN@PPy nanofibers provides extra capacity to the LIB cell by the oxidation and reduction of PPy, which also contributes to the wide cathodic and anodic peaks obtained in the cyclic voltammograms.

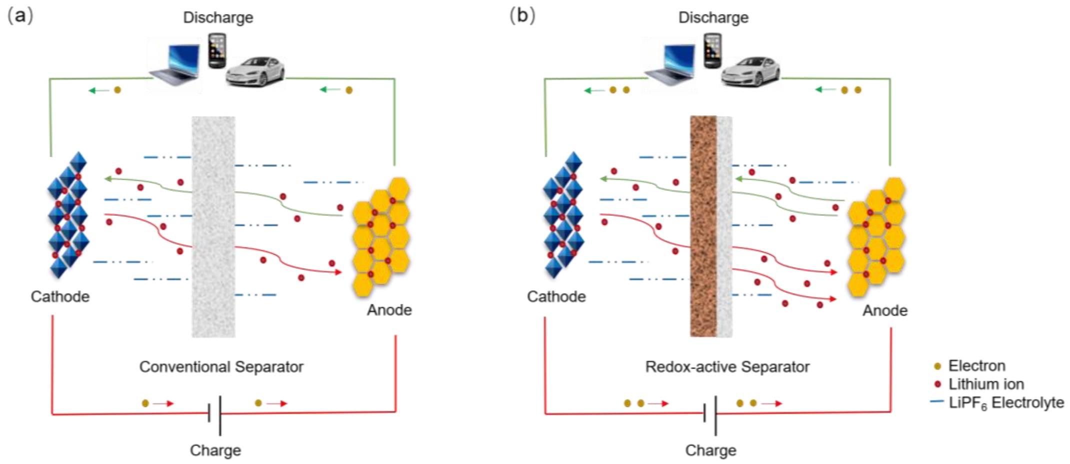

Cathode: $LiFePO_4 \underset{Discharge}{\overset{Charge}{\rightleftarrows}} Li_{1-x}FePO_4 + xLi^+ + xe^-$

Anode: $xLi^+ + xe^- + C \underset{Discharge}{\overset{Charge}{\rightleftarrows}} Li_xC$

Cathode: $LiFePO_4 \underset{Discharge}{\overset{Charge}{\rightleftarrows}} Li_{1-x}FePO_4 + xLi^+ + xe^-$

Redox-active separator: $PPy + LiPF_6 \underset{Discharge}{\overset{Charge}{\rightleftarrows}} [PPy^+]PF_6^- + Li^+ + e^-$

Anode: $(x+1)\,Li^+ + (x+1)\,e^- + C \underset{Discharge}{\overset{Charge}{\rightleftarrows}} Li_{x+1}C$

Figure 5.12. Schematic of the LFP/Li batteries containing (a) conventional separator and (b) redox-active separator

The exact discharge capacity provided by the redox-active separator at 0.2 C rate is determined as 0.117 mAh by calculating the difference of the discharge capacity between the cells containing redox-active separator and electrospun PAN separator. The capacity generated by the nanofibrous redox-active separator fabricated in this study is comparable to the capacity reported in literature (0.116 mAh) [17], in which the redox-active separator is fabricated by a vacuum filtration membrane making process (as introduced in Section 1.2). However, the specific capacity of the redox-active separator fabricated in this study (164.8 $mAh \cdot g^{-1}$) is greater than the prior art (105 $mAh \cdot g^{-1}$).

This advantage is attributed to the superior structural properties of the nanofibrous separator, as well as the doping of $Fe(CN)_6^{4-}$ into PPy polymer. The porosity, pore size and ionic conductivity of the redox-active separator in this study is 34.4%, 1150.6% and 93.8% higher than that of the separator reported in literature [17], which allows the retention of larger amount of liquid electrolyte and fluently migration of Li^+ ions. As a result, the discharge capacity of the redox-active separator fabricated in this study outperformed the one in the prior art. (The same reason also explains the 3.7 % higher of specific capacity of the LIB cell with electrospun PAN separator compared to commercial PP separator, as shown in Figure 5.11 a). In addition to the nano-structural advantage, the doping of $Fe(CN)_6^{4-}$ into PPy polymer also contributes to the enhanced capacity. First, the doping of $Fe(CN)_6^{4-}$ strongly improved the conductivity of the PPy skeleton by 3 orders of magnitude (*see* Section 4.4.4), leading to enhancing the kinetics of the PPy electrochemical process [193]. Second, the $Fe(CN)_6^{3-/4-}$ couple is electrochemically active with its redox potential close to the PPy. Thus, the reduction and oxidation of $Fe(CN)_6^{3-/4-}$, with its theoretical capacity of 90 $mAh \cdot g^{-1}$, also provides additional capacity during the battery cycling. In addition, the doped $Fe(CN)_6^{4-}$ anions can bridge the charge transfer between the PPy and the electrolyte by acting as an electron mediator [180].

Moreover, the specific capacity of the nanofibrous redox-active separator fabricated in this study (164.8 mAh·g^{-1}) is also comparable to that of the $Fe(CN)_6^{4-}$ doped PPy nanoparticles used directly as LIB cathode (145 mAh·g^{-1} [180]). The relatively higher (about 13.7%) specific capacity is owing to the lower charge/discharge current rate adopted in this study (the current rate is 34 mA·g^{-1} in this study, whereas it is 50 mA·g^{-1} in the compared literature [180]), as well as the structural advantage of the nanofibrous membrane as discussed in the preceding paragraph.

Table 5.3 compares the energy density of the LIB cells with different separators. The calculated gravimetric and volumetric energy density is normalized with respect to the total mass and volume of the cathode and separator, respectively. The redox-active separator fabricated in this study achieves the highest gravimetric energy density of 103.0 mAh·g^{-1}, which is 56.1% and 27.2% higher than the commercial PP separator and the redox-active separator reported in literature [17]. The reason is mainly attributed to the light weight of the electrospun separators. Therefore, the electrospun PAN separator, as a conventional separator, also obtains a high gravimetric energy density of 87.4 mAh·g^{-1}. However, the volumetric energy density of the redox-active separator fabricated in this study is still weaker than commercial PP separator, due to the much thicker thickness (2 times of the commercial separator) adopted in this study to ensure the durability of the battery testing. Thus, future works are needed to develop thin redox-active separator with sufficient mechanical strength, in order to achieve a greater volumetric energy density without sacrificing the battery durability (details are discussed in Section 6.2).

Table 5.3.Energy density of the LIB cells containing different separators

	Gravimetric energy density ($mAh \cdot g^{-1}$)	Volumetric energy density ($mAh \cdot cm^{-3}$)	Ref.
Commercial PP separator	66.0	64.1	This work
Electrospun PAN separator	87.4	37.2	This work
Redox-active separator	103.0	44.4	This work
Redox-active separator	81	-	[17]

5.4 Summary

The proposed nanofibrous redox-active separator is fabricated in this chapter based on electrospinning and *in-situ* polymerization. The fabricated separator is a bilayer membrane with the redox-active layer consisting PAN@PPy core-shell structured nanofibers, and the inert layer consisting PAN nanofibers. The PPy fiber shell with wall thickness of about 70 nm is doped by $Fe(CN)_6^{4-}$ anions. The chemical composition of the PPy fiber shell is determined as $PPy_{18.5}^{7+} \cdot (SO_4)_{1.5}^{3-} \cdot Fe(CN)_6^{4-}$ by element analysis obtained from XPS. The porosity and electrolyte uptake of the redox-active separator (79.3 ± 7.1% and 294.6 ± 31.5%) are slightly lower than that of the pristine electrospun PAN separator (85.7 ± 7.0% and 310.7 ± 32.2%), but greatly higher than the commercial PP separator (41% and 81.5 ± 17.4%). Similarly, the ionic conductivity of the redox-active separator (1.57 ± 0.06 $mS \cdot cm^{-1}$) and electrospun PAN separator (2.26 ± 0.09 $mS \cdot cm^{-1}$) are greater than that of commercial PP separator (0.75 ± 0.02 $mS \cdot cm^{-1}$). In addition, the redox-active separator is thermally stable up to 289 °C, and is capable of maintaining its dimensions at 160 °C. Moreover, the redox-active separator exhibits greater mechanical properties than the electrospun PAN separator, including 82.9% higher of yield strength (6.4±0.6 MPa); 187.3% higher of Young's modulus (70.1±14.1 MPa); and 13.0% higher of UTS (7.8±0.6 MPa).

The reason is that the PAN@PPy nanofibers in the redox-active separator have better mechanical properties than the pristine electrospun PAN nanofibers, due to the bonded fibers created by the forming of PPy fiber shells.

Finally, the redox-active separator, electrospun PAN separator and commercial PP separator are assembled into CR2032 coin LIB cells for performance evaluation. The battery cell containing redox-active separator exhibits the highest discharge capacity of 158.7-227.0 mAh·g^{-1} at different current rates of 2-0.2 C. The enhanced battery capacity is stemmed from the redox-activity of the PPy polymer, as evidenced by the wider cathodic and anodic peaks obtained from the cyclic voltammetry compared to the other two separators. In addition, the battery cell with redox-active separator achieves the highest gravimetric energy density of 103.0 mAh·g^{-1}, which is 56.1% higher than that of commercial PP separator.

Chapter 6 Conclusions and Future Works

6.1 Conclusions

This thesis develops a PPy based redox-active nanofibrous separator for LIB to enhance the battery capacity. The redox activity of the developed separator stems from the PPy polymer, which is integrated with the electrospun nanofibers by *in-situ* polymerization. Prior to fabricating the redox-active separator, a numerical modeling study is first carried out to quantitatively investigate the effect of a separator on the LIB performance. The results show that the separator thickness has strong effects on the battery energy density, as it drops from 148.8 to 110.6 Wh/kg when the separator thickness increases from 5 to 100 μm. Moreover, the mass transfer resistance increases with decreasing separator porosity, resulting in the increased electrolyte concentration gradient inside the battery separator. The correlation between the separator porosity and the electrolyte concentration gradient can be described by an exponential function, which indicates that separators should have an optimum porosity of 80% and that further increase in the separator porosity contributes little to the mass transfer. In addition, it is necessary to improve the thermal properties of the separator because of its great heat transfer resistance. Simultaneous increase in thermal conductivity to 1 W m^{-1} K^{-1} and heat capacity to 3500 J kg^{-1} K^{-1}, respectively, helps reduce the battery temperature rise by 1.3 K and temperature differences by 0.8 K.

Then, this thesis presents a kinetics study of the *in-situ* polymerization of PPy on electrospun PAN nanofibers. The *in-situ* polymerization is the method adopted to produce redox-active nanofibers. The polymerization mechanism for PPy based on the coupling of oxidized pyrrole oligomers and neutral pyrrole monomers is identified as suitable to understand this process. The reaction rate constant k_2 (between oxidized oligomers and neutral monomers) increases by 158.2-209.6% when the electrospun fibrous template is added, because considerable amount of reaction sites is created in the *in-situ* polymerization process due to the large surface area of electrospun fibers presented in the reaction bath. This explanation is further confirmed by the 37.7% higher activation entropy of the *in-situ* polymerization process compared to the polymerization without template. Adding electrospun fibrous template into the *in-situ* polymerization bath increases the available reaction sites between reactants, leading to the increase of overall disorder of the reaction process.

The PPy based redox-active separator is subsequently fabricated and characterized. The fabricated separator is a bilayer membrane with the redox-active layer consisting PAN@PPy core-shell structured nanofibers, and the inert layer consisting PAN nanofibers. The porosity, electrolyte uptake, and ionic conductivity of the redox-active separator (79.3 ± 7.1%, 294.6 ± 31.5% and 1.57 ± 0.06 mS·cm^{-1}, respectively) are higher than that of commercial PP separator (41%, 81.5 ± 17.4% and 0.75 ± 0.02 mS·cm^{-1}, respectively). In addition, the redox-active separator is thermally stable up to 289 °C, and is capable of maintaining its dimensions at 160 °C. Moreover, the redox-active separator exhibits mechanical properties including a yield strength of 6.4±0.6 MPa, Young's modulus of 70.1 ±14.1 MPa, and UTS of 7.8±0.6 MPa.

Finally, the redox-active separator, electrospun PAN separator and commercial PP separator are assembled into LIB coin cells for performance evaluation. The battery cell containing redox-active separator exhibits the highest discharge capacity of 158.7-227.0 mAh·g-1 at different current rates of 2-0.2 C. The enhanced battery capacity is stemmed from the redox-activity of the PPy polymer contained in the redox-active separator, as evidenced by the wider cathodic and anodic peaks obtained from the cyclic voltammetry compared to the other two separators. In addition, the battery cell with redox-active separator achieves the highest gravimetric energy density of 103.0 mAh·g-1, which is 56.1% higher than the commercial PP separator. The results in this thesis suggest a promising strategy to enhance the capacity of LIBs by merely changing the conventional separators into nanofibrous redox-active separators.

6.2 Recommended future works

The following recommendations are suggested for future research works based on the studies in this thesis.

(1) **Optimization of the redox-active separator.** Battery modeling can assistant the optimization of the design parameter of the battery separator. The numerical model developed in Chapter 3 is capable of simulating the LIB performance with various separator structure. Future works can devote to expand this model to simulate LIB with redox-active separator. Additional experimental works are needed to determine the electrochemical properties of the PPy polymer, *e.g.*, its open circuit potential at different state of charge, in order to calculate its electrochemical kinetics. Then, the redox-active separator can be added into the model domain as a bilayer component between the cathode and anode. The redox-active layer can be considered in the model as an "addition cathode" to participate in the charge conservation and mass conservation. Eventually, the design parameter of the redox-active separator, including porosity, layer thickness, and PPy loading, can be optimized.

(2) **Improving the mechanical strength of electrospun separator.** There is a need to improve the mechanical strength of the redox-active separator developed in this study. Although the gravimetric energy density of the redox-active separator outperforms that of commercial separator (as shown in Section 5.3.4), the volumetric energy density is still its drawback. This is because a thicker redox-active separator is used in battery cell to compensate its weak mechanical strength. Therefore, the volumetric energy density could be strongly enhanced, once a thin redox-active separator with sufficient mechanical strength is available.

A feasible approach is to change the PAN nanofibers used in this study to another type of electrospun nanofibers with greater mechanical properties. A handful of research works have demonstrated the production of strong electrospun nanofibers with UTS as high as above 20 MPa (as shown in Figure 5.10), which is more than 3 times of the strength of the PAN (6.9±0.4 MPa) nanofibers used in this study. Thus, the mechanical strength of the redox-active separator can be immediately improved by adopting mechanically stronger electrospun nanofibers as its skeleton.

Another approach is to create bindings between all the electrospun nanofibers. Lacking inter-fiber bindings is a main factor causes the weak mechanical properties of electrospun membrane. As an example, the mechanical properties of electrospun PAN membrane are improved by in-situ polymerization of PPy because it results in the bindings of some adjacent fibers (as discussed in Section 5.3.3). However, not all the fibers are bonded together in this study. Thus, future works can devote to explore methods that can bind all the electrospun fibers together. In addition, it is of interest to quantitatively study the relationship between the mechanical strength of an electrospun membrane and the proportion of bonded fibers it contains.

In addition to the tensile strength, future works could also study other mechanical properties of the fabricated separator including compression strength and puncture strength. Those mechanical properties are deemed essential for a comprehensive understanding of the mechanical performance of a separator.

(3) **Enhancing the PPy loading on the redox-active separator.** The redox activity of the fabricated separator in this study is stemmed from the integrated PPy polymer. Thus, increasing the PPy loading on the redox-active separator could further enhance the capacity of the LIB cell. Chapter 5 demonstrates the fabrication of PPy based core-shell structured nanofibrous separator using *in-situ* polymerization, in which the PPy shell adheres on the surface of the core fiber. Thus, increase the surface area of the core fiber is possible to

further enhance its PPy loading.

A feasible approach is to fabricate electrospun nanofibers with intra porous structure and use it as core fibers for PPy *in-situ* polymerization. The surface area of the intra porous electrospun nanofibers can be dramatically increased since the pores are introduced into the fiber surface [194]. Available methods to produce such electrospun nanofibers including non-solvent induced phase separation [44], thermal-induced phase separation [195], and selective removal of a sacrificial phase [196].

(4) **Investigation of the thermal properties of redox-active separator.** The thermal properties, including thermal conductivity and heat capacity, of a separator have a strong effect on the heat dissipation of a LIB (as discussed in Section 3.3.4). However, this thesis only focused on the electrochemical performance of the fabricated redox-active separator. The thermal properties of the separator are not studied due to the limited time of a PhD research. Thus, future works can be carried out to further investigate the thermal effect of the redox-active separator on LIBs, as well as developing composite separators to further improve the battery's heat dissipation.

(5) **Narrowing down the pore size distribution of the fabricated separator.** The pore size of the nanofibrous separators fabricated in this study has a relatively broad distribution. Thus, the maximum pore size of the redox-active separator exceeds 1 um as shown in Figure 5.5, which may raise concerns for battery self-discharging. Therefore, it is necessary to narrow down the pore size distribution of the separator, in order to prevent the battery self-discharging and improve the long-term stability of battery operation.

The precise control of the electrospinning process could result in narrowing down the pore size distribution of the fabricated separator. Future works could focus on the precise control of the environmental parameters of the electrospinning, *e.g.* temperature and humidity, which are not controlled in the present thesis.

(6) **Further investigating the kinetics of PPy in-situ polymerization.** The kinetics of

PPy polymerization is enhanced when adding electrospun nanofibrous membrane as template for in-situ polymerization as shown in Section 4.4.2. The reason for this enhancement is explained by the increased reaction sites in this thesis. However, the decreasing of diffusion distance may also attribute to this. Since the electrospun membrane has a 3D fibrous structure, the possibility of the reactants meeting each other is increased when they are trapped inside the membrane structure compared to the situation when the membrane is absent (in which the reactions are mostly taking place on the bottom of the reaction container because of the aggregation of PPy clusters). However, future experimental works are needed for further investigation. For instance, electrospun membranes with different porosity, packing density, and pore size could be fabricated and implemented for PPy *in-situ* polymerization to justify the effect of diffusion distance on the reaction kinetics.

Copyright Permissions

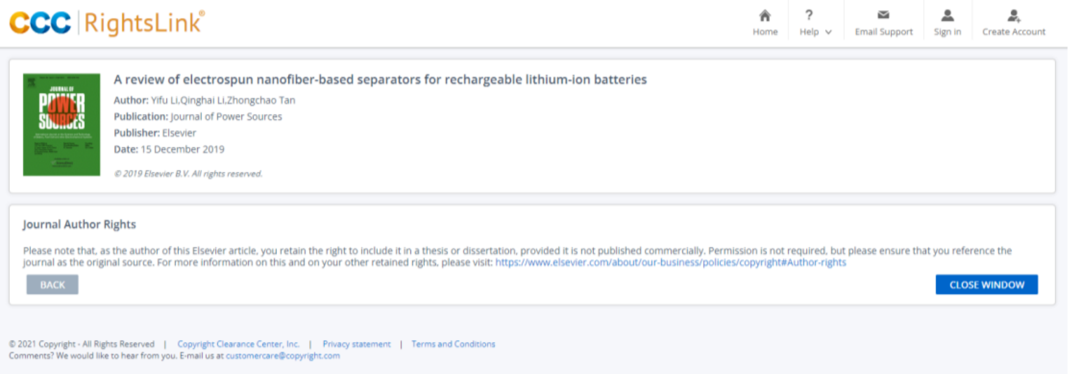

A review of electrospun nanofiber-based separators for rechargeable lithium-ion batteries

Author: Yifu Li,Qinghai Li,Zhongchao Tan
Publication: Journal of Power Sources
Publisher: Elsevier
Date: 15 December 2019

© 2019 Elsevier B.V. All rights reserved.

Journal Author Rights

Please note that, as the author of this Elsevier article, you retain the right to include it in a thesis or dissertation, provided it is not published commercially. Permission is not required, but please ensure that you reference the journal as the original source. For more information on this and on your other retained rights, please visit: https://www.elsevier.com/about/our-business/policies/copyright#Author-rights

© 2021 Copyright - All Rights Reserved | Copyright Clearance Center, Inc. | Privacy statement | Terms and Conditions
Comments? We would like to hear from you. E-mail us at customercare@copyright.com

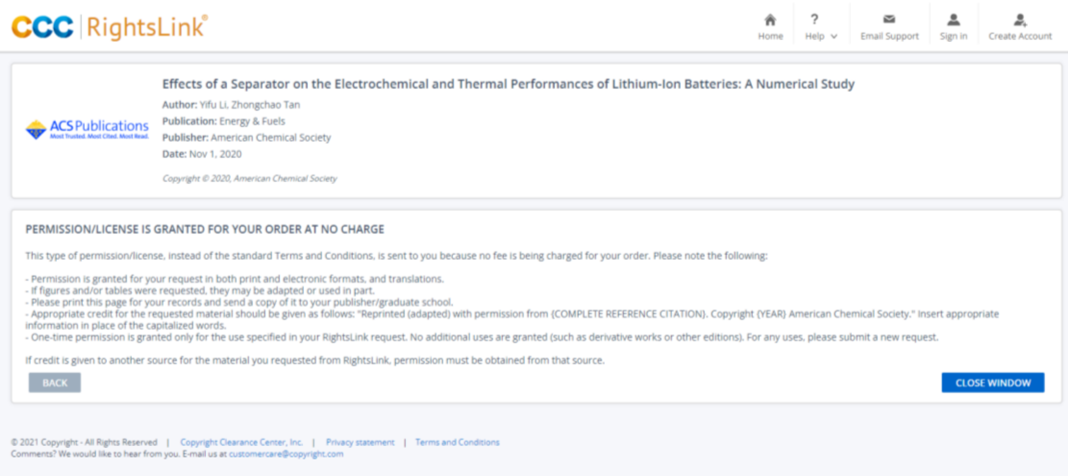

Effects of a Separator on the Electrochemical and Thermal Performances of Lithium-Ion Batteries: A Numerical Study

Author: Yifu Li, Zhongchao Tan
Publication: Energy & Fuels
Publisher: American Chemical Society
Date: Nov 1, 2020

Copyright © 2020, American Chemical Society

PERMISSION/LICENSE IS GRANTED FOR YOUR ORDER AT NO CHARGE

This type of permission/license, instead of the standard Terms and Conditions, is sent to you because no fee is being charged for your order. Please note the following:

- Permission is granted for your request in both print and electronic formats, and translations.
- If figures and/or tables were requested, they may be adapted or used in part.
- Please print this page for your records and send a copy of it to your publisher/graduate school.
- Appropriate credit for the requested material should be given as follows: "Reprinted (adapted) with permission from {COMPLETE REFERENCE CITATION}. Copyright {YEAR} American Chemical Society." Insert appropriate information in place of the capitalized words.
- One-time permission is granted only for the use specified in your RightsLink request. No additional uses are granted (such as derivative works or other editions). For any uses, please submit a new request.

If credit is given to another source for the material you requested from RightsLink, permission must be obtained from that source.

© 2021 Copyright - All Rights Reserved | Copyright Clearance Center, Inc. | Privacy statement | Terms and Conditions
Comments? We would like to hear from you. E-mail us at customercare@copyright.com

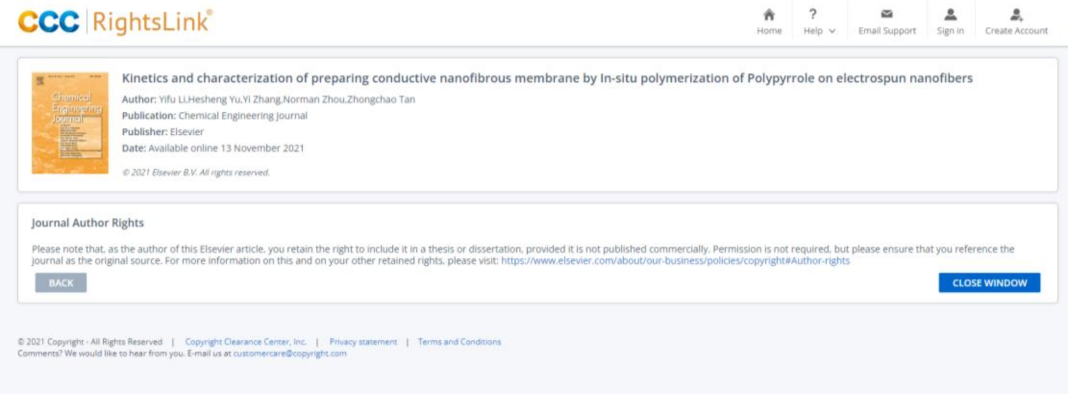

Kinetics and characterization of preparing conductive nanofibrous membrane by In-situ polymerization of Polypyrrole on electrospun nanofibers

Author: Yifu Li,Hesheng Yu,Yi Zhang,Norman Zhou,Zhongchao Tan
Publication: Chemical Engineering Journal
Publisher: Elsevier
Date: Available online 13 November 2021

© 2021 Elsevier B.V. All rights reserved.

Journal Author Rights

Please note that, as the author of this Elsevier article, you retain the right to include it in a thesis or dissertation, provided it is not published commercially. Permission is not required, but please ensure that you reference the journal as the original source. For more information on this and on your other retained rights, please visit: https://www.elsevier.com/about/our-business/policies/copyright#Author-rights

© 2021 Copyright - All Rights Reserved | Copyright Clearance Center, Inc. | Privacy statement | Terms and Conditions
Comments? We would like to hear from you. E-mail us at customercare@copyright.com

References

[1] J. Sheng, S. Tong, Z. He, R. Yang, Recent developments of cellulose materials for lithium-ion battery separators, Cellulose, 24 (2017) 4103-4122.

[2] P. Alotto, M. Guarnieri, F. Moro, Redox flow batteries for the storage of renewable energy: A review, Renewable and Sustainable Energy Reviews, 29 (2014) 325-335.

[3] T.O. Sistrunk, John Frederic Daniell, Journal of Chemical Education, 29 (1952) 26.

[4] P. Kurzweil, Gaston Planté and his invention of the lead–acid battery—The genesis of the first practical rechargeable battery, Journal of Power Sources, 195 (2010) 4424-4434.

[5] W.I.F.D. M.M.Thackeray, P.G.Bruce, J.B.Goodenough, Lithium insertion into manganese spinels, Materials Research Bulletin, 18 (1983) 461-472

[6] S.J.R. Agarwal R.R., Stagewise electrochemical intercalation of lithium in graphite by means of a molten salt cell. , Electrochemical Society, (1985).

[7] H. Lee, M. Yanilmaz, O. Toprakci, K. Fu, X. Zhang, A review of recent developments in membrane separators for rechargeable lithium-ion batteries, Energy Environ. Sci., 7 (2014) 3857-3886.

[8] Y. Li, Z. Tan, Effects of a Separator on the Electrochemical and Thermal Performances of Lithium-Ion Batteries: A Numerical Study, Energy & Fuels, 34 (2020) 14915-14923.

[9] V. Deimede, C. Elmasides, Separators for Lithium-Ion Batteries: A Review on the Production Processes and Recent Developments, Energy Technology, 3 (2015) 453-468.

[10] C.T. Love, Thermomechanical analysis and durability of commercial micro-porous polymer Li-ion battery separators, Journal of Power Sources, 196 (2011) 2905-2912.

[11] D. Djian, F. Alloin, S. Martinet, H. Lignier, J.Y. Sanchez, Lithium-ion batteries with high charge rate capacity: Influence of the porous separator, Journal of Power Sources, 172

(2007) 416-421.

[12] Z. Li, J.-w. Zhang, L.-g. Yu, J.-w. Zhang, Electrospun porous nanofibers for electrochemical energy storage, Journal of Materials Science, 52 (2017) 6173-6195.

[13] J.-W. Jung, C.-L. Lee, S. Yu, I.-D. Kim, Electrospun nanofibers as a platform for advanced secondary batteries: a comprehensive review, Journal of Materials Chemistry A, 4 (2016) 703-750.

[14] J. Zucker, Melt blown battery separator, in, Daramic LLC U.S., 2004.

[15] W. Yi, Z. Huaiyu, H. Jian, L. Yun, Z. Shushu, Wet-laid non-woven fabric for separator of lithium-ion battery, Journal of Power Sources, 189 (2009) 616-619.

[16] T.-H. Cho, M. Tanaka, H. Ohnishi, Y. Kondo, M. Yoshikazu, T. Nakamura, T. Sakai, Composite nonwoven separator for lithium-ion battery: Development and characterization, Journal of Power Sources, 195 (2010) 4272-4277.

[17] Z. Wang, R. Pan, C. Ruan, K. Edstrom, M. Stromme, L. Nyholm, Redox-Active Separators for Lithium-Ion Batteries, Advanced science, 5 (2018) 1700663.

[18] J. Li, W. Tian, H. Yan, L. He, X. Tuo, Preparation and performance of aramid nanofiber membrane for separator of lithium ion battery, Journal of Applied Polymer Science, 133 (2016).

[19] Y. Xiang, J. Li, J. Lei, D. Liu, Z. Xie, D. Qu, K. Li, T. Deng, H. Tang, Advanced Separators for Lithium-Ion and Lithium-Sulfur Batteries: A Review of Recent Progress, ChemSusChem, 9 (2016) 3023-3039.

[20] Q. Liu, J. Zhu, L. Zhang, Y. Qiu, Recent advances in energy materials by electrospinning, Renewable and Sustainable Energy Reviews, 81 (2018) 1825-1858.

[21] C.J. Ellison, A. Phatak, D.W. Giles, C.W. Macosko, F.S. Bates, Melt blown nanofibers: Fiber diameter distributions and onset of fiber breakup, Polymer, 48 (2007) 3306-3316.

[22] A. Safavi, S. Fathi, M.R. Babaei, Z. Mansoori, M. Latifi, Experimental and numerical analysis of fiber characteristics effects on fiber dispersion for wet-laid nonwoven, Fibers and Polymers, 10 (2009) 231-236.

[23] L. Zhang, W. Batchelor, S. Varanasi, T. Tsuzuki, X. Wang, Effect of cellulose nanofiber dimensions on sheet forming through filtration, Cellulose, 19 (2012) 561-574.

[24] X. Huang, Performance evaluation of a non-woven lithium ion battery separator prepared through a paper-making process, Journal of Power Sources, 256 (2014) 96-101.

[25] J. Yoon, H.S. Yang, B.S. Lee, W.R. Yu, Recent Progress in Coaxial Electrospinning: New Parameters, Various Structures, and Wide Applications, Adv Mater, 30 (2018) e1704765.

[26] H. Zhang, C.-E. Lin, M.-Y. Zhou, A.E. John, B.-K. Zhu, High thermal resistance polyimide separators prepared via soluble precusor and non-solvent induced phase separation process for lithium ion batteries, Electrochimica Acta, 187 (2016) 125-133.

[27] F. Zhang, X. Ma, C. Cao, J. Li, Y. Zhu, Poly(vinylidene fluoride)/SiO2 composite membranes prepared by electrospinning and their excellent properties for nonwoven separators for lithium-ion batteries, Journal of Power Sources, 251 (2014) 423-431.

[28] M. Yanilmaz, Y. Lu, J. Zhu, X. Zhang, Silica/polyacrylonitrile hybrid nanofiber membrane separators via sol-gel and electrospinning techniques for lithium-ion batteries, Journal of Power Sources, 313 (2016) 205-212.

[29] L. Rayleigh, On the equilibrium of liquid conducting masses charged with electricity, The London, Edinburgh, and Dublin Philosophical Magazine and Journal of Science, 14 (1882) 184-186.

[30] F.R.S. Geoffrey Taylor, Disintegration of water drops in an electric field, Proceedings of the Royal Society of London. Series A. Mathematical and Physical Sciences, 280 (1964) 383.

[31] M.J. Laudenslager, W.M. Sigmund, Electrospinning, in: B. Bhushan (Ed.) Encyclopedia of Nanotechnology, Springer Netherlands, Dordrecht, 2012, pp. 769-775.

[32] W. Chen, Y. Liu, Y. Ma, J. Liu, X. Liu, Improved performance of PVdF-HFP/PI nanofiber membrane for lithium ion battery separator prepared by a bicomponent cross-electrospinning method, Materials Letters, 133 (2014) 67-70.

[33] F. Huang, Y. Xu, B. Peng, Y. Su, F. Jiang, Y.-L. Hsieh, Q. Wei, Coaxial Electrospun Cellulose-Core Fluoropolymer-Shell Fibrous Membrane from Recycled Cigarette Filter as Separator for High Performance Lithium-Ion Battery, ACS Sustainable Chemistry & Engineering, 3 (2015) 932-940.

[34] F. Huang, W. Liu, P. Li, J. Ning, Q. Wei, Electrochemical Properties of LLTO/Fluoropolymer-Shell Cellulose-Core Fibrous Membrane for Separator of High Performance Lithium-Ion Battery, Materials, 9 (2016).

[35] L. Persano, A. Camposeo, C. Tekmen, D. Pisignano, Industrial Upscaling of Electrospinning and Applications of Polymer Nanofibers: A Review, Macromolecular Materials and Engineering, 298 (2013) 504-520.

[36] C.J.J. Angammana, S H, The Effects of Electric Field on the Multijet Electrospinning Process and Fiber Morphology, IEEE Transactions on Industry Applications, 47 (2011) 1028-1035.

[37] Y.M.S.M.M.H.M.P.B. G.C.Rutledge, Experimental characterization of electrospinning the electrically forced jet and instabilities, Polymer, 42 (2001) 09955-09967.

[38] A.L. Yarin, E. Zussman, Upward needleless electrospinning of multiple nanofibers, Polymer, 45 (2004) 2977-2980.

[39] F.S. Oldrich Jirsak, David Lukas, Vaclav Kotek, Lenka Martinova, Jiri Chaloupek A method of nanofibres production from a polymer solution using electrostatic spinning and a device for carrying out the method, in: W.I.p. organization (Ed.), 2005.

[40] H. Niu, X. Wang, T. Lin, Needleless electrospinning: influences of fibre generator geometry, Journal of the Textile Institute, 103 (2012) 787-794.

[41] X. Wang, H. Niu, X. Wang, T. Lin, Needleless Electrospinning of Uniform Nanofibers Using Spiral Coil Spinnerets, Journal of Nanomaterials, 2012 (2012) 1-9.

[42] O. Jirsak, P. Sysel, F. Sanetrnik, J. Hruza, J. Chaloupek, Polyamic Acid Nanofibers Produced by Needleless Electrospinning, Journal of Nanomaterials, 2010 (2010) 1-6.

[43] Y. Li, Q. Li, Z. Tan, A review of electrospun nanofiber-based separators for rechargeable lithium-ion batteries, Journal of Power Sources, 443 (2019) 227262.

[44] X. Yu, H. Xiang, Y. Long, N. Zhao, X. Zhang, J. Xu, Preparation of porous polyacrylonitrile fibers by electrospinning a ternary system of PAN/DMF/H2O, Materials Letters, 64 (2010) 2407-2409.

[45] S.-S. Choi, Y.S. Lee, C.W. Joo, S.G. Lee, J.K. Park, K.-S. Han, Electrospun PVDF nanofiber web as polymer electrolyte or separator, Electrochimica Acta, 50 (2004) 339-343.

[46] K. Gao, X. Hu, C. Dai, T. Yi, Crystal structures of electrospun PVDF membranes and its separator application for rechargeable lithium metal cells, Materials Science and Engineering: B, 131 (2006) 100-105.

[47] K. Hwang, B. Kwon, H. Byun, Preparation of PVdF nanofiber membranes by electrospinning and their use as secondary battery separators, Journal of Membrane Science, 378 (2011) 111-116.

[48] Cuiru Yang, Zhidong Jia, Zhicheng Guana, L. Wang, Polyvinylidene fluoride membrane by novel electrospinning system for separator of Li-ion batteries, Journal of Power Sources, 189 (2009) 716-720.

[49] T. Evans, J.-H. Lee, V. Bhat, S.-H. Lee, Electrospun polyacrylonitrile microfiber separators for ionic liquid electrolytes in Li-ion batteries, Journal of Power Sources, 292 (2015) 1-6.

[50] X. Ma, P. Kolla, R. Yang, Z. Wang, Y. Zhao, A.L. Smirnova, H. Fong, Electrospun polyacrylonitrile nanofibrous membranes with varied fiber diameters and different membrane porosities as lithium-ion battery separators, Electrochimica Acta, 236 (2017) 417-423.

[51] N. Sabetzadeh, A.A. Gharehaghaji, M. Javanbakht, Porous PAN micro/nanofiber separators for enhanced lithium-ion battery performance, Solid State Ionics, 325 (2018) 251-257.

[52] L. Cao, P. An, Z. Xu, J. Huang, Performance evaluation of electrospun polyimide non-woven separators for high power lithium-ion batteries, Journal of Electroanalytical Chemistry, 767 (2016) 34-39.

[53] W. Jiang, Z. Liu, Q. Kong, J. Yao, C. Zhang, P. Han, G. Cui, A high temperature operating nanofibrous polyimide separator in Li-ion battery, Solid State Ionics, 232 (2013) 44-48.

[54] Y.-E. Miao, G.-N. Zhu, H. Hou, Y.-Y. Xia, T. Liu, Electrospun polyimide nanofiber-based nonwoven separators for lithium-ion batteries, Journal of Power Sources, 226 (2013) 82-86.

[55] L. Kong, Y. Yan, Z. Qiu, Z. Zhou, J. Hu, Robust fluorinated polyimide nanofibers membrane for high-performance lithium-ion batteries, Journal of Membrane Science, 549 (2018) 321-331.

[56] Y. Ding, H. Hou, Y. Zhao, Z. Zhu, H. Fong, Electrospun polyimide nanofibers and their applications, Progress in Polymer Science, 61 (2016) 67-103.

[57] B. Jung，, J. K.Yoon, B. Kim, H.W. Rhee, Effect of crystallization and annealing on polyacrylonitrile membranes for ultrafiltration, Journal of Membrane Science, 246 (2005) 67-76.

[58] X. Huang, Separator technologies for lithium-ion batteries, Journal of Solid State

Electrochemistry, 15 (2010) 649-662.

[59] T.-H. Cho, M. Tanaka, H. Onishi, Y. Kondo, T. Nakamura, H. Yamazaki, S. Tanase, T. Sakai, Battery performances and thermal stability of polyacrylonitrile nano-fiber-based nonwoven separators for Li-ion battery, Journal of Power Sources, 181 (2008) 155-160.

[60] D.B. Xiaosong Huang, Xinran Xiao, A multilayer composite separator consisting of non-woven mats and ceramic particles for use in lithium ion batteries, Journal of Solid State Electrochemistry, 18 (2014) 133-139.

[61] H. Li, B. Zhang, W. Liu, B. Lin, Q. Ou, H. Wang, M. Fang, D. Liu, S. Neelakandan, L. Wang, Effects of an electrospun fluorinated poly(ether ether ketone) separator on the enhanced safety and electrochemical properties of lithium ion batteries, Electrochimica Acta, 290 (2018) 150-164.

[62] H. Li, B. Zhang, B. Lin, Y. Yang, Y. Zhao, L. Wang, Electrospun Poly(ether ether ketone) Nanofibrous Separator with Superior Performance for Lithium-Ion Batteries, Journal of The Electrochemical Society, 165 (2018) A939-A946.

[63] Z. Li, W. Wang, Y. Han, L. Zhang, S. Li, B. Tang, S. Xu, Z. Xu, Ether modified poly(ether ether ketone) nonwoven membrane with excellent wettability and stability as a lithium ion battery separator, Journal of Power Sources, 378 (2018) 176-183.

[64] W. Qi, C. Lu, P. Chen, L. Han, Q. Yu, R. Xu, Electrochemical performances and thermal properties of electrospun Poly(phthalazinone ether sulfone ketone) membrane for lithium-ion battery, Materials Letters, 66 (2012) 239-241.

[65] C. Shi, J. Zhu, X. Shen, F. Chen, F. Ning, H. Zhang, Y.-Z. Long, X. Ning, J. Zhao, Flexible inorganic membranes used as a high thermal safety separator for the lithium-ion battery, RSC Advances, 8 (2018) 4072-4077.

[66] C. Shi, P. Zhang, S. Huang, X. He, P. Yang, D. Wu, D. Sun, J. Zhao, Functional separator consisted of polyimide nonwoven fabrics and polyethylene coating layer for

lithium-ion batteries, Journal of Power Sources, 298 (2015) 158-165.

[67] J. Li, Q. Zhong, Y. Yao, S. Bi, T. Zhou, X. Guo, M. Wu, T. Feng, R. Xiang, Electrochemical performance and thermal stability of the electrospun PTFE nanofiber separator for lithium-ion batteries, Journal of Applied Polymer Science, 135 (2018) 46508.

[68] Y. Liang, S. Cheng, J. Zhao, C. Zhang, S. Sun, N. Zhou, Y. Qiu, X. Zhang, Heat treatment of electrospun Polyvinylidene fluoride fibrous membrane separators for rechargeable lithium-ion batteries, Journal of Power Sources, 240 (2013) 204-211.

[69] L. Kong, B. Liu, J. Ding, X. Yan, G. Tian, S. Qi, D. Wu, Robust polyetherimide fibrous membrane with crosslinked topographies fabricated via in-situ micro-melting and its application as superior Lithium-ion battery separator with shutdown function, Journal of Membrane Science, 549 (2018) 244-250.

[70] Y. Zhai, N. Wang, X. Mao, Y. Si, J. Yu, S.S. Al-Deyab, M. El-Newehy, B. Ding, Sandwich-structured PVdF/PMIA/PVdF nanofibrous separators with robust mechanical strength and thermal stability for lithium ion batteries, J. Mater. Chem. A, 2 (2014) 14511-14518.

[71] J. Liu, Y. Liu, W. Yang, Q. Ren, F. Li, Z. Huang, Lithium ion battery separator with high performance and high safety enabled by tri-layered SiO 2 @PI/m-PE/SiO 2 @PI nanofiber composite membrane, Journal of Power Sources, 396 (2018) 265-275.

[72] C. Zhu, T. Nagaishi, J. Shi, H. Lee, P.Y. Wong, J. Sui, K. Hyodo, I.S. Kim, Enhanced Wettability and Thermal Stability of a Novel Polyethylene Terephthalate-Based Poly(Vinylidene Fluoride) Nanofiber Hybrid Membrane for the Separator of Lithium-Ion Batteries, ACS applied materials & interfaces, 9 (2017) 26400-26406.

[73] D. Wu, C. Shi, S. Huang, X. Qiu, H. Wang, Z. Zhan, P. Zhang, J. Zhao, D. Sun, L. Lin, Electrospun Nanofibers for Sandwiched Polyimide/Poly (vinylidene fluoride)/Polyimide Separators with the Thermal Shutdown Function, Electrochimica Acta, 176 (2015) 727-734.

[74] N. Angulakshmi, A.M. Stephan, Electrospun Trilayer Polymeric Membranes as Separator for Lithium–ion Batteries, Electrochimica Acta, 127 (2014) 167-172.

[75] T.J.R. Bin Wang, Guoying Chen, Electroactive Polymer Fiber Separators for Stable and Reversible Overcharge Protection in Rechargeable Lithium Batteries, Journal of The Electrochemical Society, 161 (2014) A1039-A1044.

[76] Y.-S. Oh, G.Y. Jung, J.-H. Kim, J.-H. Kim, S.H. Kim, S.K. Kwak, S.-Y. Lee, Janus-Faced, Dual-Conductive/Chemically Active Battery Separator Membranes, Advanced Functional Materials, 26 (2016) 7074-7083.

[77] K. Peng, B. Wang, C. Ji, A poly(ethylene terephthalate) nonwoven sandwiched electrospun polysulfonamide fibrous separator for rechargeable lithium ion batteries, Journal of Applied Polymer Science, 134 (2017).

[78] D. Li, D. Shi, Z. Yuan, K. Feng, H. Zhang, X. Li, A low cost shutdown sandwich-like composite membrane with superior thermo-stability for lithium-ion battery, Journal of Membrane Science, 542 (2017) 1-7.

[79] J.M. Kim, J.H. Park, C.K. Lee, S.Y. Lee, Multifunctional semi-interpenetrating polymer network-nanoencapsulated cathode materials for high-performance lithium-ion batteries, Scientific reports, 4 (2014) 4602.

[80] S. Wu, F. Li, R. Xu, S. Wei, G. Li, Synthesis of thiol-functionalized MCM-41 mesoporous silicas and its application in Cu(II), Pb(II), Ag(I), and Cr(III) removal, Journal of Nanoparticle Research, 12 (2009) 2111-2124.

[81] J. Zhang, Z. Liu, Q. Kong, C. Zhang, S. Pang, L. Yue, X. Wang, J. Yao, G. Cui, Renewable and superior thermal-resistant cellulose-based composite nonwoven as lithium-ion battery separator, ACS applied materials & interfaces, 5 (2013) 128-134.

[82] C. Cao, L. Tan, W. Liu, J. Ma, L. Li, Polydopamine coated electrospun poly(vinyldiene fluoride) nanofibrous membrane as separator for lithium-ion batteries, Journal of Power

Sources, 248 (2014) 224-229.

[83] C. Shi, J. Dai, S. Huang, C. Li, X. Shen, P. Zhang, D. Wu, D. Sun, J. Zhao, A simple method to prepare a polydopamine modified core-shell structure composite separator for application in high-safety lithium-ion batteries, Journal of Membrane Science, 518 (2016) 168-177.

[84] X. Liang, Y. Yang, X. Jin, J. Cheng, Polyethylene Oxide-Coated Electrospun Polyimide Fibrous Seperator for High-Performance Lithium-Ion Battery, Journal of Materials Science & Technology, 32 (2016) 200-206.

[85] J. Fan, On the discharge capability and its limiting factors of commercial 18650 Li-ion cell at low temperatures, Journal of Power Sources, 117 (2003) 170-178.

[86] Y. Zhai, K. Xiao, J. Yu, B. Ding, Fabrication of hierarchical structured SiO 2 /polyetherimide-polyurethane nanofibrous separators with high performance for lithium ion batteries, Electrochimica Acta, 154 (2015) 219-226.

[87] W. Ye, J. Zhu, X. Liao, S. Jiang, Y. Li, H. Fang, H. Hou, Hierarchical three-dimensional micro/nano-architecture of polyaniline nanowires wrapped-on polyimide nanofibers for high performance lithium-ion battery separators, Journal of Power Sources, 299 (2015) 417-424.

[88] X. Liang, Y. Yang, X. Jin, Z. Huang, F. Kang, The high performances of SiO 2 /Al 2 O 3 -coated electrospun polyimide fibrous separator for lithium-ion battery, Journal of Membrane Science, 493 (2015) 1-7.

[89] S.-R. Park, Y.-C. Jung, W.-K. Shin, K.H. Ahn, C.H. Lee, D.-W. Kim, Cross-linked fibrous composite separator for high performance lithium-ion batteries with enhanced safety, Journal of Membrane Science, 527 (2017) 129-136.

[90] X. Shen, C. Li, C. Shi, C. Yang, L. Deng, W. Zhang, L. Peng, J. Dai, D. Wu, P. Zhang, J. Zhao, Core-shell structured ceramic nonwoven separators by atomic layer deposition for

safe lithium-ion batteries, Applied Surface Science, 441 (2018) 165-173.

[91] K. Xiao, Y. Zhai, J. Yu, B. Ding, Nanonet-structured poly(m-phenylene isophthalamide)–polyurethane membranes with enhanced thermostability and wettability for high power lithium ion batteries, RSC Advances, 5 (2015) 55478-55485.

[92] M. Zhao, J. Wang, C. Chong, X. Yu, L. Wang, Z. Shi, An electrospun lignin/polyacrylonitrile nonwoven composite separator with high porosity and thermal stability for lithium-ion batteries, RSC Advances, 5 (2015) 101115-101120.

[93] F. Croce, R. Curini, A. Martinelli, L. Persi, F. Ronci, B. Scrosati, R. Caminiti, Physical and Chemical Properties of Nanocomposite Polymer Electrolytes, The Journal of Physical Chemistry B, 103 (1999) 10632-10638.

[94] L. Zhou, Q. Cao, B. Jing, X. Wang, X. Tang, N. Wu, Study of a novel porous gel polymer electrolyte based on thermoplastic polyurethane/poly(vinylidene fluoride-co-hexafluoropropylene) by electrospinning technique, Journal of Power Sources, 263 (2014) 118-124.

[95] W. Chen, Y. Liu, Y. Ma, W. Yang, Improved performance of lithium ion battery separator enabled by co-electrospinnig polyimide/poly(vinylidene fluoride-co-hexafluoropropylene) and the incorporation of TiO 2 -(2-hydroxyethyl methacrylate), Journal of Power Sources, 273 (2015) 1127-1135.

[96] G. Zainab, X. Wang, J. Yu, Y. Zhai, A. Ahmed Babar, K. Xiao, B. Ding, Electrospun polyacrylonitrile/polyurethane composite nanofibrous separator with electrochemical performance for high power lithium ion batteries, Materials Chemistry and Physics, 182 (2016) 308-314.

[97] X. Zhou, L. Yue, J. Zhang, Q. Kong, Z. Liu, J. Yao, G. Cui, A Core-Shell Structured Polysulfonamide-Based Composite Nonwoven Towards High Power Lithium Ion Battery Separator, Journal of The Electrochemical Society, 160 (2013) A1341-A1347.

[98] W.J. Zhihong Liu, Qingshan Kong, Chuanjian Zhang, Pengxian Han, Xuejiang Wang, Jianhua Yao, Guanglei Cui, A Core@sheath Nanofibrous Separator for Lithium Ion Batteries Obtained by Coaxial Electrospinning, Macromolecular Materials and Engineering, 298 (2012) 806-813.

[99] S. Yang, W. Ma, A. Wang, J. Gu, Y. Yin, A core–shell structured polyacrylonitrile@poly(vinylidene fluoride-hexafluoro propylene) microfiber complex membrane as a separator by co-axial electrospinning, RSC Advances, 8 (2018) 23390-23396.

[100] X. Jiang, L. Xiao, X. Ai, H. Yang, Y. Cao, A novel bifunctional thermo-sensitive poly(lactic acid)@poly(butylene succinate) core–shell fibrous separator prepared by a coaxial electrospinning route for safe lithium-ion batteries, Journal of Materials Chemistry A, 5 (2017) 23238-23242.

[101] K. Liu, W. Liu, Y. Qiu, B. Kong, Y. Sun, Z. Chen, D. Zhuo, D. Lin, Y. Cui, Electrospun core-shell microfiber separator with thermal-triggered flame-retardant properties for lithium-ion batteries, Science Advances, 3 (2017).

[102] S. Park, C.W. Son, S. Lee, D.Y. Kim, C. Park, K.S. Eom, T.F. Fuller, H.I. Joh, S.M. Jo, Multicore-shell nanofiber architecture of polyimide/polyvinylidene fluoride blend for thermal and long-term stability of lithium ion battery separator, Scientific reports, 6 (2016) 36977.

[103] Y. Wang, S. Wang, J. Fang, L.-X. Ding, H. Wang, A nano-silica modified polyimide nanofiber separator with enhanced thermal and wetting properties for high safety lithium-ion batteries, Journal of Membrane Science, 537 (2017) 248-254.

[104] J. Shayapat, O.H. Chung, J.S. Park, Electrospun polyimide-composite separator for lithium-ion batteries, Electrochimica Acta, 170 (2015) 110-121.

[105] M. Yanilmaz, M. Dirican, X. Zhang, Evaluation of electrospun SiO2/nylon 6,6

nanofiber membranes as a thermally-stable separator for lithium-ion batteries, Electrochimica Acta, 133 (2014) 501-508.

[106] Q. Fu, G. Lin, X. Chen, Z. Yu, R. Yang, M. Li, X. Zeng, J. Chen, Mechanically Reinforced PVdF/PMMA/SiO2 Composite Membrane and Its Electrochemical Properties as a Separator in Lithium-Ion Batteries, Energy Technology, 6 (2018) 144-152.

[107] Y. Li, X. Ma, N. Deng, W. Kang, H. Zhao, Z. Li, B. Cheng, Electrospun SiO2/PMIA nanofiber membranes with higher ionic conductivity for high temperature resistance lithium-ion batteries, Fibers and Polymers, 18 (2017) 212-220.

[108] M. Yanilmaz, J. Zhu, Y. Lu, Y. Ge, X. Zhang, High-strength, thermally stable nylon 6,6 composite nanofiber separators for lithium-ion batteries, Journal of Materials Science, 52 (2017) 5232-5241.

[109] Y. Jiang, Y. Ding, P. Zhang, F. Li, Z. Yang, Temperature-dependent on/off PVP@TiO2 separator for safe Li-storage, Journal of Membrane Science, 565 (2018) 33-41.

[110] D. Boriboon, T. Vongsetskul, P. Limthongkul, W. Kobsiriphat, P. Tammawat, Cellulose ultrafine fibers embedded with titania particles as a high performance and eco-friendly separator for lithium-ion batteries, Carbohydrate polymers, 189 (2018) 145-151.

[111] O. Padmaraj, B.N. Rao, M. Venkateswarlu, N. Satyanarayana, Electrochemical characterization of electrospun nanocomposite polymer blend electrolyte fibrous membrane for lithium battery, The journal of physical chemistry. B, 119 (2015) 5299-5308.

[112] F. Hussain, M. Hojjati, M. Okamoto, R.E. Gorga, Review article: Polymer-matrix Nanocomposites, Processing, Manufacturing, and Application: An Overview, Journal of Composite Materials, 40 (2006) 1511-1575.

[113] B. Shi, M. He, Lewis acid–base property of P(VDF-co-HFP) measured by inverse gas chromatography, Journal of Applied Polymer Science, 107 (2008) 1642-1646.

[114] Y.-Z.Z. Zheng-Ming Huang, M. Kotaki, S. Ramakrishna, A review on polymer

nanofibers by electrospinning and their applications in nanocomposites, Composites Science and Technology, 63 (2003) 2223-2253.

[115] M. Yanilmaz, Y. Lu, M. Dirican, K. Fu, X. Zhang, Nanoparticle-on-nanofiber hybrid membrane separators for lithium-ion batteries via combining electrospraying and electrospinning techniques, Journal of Membrane Science, 456 (2014) 57-65.

[116] S.A. Smith, J.H. Park, B.P. Williams, Y.L. Joo, Polymer/ceramic co-continuous nanofiber membranes via room-curable organopolysilazane for improved lithium-ion battery performance, Journal of Materials Science, 52 (2016) 3657-3669.

[117] S.A. Smith, B.P. Williams, Y.L. Joo, Effect of polymer and ceramic morphology on the material and electrochemical properties of electrospun PAN/polymer derived ceramic composite nanofiber membranes for lithium ion battery separators, Journal of Membrane Science, 526 (2017) 315-322.

[118] Y. Liang, L. Ji, B. Guo, Z. Lin, Y. Yao, Y. Li, M. Alcoutlabi, Y. Qiu, X. Zhang, Preparation and electrochemical characterization of ionic-conducting lithium lanthanum titanate oxide_polyacrylonitrile submicron composite fiber-based lithium-ion battery separators, Journal of Power Sources, 196 (2011) 436-441.

[119] Y. Liang, Z. Lin, Y. Qiu, X. Zhang, Fabrication and characterization of LATP_PAN composite fiber-based lithium-ion battery separators, Electrochimica Acta, 56 (2011) 6474-6480.

[120] H.-l. Chen, X.-n. Jiao, Preparation and characterization of Polyvinylidene fluoride/Octaphenyl-Polyhedral oligomeric silsesquioxane hybrid Lithium-ion battery separators by electrospinning, Solid State Ionics, 310 (2017) 134-142.

[121] Y. Ni, S. Zheng, K. Nie, Morphology and thermal properties of inorganic–organic hybrids involving epoxy resin and polyhedral oligomeric silsesquioxanes, Polymer, 45 (2004) 5557-5568.

[122] H. Zhao, N. Deng, J. Yan, W. Kang, J. Ju, L. Wang, Z. Li, B. Cheng, Effect of OctaphenylPolyhedral oligomeric silsesquioxane on the electrospun Poly-m-phenylene isophthalamid separators for lithium-ion batteries with high safety and excellent electrochemical performance, Chemical Engineering Journal, 356 (2019) 11-21.

[123] I.S. Chronakis, S. Grapenson, A. Jakob, Conductive polypyrrole nanofibers via electrospinning: Electrical and morphological properties, Polymer, 47 (2006) 1597-1603.

[124] S. Cetiner, F. Kalaoglu, H. Karakas, A.S. Sarac, Electrospun Nanofibers of Polypyrrole-Poly(Acrylonitrile-co-Vinyl Acetate), Textile Research Journal, 80 (2010) 1784-1792.

[125] L. Zhao, X.X. Zhang, N. Wang, The Morphology, Structure and Electrical Properties of Polypyrrole Nanofibers via Electrospinning, Advanced Materials Research, 616-618 (2012) 1675-1679.

[126] C. Sasso, D. Beneventi, E. Zeno, D. Chaussy, M. Petit-Conil, N. Belgacem, Polypyrrole and polypyrrole/wood-derived materials conducting composites: a review, BioResources 6(2011) 3585-3620.

[127] E. Tavakkol, H. Tavanai, A. Abdolmaleki, M. Morshed, Production of conductive electrospun polypyrrole/poly(vinyl pyrrolidone) nanofibers, Synthetic Metals, 231 (2017) 95-106.

[128] T.S. Kang, S.W. Lee, J. Joo, J.Y. Lee, Electrically conducting polypyrrole fibers spun by electrospinning, Synthetic Metals, 153 (2005) 61-64.

[129] Y.-W. Ju, J.-H. Park, H.-R. Jung, W.-J. Lee, Electrochemical properties of polypyrrole/sulfonted SEBS composite nanofibers prepared by electrospinning, Electrochimica Acta, 52 (2007) 4841-4847.

[130] Y. Cong, S. Liu, H. Chen, Fabrication of Conductive Polypyrrole Nanofibers by Electrospinning, Journal of Nanomaterials, 2013 (2013) 1-6.

[131] H. Yao, F. Zhang, G. Zhang, H. Luo, L. Liu, M. Shen, Y. Yang, A novel two-dimensional coordination polymer-polypyrrole hybrid material as a high-performance electrode for flexible supercapacitor, Chemical Engineering Journal, 334 (2018) 2547-2557.

[132] A. Chatterjee, S. Maity, A comparative study of reaction kinetics of in-situ chemical polymerization of polypyrrole onto various textile fibres, Surface and Coatings Technology, 324 (2017) 569-576.

[133] Y. Wang, G.A. Sotzing, R.A. Weiss, Preparation of Conductive Polypyrrole/Polyurethane Composite Foams by In situ Polymerization of Pyrrole, Chemistry of Materials, 20 (2008) 2574-2582.

[134] J.Y. Lee, C.A. Bashur, A.S. Goldstein, C.E. Schmidt, Polypyrrole-coated electrospun PLGA nanofibers for neural tissue applications, Biomaterials, 30 (2009) 4325-4335.

[135] T. Sudwilai, J.J. Ng, C. Boonkrai, N. Israsena, S. Chuangchote, P. Supaphol, Polypyrrole-coated electrospun poly(lactic acid) fibrous scaffold: effects of coating on electrical conductivity and neural cell growth, Journal of biomaterials science. Polymer edition, 25 (2014) 1240-1252.

[136] J. Thunberg, T. Kalogeropoulos, V. Kuzmenko, D. Hägg, S. Johannesson, G. Westman, P. Gatenholm, In situ synthesis of conductive polypyrrole on electrospun cellulose nanofibers: scaffold for neural tissue engineering, Cellulose, 22 (2015) 1459-1467.

[137] S. Shafei, J. Foroughi, Z. Chen, C.S. Wong, M. Naebe, Short Oxygen Plasma Treatment Leading to Long-Term Hydrophilicity of Conductive PCL-PPy Nanofiber Scaffolds, Polymers, 9 (2017).

[138] J. Wang, K. Pan, Q. He, B. Cao, Polyacrylonitrile/polypyrrole core/shell nanofiber mat for the removal of hexavalent chromium from aqueous solution, Journal of hazardous materials, 244-245 (2013) 121-129.

[139] Y. Yang, J. Wen, J. Wei, R. Xiong, J. Shi, C. Pan, Polypyrrole-decorated Ag-TiO2

nanofibers exhibiting enhanced photocatalytic activity under visible-light illumination, ACS applied materials & interfaces, 5 (2013) 6201-6207.

[140] S. Nair, E. Hsiao, S.H. Kim, Fabrication of electrically-conducting nonwoven porous mats of polystyrene–polypyrrole core–shell nanofibers via electrospinning and vapor phase polymerization, Journal of Materials Chemistry, 18 (2008) 5155.

[141] G.E. Blomgren, The Development and Future of Lithium Ion Batteries, Journal of The Electrochemical Society, 164 (2016) A5019-A5025.

[142] S. Liu, X. Liu, R. Dou, W. Zhou, Z. Wen, L. Liu, Experimental and simulation study on thermal characteristics of 18,650 lithium–iron–phosphate battery with and without spot–welding tabs, Applied Thermal Engineering, 166 (2020) 114648.

[143] W.A. Appiah, J. Park, L. Van Khue, Y. Lee, J. Choi, M.-H. Ryou, Y.M. Lee, Comparative study on experiments and simulation of blended cathode active materials for lithium ion batteries, Electrochimica Acta, 187 (2016) 422-432.

[144] H. Li, Y. Wang, X. He, Q. Li, C. Lian, Z. Wang, Effects of Structure Parameters on the Thermal Performance of a Ternary Lithium-Ion Battery under Fast Charging Conditions, Energy & Fuels, 34 (2020) 8891-8904.

[145] J. Li, Y. Cheng, M. Jia, Y. Tang, Y. Lin, Z. Zhang, Y. Liu, An electrochemical–thermal model based on dynamic responses for lithium iron phosphate battery, Journal of Power Sources, 255 (2014) 130-143.

[146] A. Jokar, B. Rajabloo, M. Désilets, M. Lacroix, Review of simplified Pseudo-two-Dimensional models of lithium-ion batteries, Journal of Power Sources, 327 (2016) 44-55.

[147] B. Suthar, P.W.C. Northrop, D. Rife, V.R. Subramanian, Effect of Porosity, Thickness and Tortuosity on Capacity Fade of Anode, Journal of The Electrochemical Society, 162 (2015) A1708-A1717.

[148] D. Miranda, A. Gören, C.M. Costa, M.M. Silva, A.M. Almeida, S. Lanceros-Méndez,

Theoretical simulation of the optimal relation between active material, binder and conductive additive for lithium-ion battery cathodes, Energy, 172 (2019) 68-78.

[149] E. Hosseinzadeh, J. Marco, P. Jennings, The impact of multi-layered porosity distribution on the performance of a lithium ion battery, Applied Mathematical Modelling, 61 (2018) 107-123.

[150] R. Scipioni, P.S. Jørgensen, C. Graves, J. Hjelm, S.H. Jensen, A Physically-Based Equivalent Circuit Model for the Impedance of a LiFePO4/Graphite 26650 Cylindrical Cell, Journal of The Electrochemical Society, 164 (2017) A2017-A2030.

[151] L.H. Saw, Y. Ye, A.A.O. Tay, Electro-thermal analysis and integration issues of lithium ion battery for electric vehicles, Applied Energy, 131 (2014) 97-107.

[152] M. Doyle, Modeling of Galvanostatic Charge and Discharge of the Lithium/Polymer/Insertion Cell, Journal of The Electrochemical Society, 140 (1993) 1526.

[153] M. Xu, Z. Zhang, X. Wang, L. Jia, L. Yang, Two-dimensional electrochemical–thermal coupled modeling of cylindrical LiFePO4 batteries, Journal of Power Sources, 256 (2014) 233-243.

[154] J. Li, Y. Cheng, L. Ai, M. Jia, S. Du, B. Yin, S. Woo, H. Zhang, 3D simulation on the internal distributed properties of lithium-ion battery with planar tabbed configuration, Journal of Power Sources, 293 (2015) 993-1005.

[155] N. Yang, X. Zhang, B. Shang, G. Li, Unbalanced discharging and aging due to temperature differences among the cells in a lithium-ion battery pack with parallel combination, Journal of Power Sources, 306 (2016) 733-741.

[156] K. Kumaresan, G. Sikha, R.E. White, Thermal Model for a Li-Ion Cell, Journal of The Electrochemical Society, 155 (2008) A164.

[157] F. Jiang, P. Peng, Elucidating the Performance Limitations of Lithium-ion Batteries due to Species and Charge Transport through Five Characteristic Parameters, Scientific

reports, 6 (2016) 32639.

[158] L. Cai, R.E. White, Mathematical modeling of a lithium ion battery with thermal effects in COMSOL Inc. Multiphysics (MP) software, Journal of Power Sources, 196 (2011) 5985-5989.

[159] F. Kreith, W.Z. Black, Basic Heat Transfer, New York: Crowel, 1980.

[160] S.C. Agwuncha, I.D. Ibrahim, E.R. Sadiku, Improving the thermal and flame resistance properties of polyolefins, (2017) 421-448.

[161] O. Olabisi, K. Adewale, Handbook of Thermoplastics . 2nd ed., CRC Press, Florida, 2016.

[162] T. Yang, N. Yang, X. Zhang, G. Li, Investigation of the thermal performance of axial-flow air cooling for the lithium-ion battery pack, International Journal of Thermal Sciences, 108 (2016) 132-144.

[163] R. Wang, J. Yu, F. Islam, A. Tahmasebi, S. Lee, Y. Chen, State-of-the-Art Research and Applications of Carbon Foam Composite Materials as Electrodes for High-Capacity Lithium Batteries, Energy & Fuels, 34 (2020) 7935-7954.

[164] P.V. Braun, J. Cho, J.H. Pikul, W.P. King, H. Zhang, High power rechargeable batteries, Current Opinion in Solid State and Materials Science, 16 (2012) 186-198.

[165] T. Wang, Y. Wang, G. Cheng, C. Ma, X. Liu, J. Wang, W. Qiao, L. Ling, Catalytic Graphitization of Anthracite as an Anode for Lithium-Ion Batteries, Energy & Fuels, 34 (2020) 8911-8918.

[166] Y. Yang, X. Huang, Z. Cao, G. Chen, Thermally conductive separator with hierarchical nano/microstructures for improving thermal management of batteries, Nano Energy, 22 (2016) 301-309.

[167] P. Wang, X. Zhang, L. Yang, X. Zhang, M. Yang, H. Chen, D. Fang, Real-time monitoring of internal temperature evolution of the lithium-ion coin cell battery during the

charge and discharge process, Extreme Mechanics Letters, 9 (2016) 459-466.

[168] Q. Wang, P. Ping, X. Zhao, G. Chu, J. Sun, C. Chen, Thermal runaway caused fire and explosion of lithium ion battery, Journal of Power Sources, 208 (2012) 210-224.

[169] C. Luo, J. Wang, P. Jia, Y. Liu, J. An, B. Cao, K. Pan, Hierarchically structured polyacrylonitrile nanofiber mat as highly efficient lead adsorbent for water treatment, Chemical Engineering Journal, 262 (2015) 775-784.

[170] X. Lu, C. Shen, Z. Zhang, E. Barrios, L. Zhai, Core-Shell Composite Fibers for High-Performance Flexible Supercapacitor Electrodes, ACS applied materials & interfaces, 10 (2018) 4041-4049.

[171] S. Percec, L. Howe, K. Ferguson, B. Wood, J. Li, Hybrid assemblies by pyrrole polymerization on nano graphene oxide platelets, Polymer, 70 (2015) 139-148.

[172] Y. Tan, K. Ghandi, Kinetics and mechanism of pyrrole chemical polymerization, Synthetic Metals, 175 (2013) 183-191.

[173] Y.O. Mezhuev, I.V. Plyushchii, Y.V. Korshak, M.I. Shtil'man, I.A. Gritskova, Dispersion Oxidative Polymerization of Pyrrole in Aqueous Solutions of Polyvinyl Alcohol, Russian Journal of General Chemistry, 89 (2019) 1477-1484.

[174] C.P. Andrieux, P. Audebert, P. Hapiot, J.M. Saveant, Identification of the first steps of the electrochemical polymerization of pyrroles by means of fast potential step techniques, The Journal of Physical Chemistry, 95 (2002) 10158-10164.

[175] R.B. Bjorklund, Kinetics of pyrrole polymerisation in aqueous iron chloride solution, Journal of the Chemical Society, Faraday Transactions 1: Physical Chemistry in Condensed Phases, 83 (1987) 1507.

[176] N.V. Blinova, J. Stejskal, M. Trchová, J. Prokeš, M. Omastová, Polyaniline and polypyrrole: A comparative study of the preparation, European Polymer Journal, 43 (2007) 2331-2341.

[177] H. Eyring, The Activated Complex in Chemical Reactions, J. Chem. Phys., 3 (1935) 107–115.

[178] C. Lin, T. Lü, D. Qi, Z. Cao, Y. Sun, Y. Wang, Effects of Surface Groups on SiO2 Nanoparticles on in Situ Solution Polymerization: Kinetics and Mechanism, Industrial & Engineering Chemistry Research, (2018).

[179] R. Stanković, V. Laninović, S. Stanković, S. Jovanović, M. Vojnović, Kinetics of the chemical polymerization of pyrrole by potassium hexacyanoferrate(III), Macromolecular Chemistry and Physics, 196 (1995) 825-832.

[180] M. Zhou, J. Qian, X. Ai, H. Yang, Redox-active Fe(CN)(6)(4-)-doped conducting polymers with greatly enhanced capacity as cathode materials for Li-ion batteries, Adv Mater, 23 (2011) 4913-4917.

[181] M.F. Planche, J.C. Thiéblemont, N. Mazars, G. Bidan, Kinetic study of pyrrole polymerization with iron (III) chloride in water, Journal of Applied Polymer Science, 52 (1994) 1867-1877.

[182] R.V. Gregory, W.C. Kimbrell, H.H. Kuhn, Conductive textiles, Synthetic Metals, 28 (1989) 823-835.

[183] G. Yuan, R. Cranston, Recent Advances in Antimicrobial Treatments of Textiles, Textile Research Journal, 78 (2008) 60-72.

[184] L.A. Al-Khateeb, S. Almotiry, M.A. Salam, Adsorption of pharmaceutical pollutants onto graphene nanoplatelets, Chemical Engineering Journal, 248 (2014) 191-199.

[185] T. Norby, M. Wideroe, R. Glockner, Y. Larring, Hydrogen in oxides, Dalton transactions, (2004) 3012-3018.

[186] R. Givehchi, Q. Li, Z. Tan, Quality factors of PVA nanofibrous filters for airborne particles in the size range of 10–125 nm, Fuel, 181 (2016) 1273-1280.

[187] G. Socrates, Infra red and Raman Characteristic Group Frequencies, 3rd ed., John

Wiley & Sons, 2004.

[188] P. Verma, P. Maire, P. Novák, A review of the features and analyses of the solid electrolyte interphase in Li-ion batteries, Electrochimica Acta, 55 (2010) 6332-6341.

[189] Z. Wang, R. Pan, C. Xu, C. Ruan, K. Edström, M. Strømme, L. Nyholm, Conducting polymer paper-derived separators for lithium metal batteries, Energy Storage Materials, 13 (2018) 283-292.

[190] Y. Gao, X. Sang, Y. Chen, Y. Li, B. Liu, J. Sheng, Y. Feng, L. Li, H. Liu, X. Wang, C. Kuang, Y. Zhai, Polydopamine modification electrospun polyacrylonitrile fibrous membrane with decreased pore size and dendrite mitigation for lithium ion battery, Journal of Materials Science, 55 (2019) 3549-3560.

[191] F. Khodaverdi, A. Vaziri, M. Javanbakht, M. Jahanfar, Improvement of PAN separator properties using PVA /malonic acid by electrospinning in lithium ion-batteries, Journal of Applied Polymer Science, 138 (2020) 50088.

[192] D. De Marco, A. Marchese, P. Migliardo, A. Bellomo, Thermal analysis of some cyano compounds, Journal of thermal analysis, 32 (1987) 927-937.

[193] L. Qie, L.-X. Yuan, W.-X. Zhang, W.-M. Chen, Y.-H. Huang, Revisit of Polypyrrole as Cathode Material for Lithium-Ion Battery, Journal of The Electrochemical Society, 159 (2012) A1624-A1629.

[194] J. Xue, T. Wu, Y. Dai, Y. Xia, Electrospinning and Electrospun Nanofibers: Methods, Materials, and Applications, Chem Rev, 119 (2019) 5298-5415.

[195] F. Xie, Y. Wang, L. Zhuo, F. Jia, D. Ning, Z. Lu, Electrospun Wrinkled Porous Polyimide Nanofiber-Based Filter via Thermally Induced Phase Separation for Efficient High-Temperature PMs Capture, ACS applied materials & interfaces, 12 (2020) 56499-56508.

[196] M. Peng, D. Li, L. Shen, Y. Chen, Q. Zheng, H. Wang, Nanoporous structured

submicrometer carbon fibers prepared via solution electrospinning of polymer blends, Langmuir: the ACS journal of surfaces and colloids, 22 (2006) 9368-9374.

Appendix A

Method to fabricate electrospun membrane with uniform fiber distribution

A.1 Introduction

The uniformity of a membrane separator is important to the LIB performance. The use of a structurally uniformed separator in a LIB cell can help to achieve a uniform distributed current density on the electrodes. Thereby, it inhibits the grows of lithium dendrite and also prevents the loose particles from penetrating the separators [1]. In general, the uniformity of the separator plays a critical role in the stable and long cycle life of LIB operation.

Electrospinning is an effective method to produce nanofibrous separators for LIBs. Flat or rotating cylindrical collectors are commonly adopted in an electrospinning setup to collect nanofibers. However, it's not always easy to peal the final collected membrane off the collector due to the strong adhesion between the collector and nanofibers. Alternatively, the collector is commonly wrapped by a metallic cover (*e.g.*, aluminum foil, metal mesh) in order to conveniently peel off the electrospun membrane in practical. However, the uniformity of the fabricated membrane is strongly affected by the electrical field distribution between the spinning needle and the grounded collector [2]. These added-on collector covers interfere in the electrical field distribution, leading to altering the uniformity of the fabricated membrane.

Three different collector covers, namely 50 mesh metal mesh, 200 mesh metal mesh and nonstick aluminum foil, are used in this appendix to investigate its effect on the uniformity of the fabricated electrospun membrane. The fabricated membrane is peeled off from the collector covers and examined by optical microscope. The uniformity of the electrospun membrane is further quantified by the standard deviation of the grey scales of the corresponding optical microscope image.

A.2 Experiment

A.2.1 Materials

Polyacrylonitrile (PAN, M_W=150000), N,N-dimethylformamide (DMF, purity>99.8%) are purchased form Sigma Aldrich, Canada. Stainless steel metal meshes with 50 and 200 mesh are purchased from Ted Pella, Inc., USA. Non-stick aluminum foil is obtained from Reynolds wrap, USA. All chemicals are used as received without any further purification.

A.2.2 Fabrication of electrospun membrane

A laboratory-made electrospinning device is used to produce PAN nanofibrous membranes as follows. First, PAN polymer is dissolved into DMF to prepare the solution of 10 wt.% concentration as electrospinning precursor. Then, the PAN solution is loaded into a syringe with a metallic needle (with inner diameter of 0.514 mm) connected to a laboratory-made positive high voltage supply. A grounded drum collector (at a rotating speed of 30 rpm) covered by different collector covers, namely the 50 mesh metal mesh, 200 mesh metal mesh and nonstick aluminum foil, is placed 11 cm away from the needle tip and used as a fiber collector. Finally, Continuous fiber jets are generated from the needle tip to form a membrane on the fiber collector when the voltage is adjusted to 7.5 kV and the PAN solution is pumped at a steady flow rate of 0.4 ml/hr.

A.2.3 Characterization of electrospun membrane

The prepared electrospun membrane is peeled off from different collector covers and examined using an optical microscope (SW380B, Swift, Canada). Then, the grayscale values of each pixels of the microscope image are extracted using the following Python code on the Colaboratory platform:

```
import cv2
```

```
im = cv2.imread("/content/microscope image.png")

gray = cv2.cvtColor(im, cv2.COLOR_BGR2GRAY)

print(gray)

import pandas as pd

df=pd.DataFrame(gray)

df.to_csv(' grayscale value',sep='\t')
```

A.3 Results and discussion

Figure A.1 shows the optical microscope images of the electrospun membrane fabricated using different collector covers under 250× magnification. The membrane fabricated with metal meshes clearly shows a mesh pattern, whereas the one fabricated with nonstick aluminum foil obtained much uniform fiber misdistribution. The image of the membrane is darker at the position where the metal mesh contacted, due to more nanofibers are accumulated at this position. This is because the metal mesh is not a flat surface, the use of it as collector cover disturbs the electrostatic field distribution between the charged needle and collector. As a result, the resultant electrospun membrane shows ununiformed fiber distribution, although the metal mesh facilitates the peeling off of the membrane.

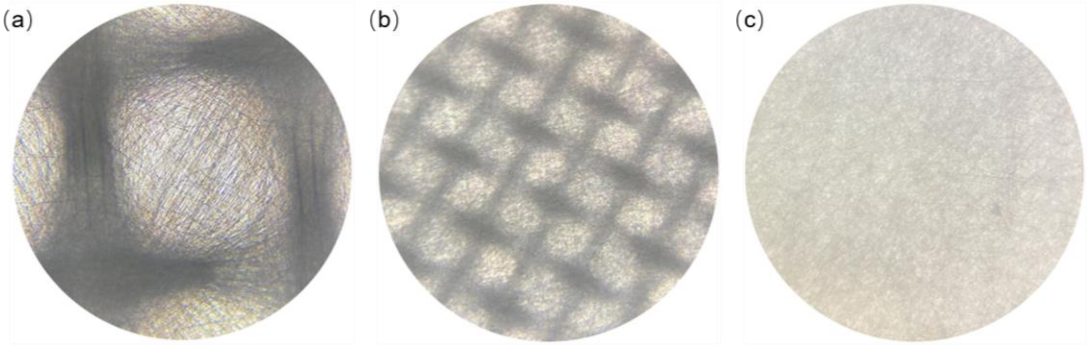

Figure A.1. Optical microscope image of electrospun membrane fabricated using (a) 50 mesh metal mesh (b) 200 mesh metal mesh and (c) nonstick aluminum foil as collector cover

The grayscale values of each pixels of the microscope image are extracted to quantitatively compare the uniformity of the membrane fabricated by different collector cover. Figure A.2 shows the grayscale distribution along the horizontal and vertical centerlines of the microscope images obtained with different collector covers. The grayscale value ranging from 0-255 indicates the different shades of the pixel from black to white. The grayscale distribution of the image obtained from using 50 mesh metal mesh shows the most fluctuated curve with grayscale values varies from 100 to 255, whereas the grayscale distribution of nonstick aluminum foil exhibits much stable variation between 190 to 240.

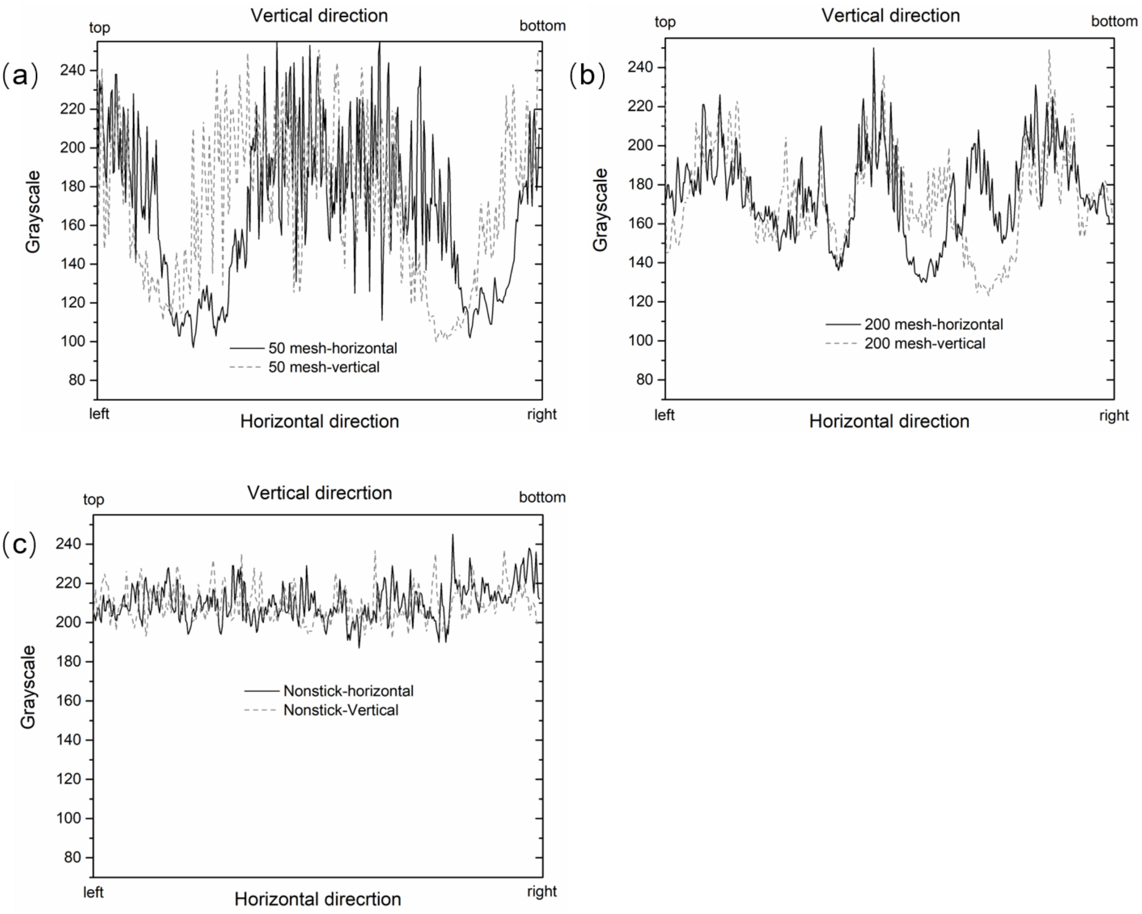

Figure A.2. Grayscale distribution along the horizontal and vertical centerlines of microscope image of electrospun membrane fabricated using (a) 50 mesh metal mesh (b) 200 mesh metal mesh and (c) nonstick aluminum foil as collector cover

The variation of the grayscale distribution of the microscope image implies the uniformity of the corresponding electrospun membrane. The decrease of the grayscale values indicates the thicker fiber accumulation. As a result, a few wide ranges of low value grayscales regions are found in the Figure A.2 (a) and (b). These regions correspond to the darker areas of the microscope image showed in Figure A.1 (a) and (b), where the fibers are accumulated following the pattern of the metal mesh. Finally, the standard deviation of the grayscale distribution is calculated as 39.3, 23.4 and 8.9 for the microscope images obtained with 50 mesh metal mesh, 200 mesh metal mesh, and nonstick aluminum foil, respectively. The results indicate that the best uniform electrospun membrane is obtained by using nonstick aluminum foil as collector cover.

A.3 Summary

Three different collector covers, namely 50 mesh metal mesh, 200 mesh metal mesh and nonstick aluminum foil, are used in this appendix to investigate its effect on the uniformity of the fabricated electrospun membrane. Collector covers are commonly used in an electrospinning process to facilitate the peeling off of the electrospun membranes. However, the results of this appendix show that the use of metal meshes as collector covers cause the ununiform fiber distribution of electrospun membranes, as evidence by the fluctuated grayscale distributions of the corresponding microscope images. On the contrary, the use of nonstick aluminum foil not only facilitates the membrane peeling, but also leading to the uniform fiber distribution of the electrospun membrane, as the lowest standard deviation of grayscale (8.9) obtained from the microscope image compared to the other collector covers (39.3 and 23.4).

References

[1] H. Lee, M. Yanilmaz, O. Toprakci, K. Fu, X. Zhang, A review of recent developments in membrane separators for rechargeable lithium-ion batteries, Energy Environ. Sci., 7 (2014) 3857-3886.

[2] J. Xue, T. Wu, Y. Dai, Y. Xia, Electrospinning and Electrospun Nanofibers: Methods, Materials, and Applications, Chem Rev, 119 (2019) 5298-5415.

Appendix B

Fabrication of electrospun nanofibers with intra-fiber porosity

B.1 Introduction

Fabrication of nanofibers with intra-fiber porous structure is a feasible way to further increase the overall surface area of the electrospun fibrous membrane. As discussed in Section 6.2, electrospun membrane with such high surface area can be used for preparing redox-active separator with improved PPy loading.

Feasible methods to prepare electrospun nanofibers with intra-porous structure including non-solvent induced phase separation [1], thermal-induced phase separation [2], and selective removal of a sacrificial phase [3]. The non-solvent induced phase separation method is to spin nanofibers using a ternary spinning solution (*i.e.*, polymer, solvent, and nonsolvent). The proportion of the ternary system in the fiber jets changes during the travelling of fibers in the air due to the difference in volatility between the solvent and nonsolvent. As a result, phase separation occurs in the ejected fibers, leading to the formation of porous structures. The thermal induced phase separation method is based on the rapid cooling of the incompletely solidified fiber jets. It can be achieved by electrospinning a polymer solution with highly volatile solvent. The rapidly evaporating of the solvent causes the cooling of unsolidified fiber jets leading to the phase separation to create intra-fiber pores. The method of selective removal of a sacrificial phase is achieved by implementing post-treatments to electrospun fibers. Generally, the prepared electrospun fibers contains least at two different polymer phases, in which the sacrificial polymer can be removed by a post-treatment process (*e.g.*, dissolving in solvent, heat treatment) to leave intra-fiber pores on the fibers.

Two different methods of non-solvent induced phase separation and selective removal of sacrificial phase are adopted in this appendix to investigate the feasibility of fabricating electrospun nanofibers with intra-fiber porous stricture. The prepared membrane samples are characterized using SEM to analyze the fiber morphology.

B.2 Experiment

B.2.1 Materials

Polyacrylonitrile (PAN, M_W=150,000), Polyvinylpyrrolidone (PVP, M_W=10,000), N,N-dimethylformamide (DMF, purity>99.8%) are purchased from Sigma Aldrich, Canada. All chemicals are used as received without any further purification.

B.2.2 Fabrication of electrospun membrane

The fabrication of electrospun nanofibers using selective removal of sacrificial phase method is carried out as follows. PAN and PVP polymers are dissolved in DMF solvent to prepare electrospinning solution with overall concentration of 8 wt.%. The weight ratio of PAN:PVP in the prepared solution ranges from 2:1 to 1:2. The electrospinning process is operated under 12.5 kV with the solution flow rate at 0.65 ml/h and collector distance at 17 cm. Then, the obtained electrospun membrane is immersed into deionized water for 2 hours at room temperature, following by drying under vacuum at 80 °C in a vacuum oven for at least 12 hours (Vacuumoven-001, LeDAB, Canada).

The fabrication process of electrospun nanofibers using non-solvent induced phase separation method is as follows. PAN is dissolved in water/DMF mixed solvent to prepare ternary electrospinning solution with the weight ratio of PAN:DMF:Water=6:93:1 or 6:91:3. The electrospinning process is operated under 12.5 kV with the solution flow rate at 0.65 ml/h and collector distance at 17 cm to produce nanofibers.

B.3 Results and discussion

Figure B.1 shows the SEM images of the electrospun fibers prepared using selective removal of sacrificial phase method. Although beaded fibers are observed in all the prepared samples, rough fiber surface is obtained using this method. The fiber surface become rougher with the decreasing PAN:PVP ratio from 2:1 to 1:2 as show in the SEM images with large magnification (Figure B.1 b, d, f). However, the number of beaded fibers also increases with the decreasing PAN:PVP ratio. In addition, the roughness of the fibers is not uniformly distribution along the fiber surface. Some regions of the fibers are roughed, whereas the other regions still exhibit smooth fiber morphology.

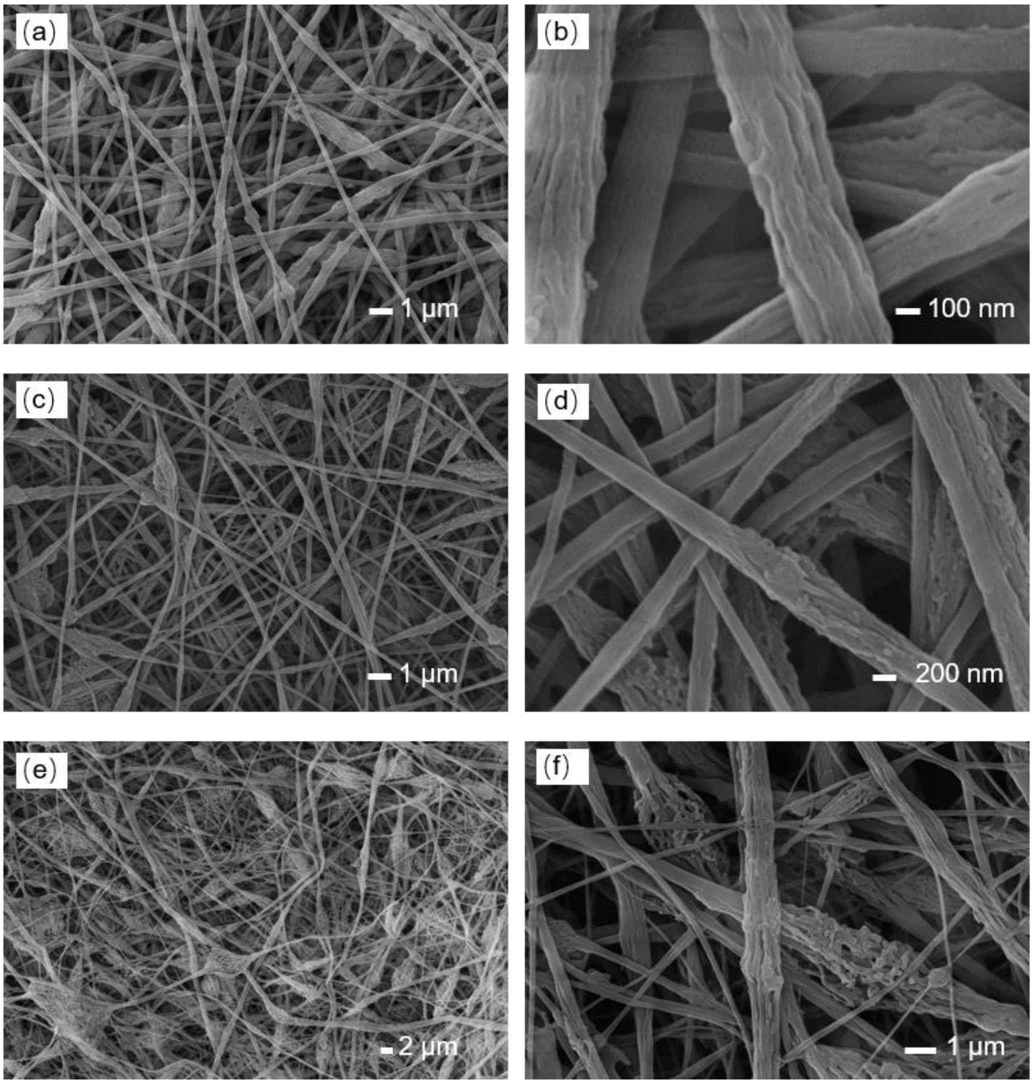

Figure B.1. SEM images of electrospun membrane prepared using selective removal of sacrificial phase method. (a) (b) PAN:PVP=2:1. (c) (d) PAN:PVP=1:1. (e) (f) PAN:PVP=1:2.

The rough fiber surface is obtained due to the removal of the sacrificial polymer PVP from the PAN/PVP composite electrospun fibers. Soaking the composite fibers in water results in the dissolving of the water-soluble polymer PVP and leaves dents on the fiber surface. While, the left non-soluble PAN polymer maintains the fiber structure. However, the PAN and PVP polymers are not homogeneously mixed in the prepared spinning solution, which causes the ununiform roughness across fabricated fibers. Even though, the selective removal of sacrificial phase method used in the study can produce rough fibers, the desired intra-fiber porous structure is not achieved.

Figure B.2 shows the SEM images of electrospun nanofibers prepared using non-solvent induced phase separation method. Beaded fibers are formed in both membrane samples fabricated using different water contents as the non-solvent in the electrospinning solution. Increasing the water content results in the even more beads formed on the fibers. Rough fiber surface is produced by this method. In addition, some small intra-fiber pores are observed for the sample fabricated with 3% water content (*see* Figure B.2 d).

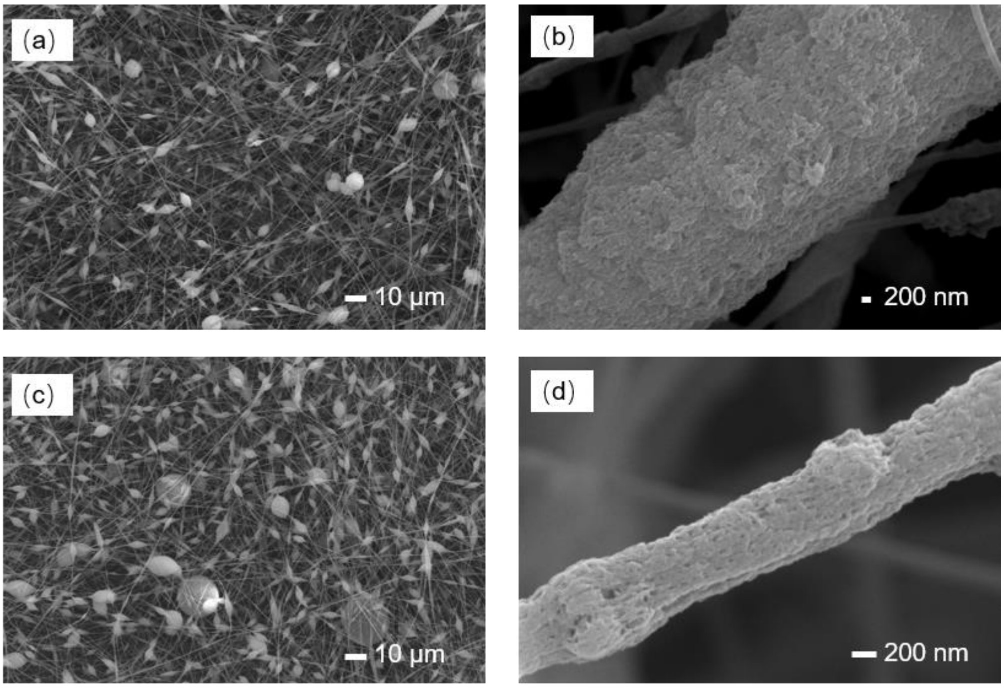

Figure B.2. SEM images of electrospun membrane prepared using non-solvent induced phase separation method (a) (b) PAN:DMF:Water=6:93:1. (c) (d) PAN:DMF:Water=6:91:3.

The formation of the rough fiber surface is owing to the adding of non-solvent water in the electrospinning solution. The proportion of the non-solvent water in the fiber jets increases during the travelling of fibers in the air due to its lower volatility compared to the solvent DMF. As a result, phase separation occurs in the ejected fibers, leading to the formation of small dents on the fiber structures. Some small intra-fiber pores are observed for the sample fabricated with 3% water content. However, further increase the water content causes the precipitation of PAN from the electrospinning solution which becomes not spinnable. Moreover, the beaded fibers are not desired for the application of battery separator, because the use of a structurally ununiform separator in a LIB cell results in the ununiform distributed current density on the electrodes, which causes the grows of lithium dendrite and also the penetration of loose electrode particles [4].

B.4 Summary

Two different methods, *i.e.*, selective removal of sacrificial phase and non-solvent induced phase separation, are adopted in this appendix to investigate the feasibility of fabricating electrospun fibers with intra-fiber porous structure. The experimental results show that both methods are capable of producing rough electrospun fibers. However, the ideal intra fiber pores are not observed. In addition, the resultant membrane contains considerable numbers of beaded fibers, which is not desired for use as battery separator. Therefore, further efforts are needed to optimize the fabrication process, in order to produce electrospun nanofibers with uniform distributed intra-fiber pores.

References

[1] X. Yu, H. Xiang, Y. Long, N. Zhao, X. Zhang, J. Xu, Preparation of porous polyacrylonitrile fibers by electrospinning a ternary system of PAN/DMF/H2O, Materials Letters, 64 (2010) 2407-2409.

[2] F. Xie, Y. Wang, L. Zhuo, F. Jia, D. Ning, Z. Lu, Electrospun Wrinkled Porous Polyimide

Nanofiber-Based Filter via Thermally Induced Phase Separation for Efficient High-Temperature PMs Capture, ACS applied materials & interfaces, 12 (2020) 56499-56508.

[3] M. Peng, D. Li, L. Shen, Y. Chen, Q. Zheng, H. Wang, Nanoporous structured submicrometer carbon fibers prepared via solution electrospinning of polymer blends, Langmuir: the ACS journal of surfaces and colloids, 22 (2006) 9368-9374.

[4] H. Lee, M. Yanilmaz, O. Toprakci, K. Fu, X. Zhang, A review of recent developments in membrane separators for rechargeable lithium-ion batteries, Energy Environ. Sci., 7 (2014) 3857-3886.